

INFORMATION TO USERS

This manuscript has been reproduced from the microfilm master. UMI films the text directly from the original or copy submitted. Thus, some thesis and dissertation copies are in typewriter face, while others may be from any type of computer printer.

The quality of this reproduction is dependent upon the quality of the copy submitted. Broken or indistinct print, colored or poor quality illustrations and photographs, print bleedthrough, substandard margins, and improper alignment can adversely affect reproduction.

In the unlikely event that the author did not send UMI a complete manuscript and there are missing pages, these will be noted. Also, if unauthorized copyright material had to be removed, a note will indicate the deletion.

Oversize materials (e.g., maps, drawings, charts) are reproduced by sectioning the original, beginning at the upper left-hand corner and continuing from left to right in equal sections with small overlaps. Each original is also photographed in one exposure and is included in reduced form at the back of the book.

Photographs included in the original manuscript have been reproduced xerographically in this copy. Higher quality 6" x 9" black and white photographic prints are available for any photographs or illustrations appearing in this copy for an additional charge. Contact UMI directly to order.

U·M·I

University Microfilms International
A Bell & Howell Information Company
300 North Zeeb Road, Ann Arbor, MI 48106-1346 USA
313:761-4700 800:521-0600

Order Number 9309359

**Ultra-high vacuum transmission electron microscopy of the clean
surfaces of Au and Ir (001)**

Dunn, Derren Neylon, Ph.D.

Northwestern University, 1992

U·M·I

300 N. Zeeb Rd.
Ann Arbor, MI 48106



NORTHWESTERN UNIVERSITY

**ULTRA HIGH VACUUM TRANSMISSION ELECTRON MICROSCOPY OF
THE CLEAN SURFACES OF AU AND IR (001)**

A DISSERTATION

SUBMITTED TO THE GRADUATE SCHOOL IN
PARTIAL FULFILLMENT OF THE REQUIREMENTS

for the degree

DOCTOR OF PHILOSOPHY

Field of Materials Science and Engineering

BY

Derren Neylon Dunn, *D. N.*

EVANSTON, ILLINOIS *Ph. D.*

December 1992

ABSTRACT

ULTRA HIGH VACUUM TRANSMISSION ELECTRON MICROSCOPY OF THE CLEAN SURFACES OF AU (001) AND IR (001)

DERREN NEYLON DUNN

The *in situ* preparation and observation of the clean surfaces of (001) oriented Au and Ir single crystals are investigated in a novel ultra high vacuum transmission electron microscope. A general method for preparing bulk single crystal samples for ultra high vacuum transmission electron microscopy (UHV-TEM) is given as a two part process. The first part of this process is a mechanical polishing step using standard metallographic procedures which occurs outside the microscope vacuum. The second part of this technique takes advantage of traditional surface science sputter anneal cycles to prepare the surface once inside the ultra high vacuum environment of the microscope.

The clean Au (001) surface was found to reconstruct into a (5xn) unit cell where n ranges between 15 and 21. The reconstructed surface is found to consist of a hexagonal layer superimposed on the bulk terminated FCC (1x1) quadratic surface. The variation in the 'n' dimension of the reconstructed unit cell is found to be due to a shear, rather than a rotation, as has been previously reported. It is also found that the strain fields of bulk defects such as dislocations and stacking faults interact with the (5xn) reconstruction.

The clean Ir (001) surface was found to reconstruct into a (5x1) surface unit cell. Similar to the Au (5xn) reconstruction, the Ir (5x1) reconstruction consists of a hexagonal

overlayer superimposed on the quadratic fcc (1x1) surface. The Ir (001) (5x1) reconstruction is not observed to interact with bulk defects as is seen in the case of the Au (001) surface.

Finally, two dimensional linear elasticity solutions are given for the case of a single edge dislocation and an array of evenly spaced edge dislocations, situated below the free surface of an infinitely extended elastic half space. The analysis is carried out by extending existing solutions to a limiting case. The elastic potential energies for both the single edge dislocation and the array of evenly spaced edge dislocations are explored as a function of distance below the free surface.

Approved¹:

¹Professor Laurence D. Marks (Thesis Advisor)
Department of Materials Science and Engineering
The Robert McCormick School of Engineering and Applied Sciences
Northwestern University
Evanston, Illinois
December 1992

DEDICATION

To My Parents Michael and Monica

ACKNOWLEDGEMENT

I would first like to thank my thesis advisor Professor Laurence D. Marks. I consider myself lucky to have worked on the Hitachi UHV-H9000 with an advisor like Professor Marks. His enthusiasm and sincere dedication to both science and teaching have been an inspiration to me. I am grateful for the patience he has shown me and the encouragement he has given me. I would also like to thank Professor John Dundurs of the Civil Engineering Department for his help on the dislocation analysis presented in Chapter 6. I have always enjoyed my discussions with Professor Dundurs, both in and out of the classroom. I would next like to thank my friends here at Northwestern, both the old and the new. I would especially like to thank Dr. Jin Ping Zhang for giving of himself and teaching me a few tricks on the microscope and in the dark room. Next, I would like to thank Dr. Vitaly Volpert for his help on the mathematics required for the dislocation analysis given in Chapter 6. He took the time to not only help but to teach and I enjoyed our interaction tremendously. I would also like to thank Dr. John Bonevich and Dr. Mary Buckett who helped me during the first half of my stay. For the new, I would like to thank Dr. Xiaohong Ai, Dr. Peirong Xu, De Jie Li and Dr. Hong Zhang; their help is greatly appreciated both in the lab and on my thesis. Special thanks are due to Anatol Bilyk for his willingness to help in a pinch.

Finally, I would like to thank my parents, Michael and Monica. They have always supported and believed in me and that has made all the difference.

TABLE OF CONTENTS

ABSTRACT	ii
ACKNOWLEDGEMENTS	v
LIST OF FIGURES	viii
Chapter 1 Introduction	1
Chapter 2 Experimental Equipment and Methods	9
2.1 Introduction	9
2.2 The Hitachi UHV-H9000 Microscope	10
2.3 Specimen Preparation Technique	13
2.4 Imaging Techniques	26
Chapter 3 UHV Microscopy of The Reconstructed Au (001) Surface	32
3.1 Introduction	32
3.2 Background	34
3.3 Experimental	36
3.4 Results	38
3.4.1 Basic Crystallography of The Reconstruction	38
3.4.2 Domain Structure	43
3.5 Discussion	52
Chapter 4 The Effect of Bulk Defects On Surface Reconstruction	60
4.1 Introduction	60
4.2 Background	60
4.3 Experimental	62
4.4 Results	62

Chapter 5 UHV Microscopy of The Reconstructed Ir (001) Surface	71
5.1 Introduction	71
5.2 Background	72
5.3 Experimental Procedures	76
5.4 Results	78
5.4.1 Initial Microstructure	78
5.4.2 Appearance of Steps	83
5.5 Ir (001) (5x1) Reconstruction	88
5.5.1 Diffraction Pattern Analysis And Particle Identification	88
5.5.2 Images of Reconstructed Ir (001) (5x1) Reconstruction	94
5.6 Discussion of Ir (001) (5x1) Reconstruction	98
Chapter 6 Edge Dislocations Near A Free Surface	101
6.1 Introduction	101
6.2 Background	102
6.3 Particular Solution For Single Edge Dislocation Near A Free Surface	104
6.4 Energy of The Single Dislocation Near A Free Surface	112
6.5 Stress Distribution of An Array of Edge Dislocations	117
6.6 Energy of An Array of Edge Dislocations Near The Free Surface of An Elastic Half Plane	125
6.7 Activation Energy For The Introduction of An Edge Dislocation Near A Free Surface	130
6.8 Discussion	134
Chapter 7 Summary And Suggestions For Research	135
7.1 General Remarks	135
7.2 Comparison of The Au And Ir Surfaces	139
7.3 Dislocation Analysis	141
7.4 Suggestions For Future Research	142
References	145

LIST OF FIGURES

FIGURE	PAGE
2.1 A schematic diagram of the hitachi UHV-H9000 Microscope and surface science chamber.	11
2.2 (a) A plot of focus values versus voltage for the Perkin-Elmer ion gun using Xe gas. (b) Focus values versus voltage for the Perkin Elmer ion gun using Ar gas.	17
2.3 Setup used to anneal a specimen in the SSC with the broad band optical annealing source.	18
2.4 A plot of the temperature versus voltage for the broad band optical annealing source.	19
2.5 (a) A bright field image of the Au sample after ion milling with 4 Kev Xe ions. (b) A PEELS spectra of the same are showing the presence of Xe.	21
2.6 (a) A dark field image taken after annealing the Xe implanted specimen. (b) A dark field image after further annealing showing the reduction in bulk defects. (c) A dark field image after more annealing which are indicative of ordering in the crystal.	22-23
2.7 (a) A schematic diagram of the original cartridge design employing a spring clip to hold the specimen in place. (b) A schematic diagram of the new design where to removable plates are used to hold the specimen in place.	25
2.8 (a) An on the zone diffraction pattern of the Ir (001) reconstructed surface. (b) An off the zone axis diffraction pattern of the Ir (001) (5x1) reconstruction.	27

2.9 (a) A dark field image of the Au (001) reconstructed surface that maximizes contrast from bulk features. (b) A dark field image of the same area taken with a diffracting condition that maximizes contrast from the surface.	31
3.1 An early stage diffraction pattern showing all of the general features exhibited by the reconstructed Au (001) surface reconstruction.	39
3.2 Shown are the higher index diffraction spots from the reconstructed Au (001) surface.	41
3.3 (a) Diffraction pattern showing the splitting of satellite spots around the {200} type diffraction spots. (b) A dark field image using the bulk {200} spots as well as the associated reconstruction satellite spots. (c) A blow of a {200} type bulk spot with the associated split satellite spots.	44-45
3.4 A Montage of diffraction patterns as a function of annealing time.	46-47
3.5 A Montage of dark field images taken with the {200} and surface satellite spots.	49-50
3.6 A schematic diagram of a possible shear structure shown in figure 3.5(a).	51
3.7 A dark field image taken with the {220} and surface satellite spots showing existence of several domains.	53-54
3.8 A high resolution showing both the '5' and 'n' dimension of the reconstructed surface.	55-56
3.9 A coincident site lattice construction of the (5xn) reconstructed surface.	57
4.1 Shown is a dark field image taken with the surface allowed {110} reflection and the associated reconstruction spots.	64

4.2 (a) A dark field image from a (5x n) reconstructed Au (001) single crystal thin film taken with a bulk {220} reflection and the associated reconstruction spots. (b) A dark field image taken under slightly different diffracting conditions which enhance the contrast from the surface relative to the bulk.	66-67
4.3 (a) A dark field image from a (5x n) reconstructed Au (001) single crystal thin film taken with a bulk forbidden {110} reflection and the associated reconstruction spots. (b) A dark field of the same area as 4.3 (a), but under slightly different diffracting conditions which make the fringes from the reconstruction more visible and contrast from the stacking fault less visible.	68-69
5.1 A schematic diagram of the Ir (001) two bridge model.	74
5.2 A montage of dark field images as a function of annealing time.	80-81
5.3 A bright field image showing a square hole which appeared after annealing.	82
5.4 A schematic diagram in reciprocal space showing the origin of the {1x1} type spots.	85
5.5 A dark field image of steps taken with the {1x1} spot.	86
5.6 A large magnification diffraction pattern of an Ir (001) reconstructed surface.	89
5.7 A high resolution image of the particles which can be identified as IrO ₂ .	92
5.8 A dark field image taken with a {200} and the associated reconstruction spots.	95
5.9 (a) A dark field image taken with the {200} and associated reconstruction spots near a dislocation. (b) A dark field image taken with the {200} and associated reconstruction spots near a profile surface.	97

6.1 The problem description located at a distance below a bimetallic interface.	105
6.2 The Case of a single dislocation which results as a limiting case of the solution for a dislocation near a bimetallic interface.	108
6.3 A plot of σ_{yy} at the free surface ($x=0$) as a function of distance along the free surface.	111
6.4 A schematic diagram of how to calculate the elastic potential E_p , for an edge dislocation below a free surface.	113
6.5 The elastic potential energy E_p , for an edge dislocation a distance of c below the free surface.	115
6.6 A plot of the energy of introducing a new dislocation into an material which already has a dislocation at c , E_{pintro} versus c .	116
6.7 A series of contours used to illustrate the summation scheme used to determine the functional form of σ_{yy} for the array of edge dislocations.	119
6.8 A plot of the convergence of σ_{yy_array} and σ_{yy} in the limit of large dislocation spacing as a function of distance along the free surface.	123
6.9 A plot of the dependence of σ_{yy_array} as a function of dislocation spacing d , versus distance along the free surface.	124
6.10 A plot of E_p and E_{p_array} in the limit of large d .	127
6. 11 A plot of E_{p_array} versus c for various values of d .	128
6.12 A plot of the activation energy of an epitactic overlayer versus misfit.	132
6.13 A plot of the critical thickness for the introduction of an edge dislocation a distance of c below a free surface, as a function of misfit.	133

CHAPTER 1

INTRODUCTION

The study of clean metallic and semiconductor surfaces has important implications for catalysis, electronic device fabrication and more recently, for the engineering of materials for space vehicles in low earth orbit. In particular, the study of the structure of clean surfaces has been given a considerable effort since they were found to reconstruct¹. The most commonly used techniques in the structure determination of reconstructed surfaces are the more traditional surface science techniques of low energy electron diffraction (LEED), reflective high energy electron diffraction (RHEED) and glancing angle X-ray diffraction. More recently scanning tunneling microscopy (STM) and ultra high vacuum transmission electron microscopy (UHV-TEM) have been used. LEED has been successful in determining the structure of reasonably simple reconstructions, but is difficult to use to determine more complicated structures such as the Si (111) (7x7) reconstruction². A kinematic interpretation of LEED patterns can be used to get an idea of the geometry and symmetries of surface structures but, cannot be used if accurate atomic positions of surface atoms are required. The reason for this is that in LEED, dynamical diffraction is the dominant mode of diffraction from the surface and as such, the interpretation of the intensity of LEED spots cannot be done directly³. It is not possible to directly take the inverse map of experimentally obtained diffraction

intensities to get surface atom positions as might be done by constructing a Patterson function³. In order to extract atom positions for surface structures, a set of most probable models must be assumed and the diffraction intensities from these models calculated for different voltages and angles of incidence. The best fit of the simulated diffraction intensities versus those obtained experimentally can then be used to determine surface atom positions to within the most applicable reliability or R factor.

RHEED suffers from a similar difficulty in the interpretation of recorded diffraction intensities and glancing angle X-ray studies suffer from the problem that, in order to get meaningful results, a synchrotron beam line is required to get the necessary photon flux of $\sim 10^{11}$ photons/sec⁴. A benefit of glancing angle X-ray investigations is that to a first approximation, the diffraction intensities from glancing angle X-rays can be interpreted kinematically⁵. RHEED and LEED suffer further from the fact that the signal obtained is spatially averaged, which makes the observation of irregularly stepped areas and other surface defects difficult⁶. It is therefore not possible to determine the local state of the surface, which might be done with a technique with higher spatial resolution. It is also not possible to obtain real space information from the surface using LEED, which would give more information on the orientation of reconstructed domains and their relationship to steps and other surface defects. Recently however, low energy electron microscopy (LEEM) has been used to image the Au (001) (5x20) reconstruction⁷. LEEM images are formed by using particular beams in a LEED pattern to form an image. The resolution of this technique is still low as compared to STM.

The advent of STM has made it possible to obtain real space images of reconstructed surfaces directly⁸. STM does have the inherent problem that it is in many ways too surface sensitive. In many cases, it is not possible to determine the relationship of surface reconstructed atoms to the bulk (1x1) surface, except in the case where interference patterns between the reconstructed surface and the bulk surface can be obtained.⁹ This is not a problem for reconstructions that occur in the space of one monolayer, but may pose significant difficulties for the case where the reconstruction affects several atomic layers of the bulk crystal.

In theory, surface information should be readily obtainable in transmission electron diffraction patterns (TED) and images with the added benefit of information of the bulk crystal between. Both real and reciprocal space information are available within the same experimental setup as well as the properties of the bulk crystal. Early TEM studies of surfaces were hampered by the less than adequate column vacuum that existed in commercial instruments. With the increasing availability of UHV equipment, it was possible to eliminate this problem. Bonevich and Marks¹⁰ and Marks et al¹¹ have previously explained the advances and requirements necessary to produce a truly ultra high vacuum transmission electron microscope and as such, will not be covered here. Instead, an emphasis on the application of existing UHV instruments to the preparation and observation of clean surfaces will be presented. Before launching into a full blown explanation of what has been done, let us first outline the requirements for the preparation of clean surfaces. Assuming one has a suitable ultra high vacuum environment, one has to be able to clean a surface that is brought into the vacuum; then one has to be able to

heat the surface and lastly, one has to be able to monitor the surface for contaminants without changing the UHV environment of the specimen.

The earliest functioning UHV-TEM was constructed by Honjo et al in 1977. This microscope was a modified JEOL 100B where a UHV section was inserted into the column^{11,12,13}. This microscope was primarily intended for nucleation and growth studies of evaporated films on clean substrates. As such, this microscope was at first fitted with evaporation units and a heating stage, and subsequently upgraded with a sputter ion gun¹⁴ and electron beam evaporation source¹⁵. The vacuum in the specimen chamber of this microscope was admittedly poor in the specimen preparation chamber with an initial pressure in the 10^{-8} torr range which could be reduced to the 10^{-10} torr range at the specimen with the aid of a cryoshroud^{12,14}. This was the first TEM capable of preparing surfaces by traditional sputter anneal cycles. Morita et al.¹⁴ were able to clean a Au thin film and Si crystal by ion bombardment. The cleanliness of the surface however, could only be maintained for a short period of time due to the vacuum constraints of the microscope. Since then, several microscopes have been developed which are capable of *in-situ* study of surfaces¹⁶⁻²². Many of these microscopes are based on the Honjo model and involve the modification of commercial microscopes either by the replacement of portions of the column, or the attachment of a UHV chamber to the side of an existing microscope. Several of the microscopes discussed in references 16-23 have been used to study the reconstructions of clean surfaces. Yagi and Takayanagi²³ and Nihoul et al.²⁴, have studied the reconstruction of Au (111) surfaces of small Au crystallites grown on MoS₂ and graphite substrates. Yamazaki et al.²⁵ have studied the reconstruction of the

Au (001) surface on similar crystallites grown on in situ cleaved graphite substrates. In the Au reconstructions studied by Yagi²⁶, Yamazaki et al.²⁵, the surfaces were prepared in a vacuum environment of 3×10^{-8} torr. The vacuum during the observation was reduced to the 10^{-9} - 10^{-10} torr range by use of a cryoshroud. The surfaces of the Au (111) and (100) crystallites could not be cleaned by any direct method such as ion bombardment. Gibson et al.²⁷ and Wilson and Petroff^{28,29} have studied the Si (7x7) reconstruction by cleaning bulk Si (111) single crystals by heating to temperatures in excess of 1000 °C. Most notably, Takayanagi et al.³⁰ have studied the Si (111) (7x7) reconstruction and determined the structure by analysis of the diffraction intensities. Up until the Takayangi et al.³⁰ study, the structure determination of the Si (111) 7x7 had eluded any complete determination by LEED. It can arguably be said that the structure determination of the Si (7x7) went a long way toward solidifying UHV-TEM as a technique for surface studies.

In general the above studies of surface reconstructions produced significant results but were to a large extent limited. The results on the Au surfaces were limited by the sample preparation. The surfaces of the crystallites could not be cleaned except by heating or by the creation of new surfaces. Heating of these samples would undoubtedly increase contamination of the surface by the outgassing of the substrate material. In the case of the results from the single crystal samples of Si (111) surface, the surface could be cleaned effectively by heating. It should be pointed out however, that the Si (111) surface is difficult to clean completely by heating due to the formation of SiC by reaction with hydrocarbons in the incomplete vacuum above the surface¹³.

While the studies represented above are a first step toward doing surface science using UHV-TEM, there is not much surface science that can be done on small crystallite islands and samples cleaned by heating alone. The studies above were aided by the fact that the surfaces of Au and Si are relatively insensitive to vacuum conditions. When contamination does occur, these surfaces can be cleaned or recreated for further study. What is required for the study of a wide variety of surfaces is the ability to use the sputter anneal cycles used in surface science preparations. The key element is the ability to achieve a truly UHV environment in the surface preparation chamber and microscope. To a first approximation, the definition of UHV can arguably be set as a base pressure below 10^{-10} torr. It should also be pointed out that a base chamber and microscope pressure at this level of vacuum are not sufficient. The important aspect is to have a controllable level of hydrocarbon and CO, CO₂ partial pressures while the microscope and specimen preparation equipment is operating.

At Northwestern a truly UHV microscope has been developed with a surface science chamber attached^{10,11}. The surface science chamber has the ability to clean surfaces by ion bombardment as well as to anneal the surface in an UHV environment. The intent of this thesis is to study clean, bulk single crystal surfaces which are prepared by traditional surface science sputter anneal cycles in UHV TEM. The method described can be used for metal, semi-conductor and oxide samples. Once the clean surfaces were obtained, the methods of surface imaging are examined and refined. The details of the specimen preparation and imaging techniques will be given in detail in chapter 2. The subsequent chapters will discuss specific results from Au (001) and Ir (001) single crystal

samples. Chapter 6 is a theoretical calculation of an array of edge dislocations near a free surface. This work was undertaken as a means to possibly explain how the misfit between a reconstructed overlayer and a bulk surface might be accommodated.

Before continuing, a word about UHV-TEM experimentation should be said. By the very nature of surface studies, the time under the best vacuum conditions for the observation of clean surfaces is limited. In most TEM investigations, one operator works on a given sample and if the pictures do not turn out the experiment can be repeated. In an average UHV experiment, the experiment runs for approximately 4 weeks and the same conditions cannot be repeated once the specimen is removed from the UHV-TEM. Consequently, large numbers of pictures have to be taken in a short period of time in order to obtain the required data to analyze the surface. In the following chapters, an average of 400 images per run was collected. As a result, no one operator could possibly take all the pictures for a given experiment. For chapter 3, most of the images presented were taken by J.P. Zhang and Professor L.D. Marks with contributions from the author. For chapter 4, the images presented were taken by Professor L.D. Marks and the author. The images for chapter 5 were chosen so as to all be taken by the author. The only image not taken by the author is the diffraction pattern shown in figure 5.4. The analysis of the images obtained were done mostly by the author with help where appropriate from Professor L.D. Marks.

The dislocation analysis seen in chapter 6 was begun under the advisement of Professor J. Dundurs in the Civil Engineering Department. The approach to the problem

as a limiting case of existing Airy stress functions and the Airy stress functions were given by him. The extension of the results to an array of edge dislocations is due to the author. The sums and integration were checked by Dr. Vitaly Volpert.

CHAPTER 2

EXPERIMENTAL EQUIPMENT AND METHODS

§ 2.1 INTRODUCTION

All of the experimental results described in the chapters to follow were obtained using ultra high vacuum transmission electron microscopy (UHV-TEM). In the past, UHV-TEM investigations of surfaces have been constrained to certain types of samples amenable to a particular microscope setup used. In particular, many investigations have been hindered by either insufficient vacuum conditions or the lack of available in-situ specimen preparation equipment. As a result, much of this work has been confined to surfaces that can be created by evaporation or constantly cleaned by sublimation. An example of this for metallic samples can be seen in the case of the Au (100) and (111) surfaces, which have been studied by evaporating small Au islands onto a MoS₂ substrate in the case of the Au (111)¹ surface, and evaporation onto small Ag islands in the case of the (100) surface². While it is possible to obtain a clean surface this way for a short time, size and substrate interactions produce strain effects that are not representative of the true Au (100) or (111) surfaces.

Work on semiconductor surfaces has mostly been confined to surfaces, such as the Si (111) surface, since this surface can be cleaned by subliming a bulk Si crystal until the

crystal is both clean and electron transparent. This technique for preparing surfaces is however limited. In order to study a large variety of materials surfaces it is necessary to be able to prepare a surface via traditional surface science sputter anneal cycles, and then examine these surfaces using TEM under a single contiguous UHV environment. In general, one has to be able to iteratively clean, anneal and examine a surface without removing it from the UHV environment.

A microscope fulfilling these requirements exists here at Northwestern University and has been documented in detail by my predecessors^{3,4}. The work described herein is largely second generation in that it assumes the existence of the UHV microscope and concentrates on the development and adaptation of the existing microscope to studying crystal surfaces with UHV-TEM.

§ 2.2 THE HITACHI UHV-H9000 MICROSCOPE

The Hitachi UHV-H9000 microscope consists of a modified side entry Hitachi H9000 high resolution transmission electron microscope with a small ultra high vacuum surface science chamber (SSC) attached. The microscope and SSC have a contiguous UHV environment with a stable operating pressure of $1-2 \times 10^{-10}$ torr. Figure 2.1 is a schematic diagram of the Hitachi UHV-H9000 transmission electron microscope. The microscope is a 300 keV transmission electron microscope equipped with a Gatan parallel electron energy loss spectrometer (PEELS) and a Gatan CCD off axis television camera.

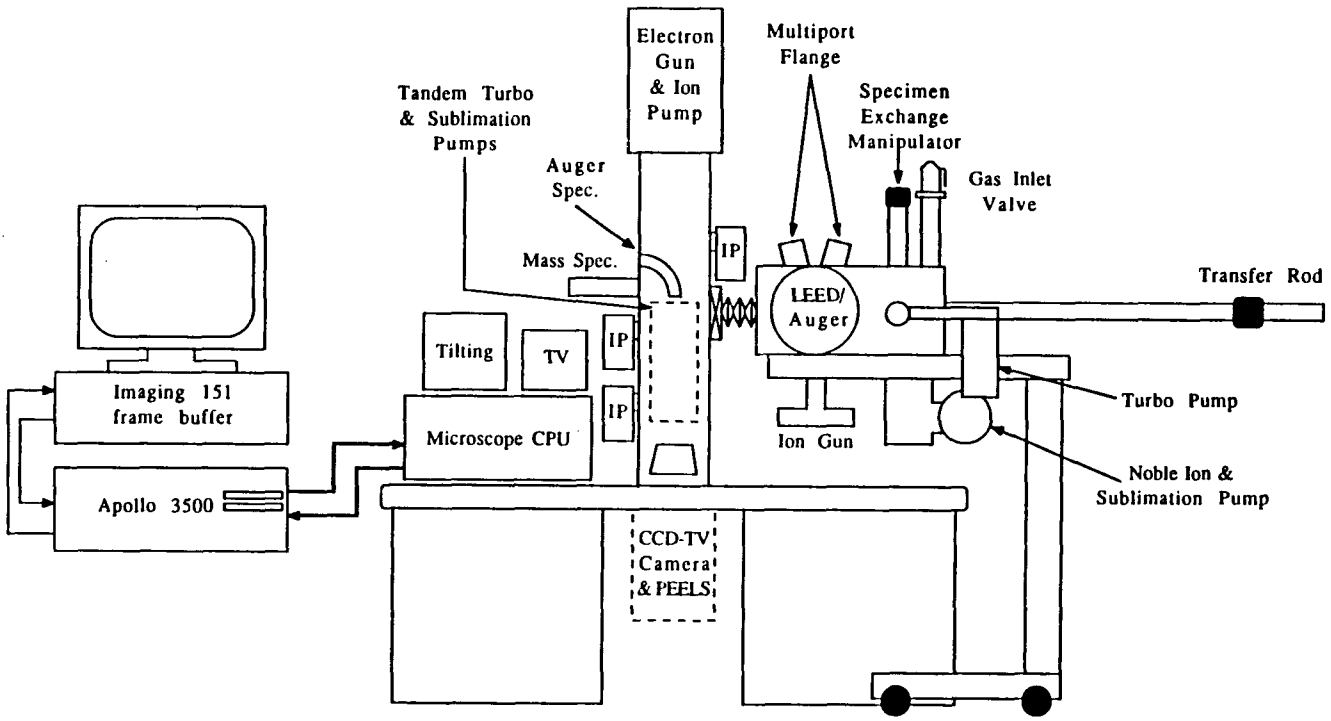


Figure 2.1. A schematic diagram of the Hitachi UHV-H9000 microscope and surface science chamber. (Courtesy of Dr. John Bonevich)

The UHV-SSC has a base pressure of $< 2 \times 10^{-10}$ torr and is equipped with a Perkin-Elmer 4 keV ion gun, a Kimball Physics 10 keV electron gun and a broad band optical annealing source capable of heating a metallic specimen to 600 °C.

A typical experimental run would begin by putting a bulk single crystal sample into the surface science chamber and baking the UHV-SSC until an acceptable vacuum is achieved. An acceptable vacuum is defined as the condition where the base pressure of the UHV-SSC is in the $1-4 \times 10^{-10}$ torr range, with a residual gas spectrum where the hydrocarbon partial pressures in the system are in the low 10^{-10} to 10^{-11} torr range. A test is then applied where the ion gun is run and the ion beam is used to hit the chamber walls. If the hydrocarbon mass spectrum, particularly the methane and carbon monoxide partial pressures, are higher than the 10^{-9} torr range, the chamber must be baked again. The reason for this is that during the specimen preparation process, ions from the ion gun can "scrub" the walls depositing hydrocarbon contamination on the surface of the specimen.

This sample would then be put into the microscope for initial examination. The bulk chemistry is probed for contamination from the specimen preparation outside the microscope using PEELS. The sample is then returned to the surface science chamber where traditional surface science sputter-anneal cycles are used to obtain a clean well ordered surface. The surface is then examined in the UHV-H9000 microscope and data collected in the form of transmission electron diffraction patterns, bright and dark field images as well as two-beam and high resolution images.

§ 2.3 SPECIMEN PREPARATION TECHNIQUE

The specimen preparation method developed has two distinct steps, the first of which occurs outside the microscope and the second occurs once the specimen has been placed in the UHV-SSC. Commercially available bulk single crystal specimens of Au and Ir were obtained and spark cut into 3 mm disks. These disks were then mechanically polished using standard metallographic techniques to a total thickness of roughly 30 μm , starting with 15 μm diamond paste and ending with 0.3 μm alumina paste. The disks were then ion milled using 3 keV Ar⁺ ions with a take off angle of 11° until the disk was nearly perforated. Once the disk was thinned, it was initially examined in the Hitachi H9000 high resolution transmission electron microscope to ensure that the sample was electron transparent and still single crystal with the proper orientation.

Once an acceptable disk is made, it is placed into the UHV-SSC and the chamber baked to achieve the proper vacuum conditions. After baking the sample is then placed in the microscope and examined using TEM and PEELS. PEELS was used to ensure that there was no implanted Ar, remanent from the ion milling process outside the vacuum, as well as to look for other sources of contamination, such as embedded diamond and alumina pastes. The sample is then put back into the SSC where it is first ion milled, to either thin the disk further or to clean the surface. The specimen is then rechecked in the microscope using PEELS and TEM. TEM is quite sensitive to hydrocarbon contamination and coverages as low as 10 monolayers can be seen. This process of ion milling and checking for contamination is repeated until the crystal is clean to the detection limit of both PEELS and TEM.

The sample is then annealed using either the broad band optical annealing source or the Kimball physics 10 keV electron gun. The electron gun is the preferred method of annealing, since a true local heating can be obtained. The broad band optical annealing source suffers from the problem that it cannot be focussed into a small enough beam to heat only the sample. As a result, the cartridge and parts of the chamber heat up, which drive adsorbed gases off the chamber walls and cartridge, subsequently contaminating the clean surface.

After annealing, the sample is then put back into the microscope and examined using both the PEELS and TEM. This cycle of ion milling and annealing is repeated until a well ordered surface is obtained. The sample preparation scheme described above can be used to prepare most metallic and semiconductor surfaces, as well as those of oxides with slight modification; which is to anneal the specimen in the proper partial pressures of O₂ to maintain stoichiometry.

In developing the specimen preparation technique described above, one of the key questions that had to be addressed was how to prepare the initial bulk single crystal disk outside the SSC. The process of surface preparation once an electron transparent single crystal specimen is prepared is simply a straight forward application of sputter anneal cycles. The process of preparing the initial electron transparent single crystal disks was however not as clear. While techniques such as electropolishing and jet polishing for preparing thin metallic foils are well known, they cannot in general be applied to single crystal specimens for UHV-TEM. The reason for this is two fold. First, both jet polishing and electropolishing are trial and error techniques which require many tries to

get a single specimen. This poses no problem for systems where a large quantity of specimen material is available but for single crystal precious metals, the cost of trial and error is prohibitive. Secondly and more importantly, chemical and electrochemical thinning processes generally leave a reaction layer consisting of intermediary bi-products, which end up as thin contamination layers on the surface of the specimen. While this is not a problem in more traditional TEM studies, it is a problem for UHV-TEM. In many cases, these intermediary compounds are very stable and difficult to clean off with typical UHV grade cleaning solutions. Also, because these intermediary compounds are stable, they are difficult to get rid of by ion milling in the SSC. In the case of a Au (111) single crystal prepared by jet polishing in a 35 % ethanol, 15% glycerine and 50% KCl solution⁵, a particularly tenacious Au-organic intermediary was formed that could not be cleaned off with HF or ion milling. Other jet polishing solutions that perhaps are cleaner, such as the commonly used HCN based solutions, might be used but were not because of safety constraints and the lack of a sufficient number of specimen blanks necessary to get the conditions correct. There is also no guarantee that this polishing process would not produce equally tenacious intermediary bi-products such as those encountered in the KCl based solution. It is because of these contamination problems that we chose to stick with traditional metallographic polishing techniques for the preparation of electron transparent single crystal blanks. While traditional mechanical polishing techniques do introduce more crystal defects than chemical thinning techniques, this is not crucial since the defect concentration can be reduced significantly during the annealing portion of the *in situ* surface preparation process.

Before we could make full use of the existing surface preparation equipment, several calibrations and modifications to existing equipment had to be made. The first calibration that was done was with the Perkin Elmer ion gun. Since the specimen is held in a Be-Cu cartridge, it is necessary that the beam size and focus values of the gun be determined to prevent sputtering of the cartridge material onto the specimen. A strip of aluminum foil covered with phosphor was attached to a blank cartridge with a 3mm disk scribed in the position where the specimen would normally be. This cartridge was placed in the SSC and the chamber pumped down. The ion gun was then run and the beam was focussed to fit well inside the scribed 3 mm disk and the focus value recorded as a function of voltage. Figures 2.2 a and b are the focus values versus voltage curves for Xe and Ar sputtering gases.

The next thing that had to be calibrated was the temperature versus amperage curve for the optical annealing source. It is not possible to attach a thermocouple to the sample for every experiment, since the thermocouple material would easily be sputtered onto the sample during ion cleaning and thinning. The sample also has to be able to move in and out of the microscope, which makes attaching a thermocouple to it difficult. The setup for calibrating the optical annealing source is similar to that used to calibrate the focus values for the ion gun. The difference here is that a cartridge was loaded with a used Au (100) single crystal specimen instead of a blank. The specimen had a chromel-alumel thermocouple spot welded to its center. The broad band optical annealing source was then set as shown in figure 2.3. The power of the optical annealing source is increased by increasing the amperage to the lamp so, the temperature of the specimen was recorded

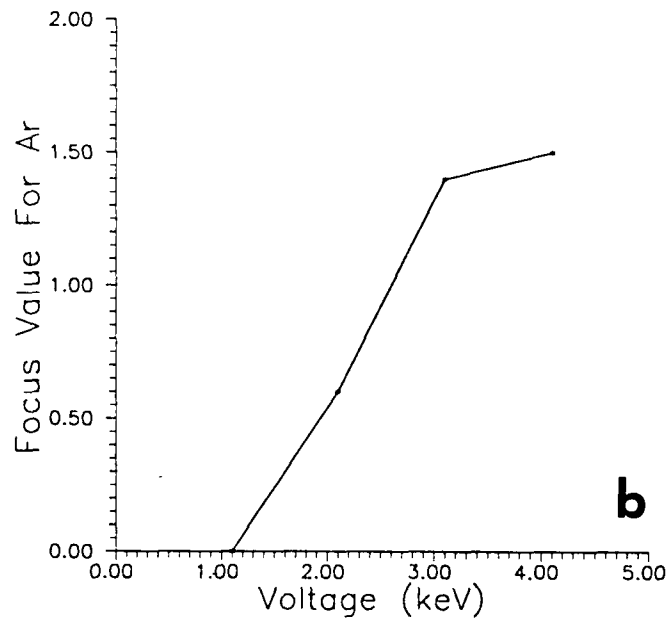
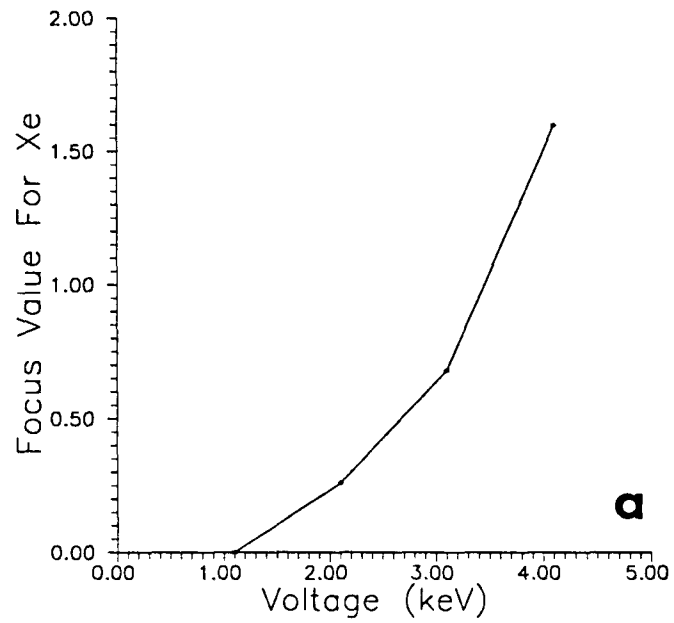


Figure 2.2. (a) Plot of focus values versus voltage for the Perkin Elmer ion gun using Xe gas. (b) Focus values versus voltage for the Perkin Elmer Ion gun using Ar gas.

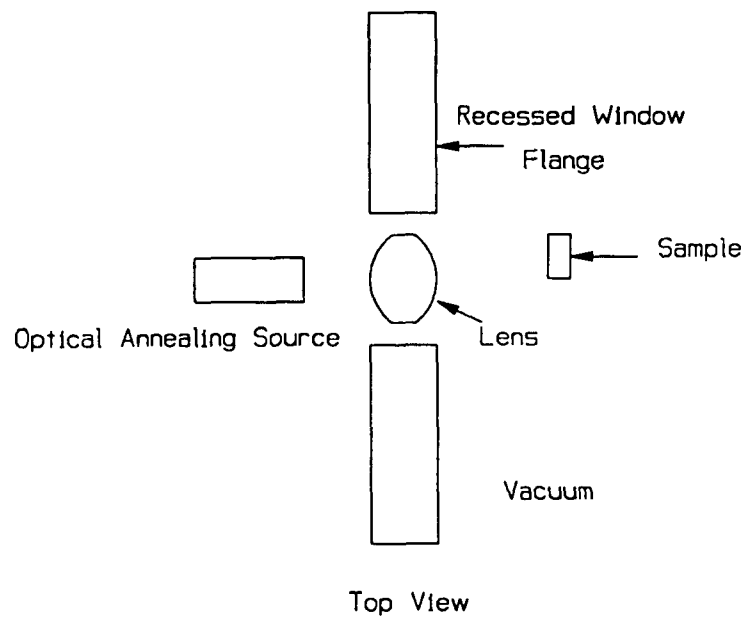


Figure 2.3. Schematic diagram of the setup used to anneal a specimen in the SSC with the broad band optical annealing source.

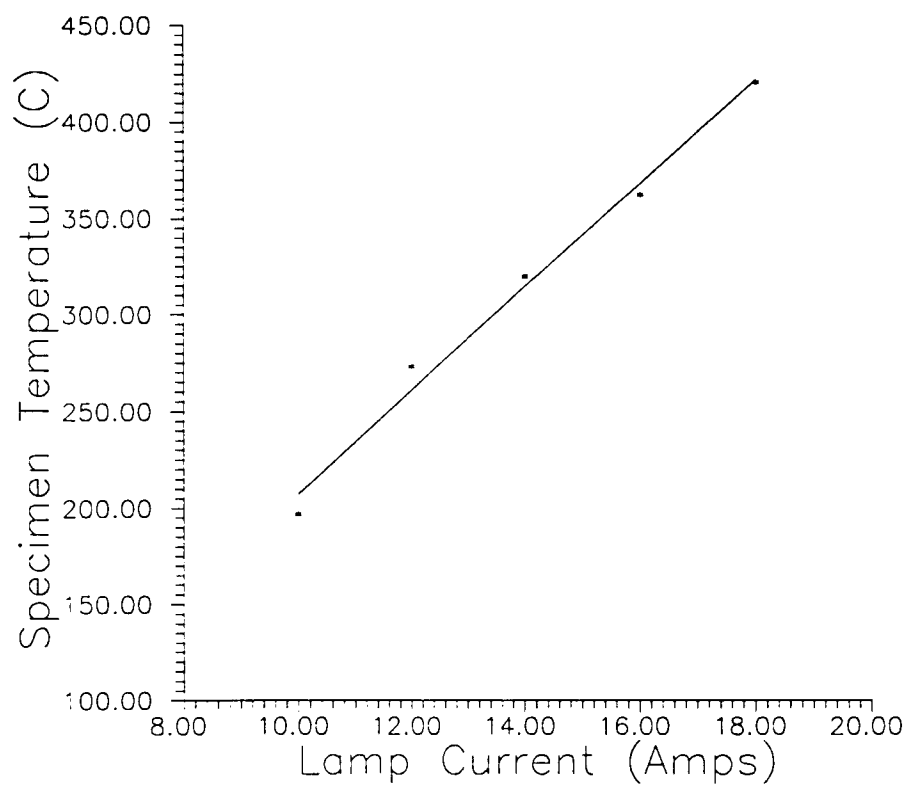


Figure 2.4. A plot of the temperature versus lamp voltage for the broad band optical annealing source.

versus lamp amperage. The temperature at each setting was allowed to equilibrate for at least 30 minutes. If a stable temperature was not reached after 30 minutes, the lamp was left at that setting until the temperature no longer fluctuated. Shown in figure 2.4 is the temperature versus amperage plot of the optical annealing source, where the temperature can be seen to be approximately a linear function of amperage. The maximum temperature obtainable for this setup is 625°C for metallic specimens. The Kimball Physics 10 keV electron gun was not calibrated in a similar way, but specific temperatures can be measured using an optical pyrometer when necessary.

When we first began preparing surfaces using traditional surface science sputter anneal cycles, the cleaning process was constrained by the specimen cartridge design. The as received cartridge would not allow the specimen to be tilted to reduce the incident angle of the ion beam to less than 90°; thus, the probability of implanting ions into the sample during thinning and cleaning was very high. In fact, during the preparation of the first Au (001) bulk single crystal, a significant amount of Xe was implanted into the sample. Figure 2.5a shows a bright field image of the sample just after thinning with 4 keV Xe ions. The Moire fringes seen in the image are due to the presence of a substitutional Xe lattice on the Au (001) parent lattice. Figure 2.5b is the accompanying linear mode PEELS spectrum showing a strong Xe edge in the bulk crystal. By simply annealing, the Xe could be driven out of the sample and much of the damage caused by implantation removed. Figures 2.7a and 2.7b are dark field images of the same sample after different stages of annealing. After a short anneal, the implanted Xe was removed, as can be seen in figure 2.6a. From figure 2.6a it is clear that the crystal has a high

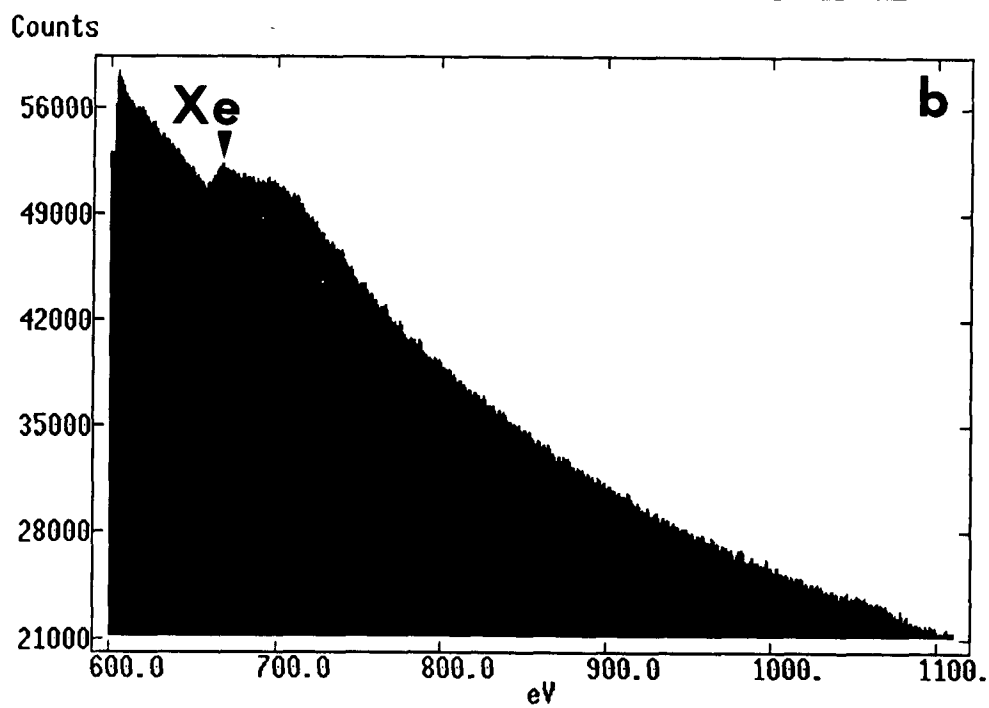
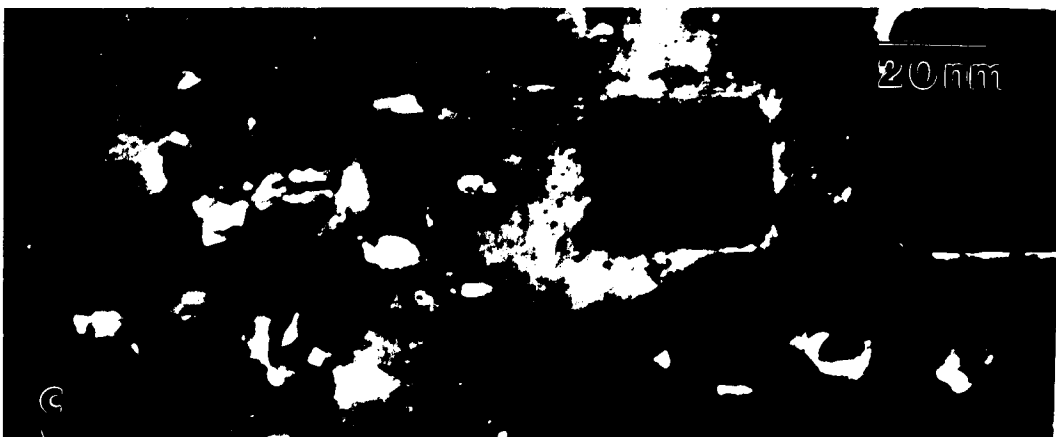
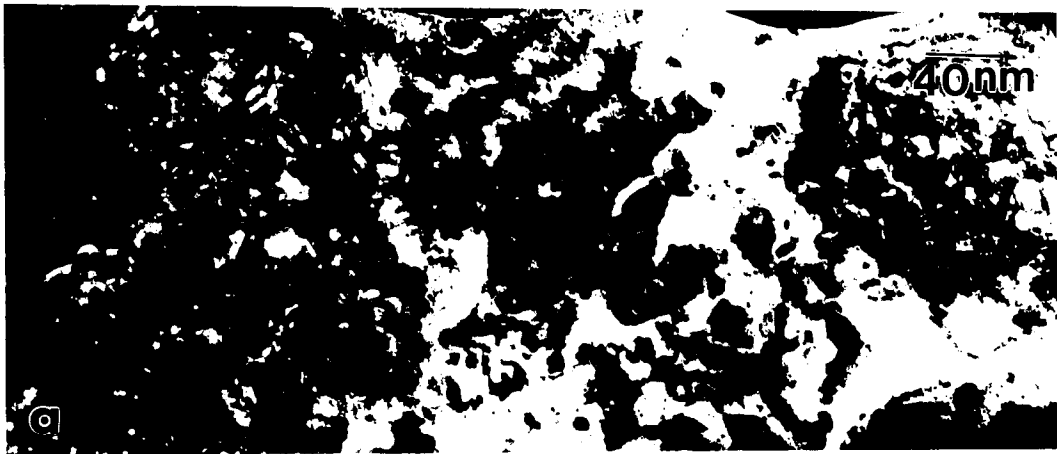


Figure 2.5. (a) A bright field image of the Au sample after ion milling with 4 keV Xe ions. The fringes running diagonally across the image are Moire fringes from implanted Xe. (b) A PEELS spectra of the same area showing the presence of the Xe.

Figure 2.6. (a) A dark field image taken after annealing the Xe implanted specimen. At this point the crystal is still heavily damaged. (b) A dark field image taken after further annealing showing the reduction in bulk defects. Some dislocations are still present. (c) A dark field image after more annealing showing square holes which are indicative of ordering in the crystal. Bulk defects can still be seen but in reduced concentration.



concentration of defects. After further annealing, the defect concentration can be reduced considerably as can be seen in figure 2.6b. After the annealing time represented by figure 2.6c, the crystal has begun to order, as is evidenced by the square holes seen in the center of the image. It should be pointed out that the squaring of holes in a sample has been observed to accompany ordering in the crystal and is found to precede the reconstruction of the surface.

In order to reduce the implantation probability and the chance of sputtering Cu from the cartridge onto the sample during thinning and cleaning a new specimen cartridge was designed. Shown in figure 2.7a is the original 3 mm design employing a spring clip to hold the specimen in place. To allow the angle of incidence for the ion gun to be reduced, the spring clip had to be eliminated as well as the material near the sides of the cartridge. Figure 2.7b is the redesigned cartridge that was built. Instead of holding the sample with a spring clip, it is held in place with two plates fastened from the top of the specimen. This means that the cartridge can be tilted to a wider range of take off angles without sputtering the cartridge and spring clip materials onto the specimen.

With the current setup, we are now routinely able to prepare and clean surfaces of metals and semi-conductors in a relatively short period of time. The original Au (001) sample took a month to prepare while recently in the work of Marks and Savage^{6,7,8}, we were able to prepare a Si (111) surface in roughly a week's time.

§ 2.4 IMAGING TECHNIQUES

The techniques for obtaining surface sensitivity in TEM images are well known¹⁹⁻²³. The two most widely used techniques for obtaining surface sensitivity in conventional TEM investigations are weak beam imaging and the method of forbidden reflections or Cherns' technique⁹. Weak beam images are obtained by first tilting to an off the zone axis diffracting condition and then using centered dark field imaging techniques to produce the image. The reason that an off the zone axis condition is used is because a kinematically diffracting condition can be established, which increases the ratio of intensity due to surface features to bulk diffraction intensity in the image. The reason for this is that under kinematical diffracting conditions, electrons emerging from the exit surface of the sample are assumed to have been scattered only once. Under these conditions, many more electrons scattered from the surface make it to the image plane, thus increasing the intensity from surface features. In a dynamical diffracting condition, the electrons scattered from the surface may be rescattered in the bulk crystal and lost to inelastic scattering processes. An example of this can be seen in the diffraction patterns in figure 2.8. Figure 2.8a is an on the zone axis diffraction pattern of the reconstructed Ir (001) surface. Near the bulk {200} type reflections are large plumes of diffraction intensity largely due to plasmon scattering and other inelastic scattering events. These intensity plumes are covering the 1/5 th order reconstruction spots near the { 200 } spots. If the crystal is then tilted of the zone axis, as is seen in figure 2.8b, the plasmon plumes are seen to be reduced in size and the 1/5 th order surface reflections are seen much more clearly. A typical weak beam image would be formed by tilting the spot required in

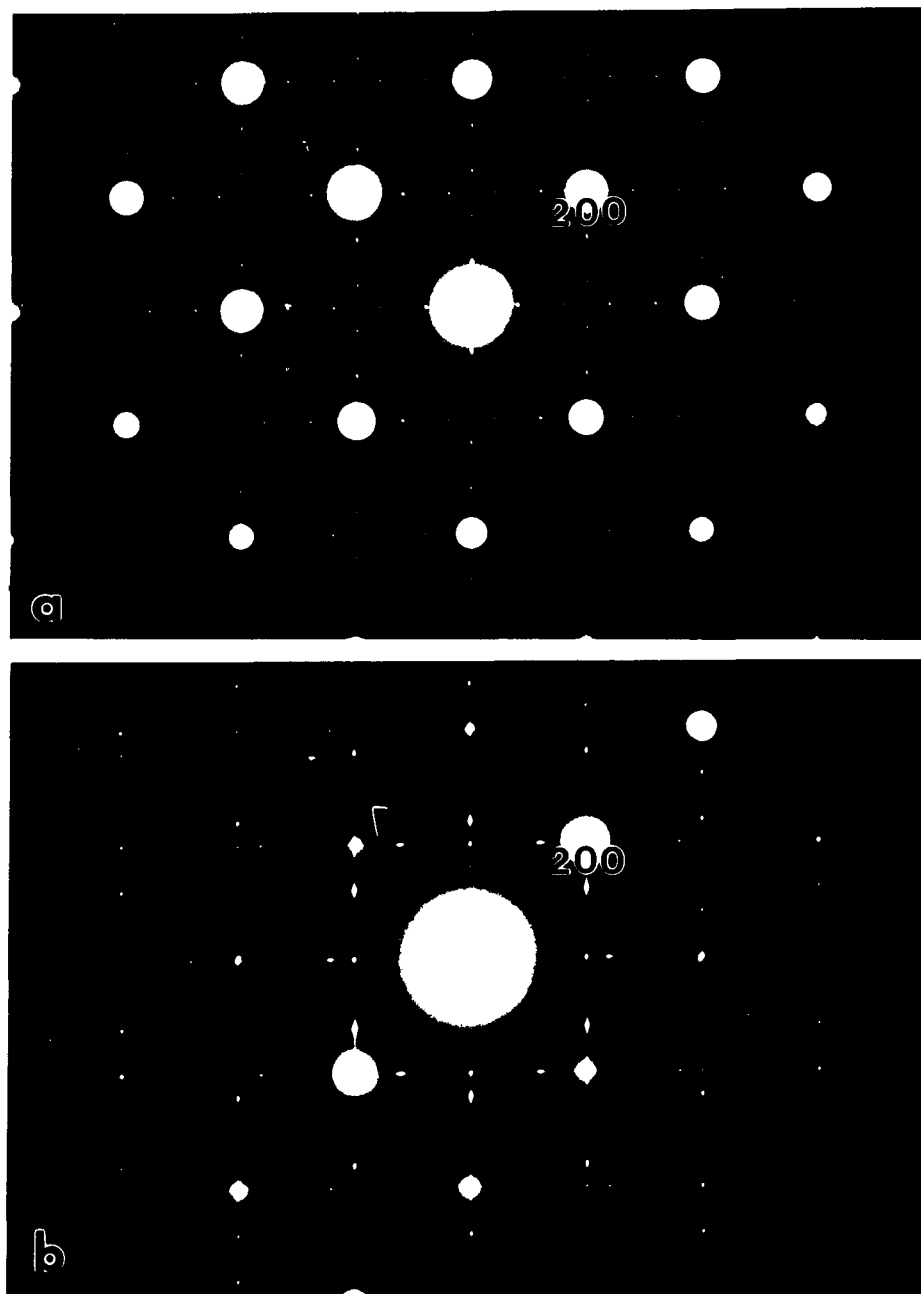


Figure 2.8. (a) An on the zone diffraction pattern of the Ir (001) (5x1) reconstructed surface. The 1/5 th order diffraction spots are obscured by inelastic scattering around the {200} spots. (b) An off the zone axis diffraction pattern of the Ir (001) (5x1) reconstruction which has reduced the intensity due to inelastic scattering thus, making the 1/5 th order spots visible (arrowed).

diffraction mode to the center of the screen, centering the spot in the objective aperture and returning to image mode for observation. Another true benefit from using a kinematic diffraction condition is that image interpretation is much easier than in images taken under more dynamical conditions.

In theory, weak beam images offer an attractive method to image surfaces in plan view, but suffer from the fact that to take good weak beam images requires a process of trial and error. This is not necessarily a critical concern using traditional microscopes, because the experiment can be repeated in a short time. In UHV-TEM, this can be disastrous since an experiment may take 4-6 weeks to repeat.

A second commonly used technique is the method of forbidden reflections or as it is sometimes referred to, Cherns' technique. Cherns⁹ reasoned that increased surface sensitivity can be obtained in systems where surface features arise from incomplete stacking sequences in bulk structures. If the structure factor for a system with an incomplete stacking sequence is evaluated, formerly forbidden reflections now have non-zero intensities and if these forbidden reflections are used to take dark field images, true surface sensitivity can be obtained. In the case of Cherns' technique, it is not necessary to establish a kinematical diffracting condition to obtain adequate contrast from surface features. Cherns' technique has been used successfully to investigate surface reconstructions such as the Si (7x7)¹⁹ and surface steps in the oxidation of Si (7x7) surfaces²⁴. The method of forbidden reflections is a useful technique to maximize surface contrast in plan view images, but the true scattering processes responsible for surface contrast under dynamical diffracting conditions have yet to be explained

adequately. Much of the practical interpretation of images using Cherns' technique rely on kinematical concepts.

In an effort to explain the intensity from surface diffraction, Peng and Whelan²⁵ have devised an explanation for the intensity levels of surface reconstruction spots in transmission electron diffraction patterns using a dynamical diffraction formulation. The idea is that for certain conditions of surface potential, the reflections from the reconstructed surface can be either coupled or decoupled from the bulk reflections. If the surface reflections are decoupled from the bulk reflections, the intensity levels reaching the diffraction plane from the surface will in general be higher relative to the bulk intensity. If however, the surface reflections are coupled to the bulk reflections, the intensity from surface reflections will be swamped by the bulk reflection intensities. While this is a good phenomenological step toward the true explanation of the dynamical formulation of surface contrast, it does not offer quantitative explanations for specific systems. Peng and Whelan's²⁵ formulation represents a qualitative explanation, but fails to clearly define the conditions for surface potentials that couple or decouple surface reflections from the bulk. In the work described herein, we have used a two prong method for examining surfaces in plan view. Transmission electron diffraction patterns (TED) and bright and dark field imaging are used together under different diffracting conditions to investigate surfaces. TED patterns contain all of the information necessary for determining the dimensions and geometry of a reconstructed surface relative to the bulk terminated surface. Tilting off the zone axis to a kinematical diffracting condition maximizes the diffraction intensities from the surface in question.

Imaging techniques are able to provide local information about the surface. A wide range of imaging techniques are used to examine the surface of the crystal. Dark field imaging both on and off the zone axis are used to examine different kinds of features. Rather than list the diffracting and imaging conditions required to image a given combination of surface and bulk features, it is better to understand the tools for imaging. Imaging in UHV-TEM can be considered as a process of tuning diffracting and imaging conditions to maximize contrast and intensity for a given feature. If the feature in question is a surface feature, then tilting off the zone axis and using weak beam dark field or Cherns' technique should be used. If however, one wants to look at a bulk defect such as a stacking fault, dark field images in an on the zone axis or two beam diffraction condition could be used. If one wanted to examine the interaction of bulk defects with surface reconstructions, then a range images must be used where the diffracting condition is varied from bulk sensitivity to surface sensitivity. Figure 2.9 is a pair of dark field images taken from a (5x n) reconstructed Au (001) thin film samples. Central in both 2.9a and 2.9b is a stacking fault and the heavier Moire fringes seen are from the n dimension of the reconstructed unit cell. Figure 2.9a is taken with a diffracting condition that maximizes the contrast from the stacking fault while still maintaining a minimum intensity from reconstructed features. Figure 2.9b is a dark field image of the same area taken with a diffracting condition that maximizes the contrast from the reconstructed surface. Roughly normal to the Moire fringes from the n dimension of the reconstructed unit cell, there can be seen finer fringes which are from the '5' dimension which were not visible in 2.9a.

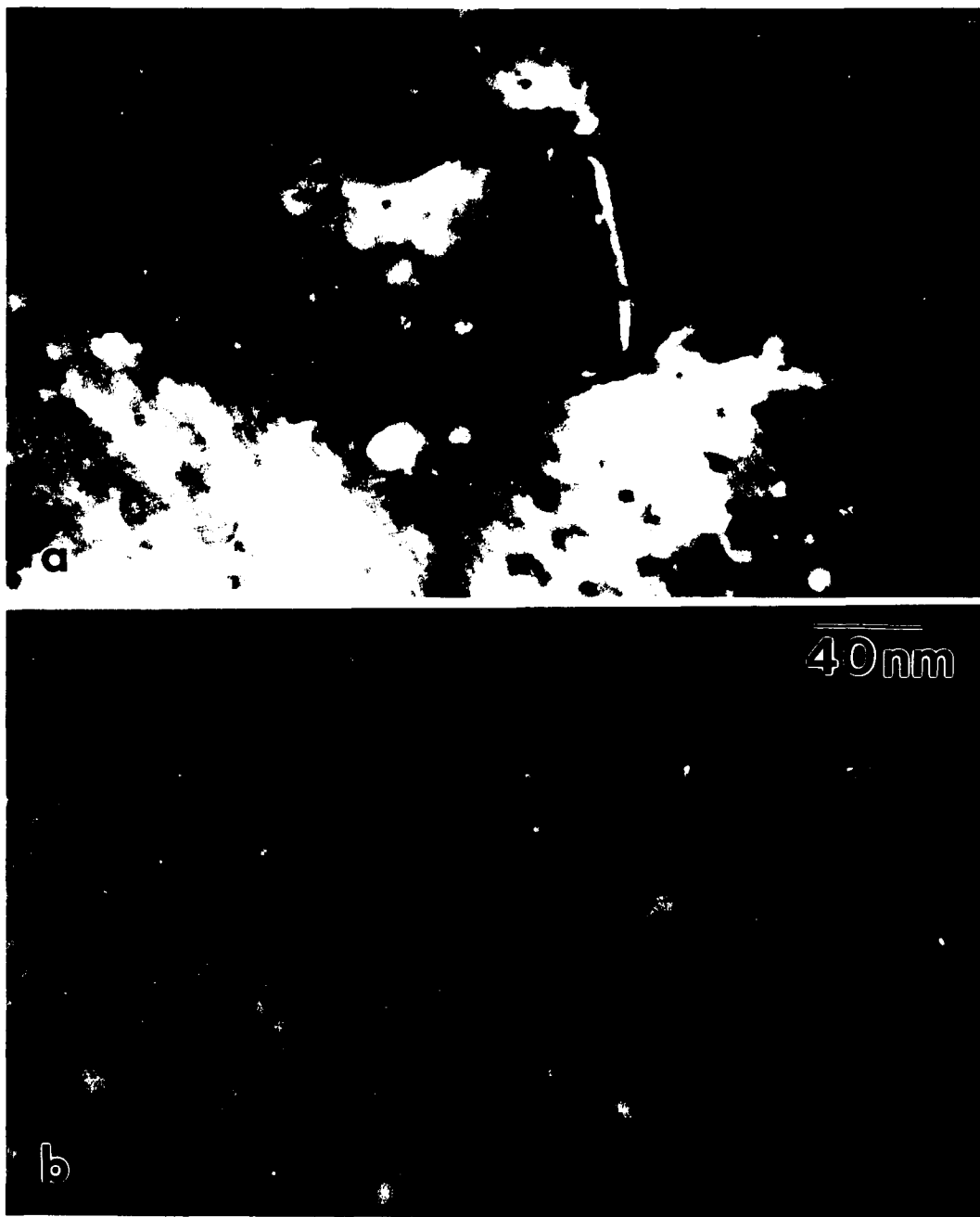


Figure 2.9. (a) A dark field image of the Au (001) reconstructed surface that maximizes contrast from bulk features. (b) A dark field image of the same area taken with a diffracting condition that maximizes contrast from the surface.

CHAPTER 3

UHV MICROSCOPY OF THE RECONSTRUCTED AU (001) SURFACE

§ 3.1 INTRODUCTION

The Au (001) surface was the first bulk single crystal specimen we chose to study in the UHV-H9000. As such, the choice of a bulk Au single crystal specimen represented not only a new experimental area for the UHV-H9000 but, more importantly, until this work was done, no bulk single crystal Au surface had been prepared much less reconstruct using UHV-TEM. The Au (001) surface also served as a calibration standard in the development of both imaging and specimen preparation techniques for UHV-TEM studies of clean surfaces. As was pointed out in chapter 2, the UHV-H9000 is the first truly UHV-TEM that has the capability to prepare surfaces via traditional surface science sputter-anneal cycles, as well as to image these surfaces all *in situ*. Aside from the fact that it had never been done before, we chose to begin with the Au (001) surface for three main reasons. The first reason is that the Au (001) surface is a very forgiving surface from a materials standpoint. Au (001) can in many ways be considered an ideal surface from a contamination point of view because, it has a very low sticking coefficient at room temperature for common vacuum contaminants such as CO, CO₂ and H₂O. Au also possesses mechanical properties that afford one the possibility of annealing out defects

incurred by the initial specimen preparation and ion milling during surface preparation.

The second reason why we chose the Au (001) surface had to do with TEM imaging requirements once a reconstructed surface is established. It should be remembered that at the time, the only imaging techniques that were thought to be useful in achieving surface sensitive plan view images were weak beam dark field imaging and dark field imaging using the surface allowed 1x1 spots (Cherns' Technique). Also, the reconstructed Au (001) surface is easier to image than many others because it has a large surface unit cell. Images could be taken at lower magnifications, which would serve to maximize the intensity from surface features in weak beam images. At the time it was thought that intensity from surface features would be considerably smaller in magnitude than intensity from bulk diffraction, which is one of the key motivations for using weak beam imaging to look at surfaces.

The third reason why we chose the Au (001) surface to examine first was because the Au (001) reconstructed surface was not well understood. Up until we began work on this surface, most of the work that had been done utilized more traditional surface science techniques such as reflective high energy electron diffraction (RHEED), low energy electron diffraction (LEED), positive ion channeling spectroscopy (PICS) and more recently TEM and scanning tunneling microscopy (STM). These techniques determined a wide variety of reconstructed unit cells ranging in dimension from (5x1) to c(26x68). We wanted to look in particular at the reason why there is so much variability in results and also what, if any, interaction existed between the reconstructed surface and the bulk crystal.

§ 3.2 BACKGROUND

It has long been known that clean surfaces of Au will reconstruct into a variety of different surface configurations. The first evidence presented for the reconstruction of the Au (001) surface was given by Fedak and Gjostein¹, who found using LEED that it reconstructed into (5x1) surface cells. Several authors since then have investigated the Au (001) surface using LEED and found that it reconstructs into (5x1)^{1,2}, (5x20)^{3,4,5} and c(26x68)⁶ surface cells. Grønlund and Nielsen have found the Au (100) surface to reconstruct into two (5x20) orthogonal domains using RHEED⁷, while Reider et al.⁸ found a (5x1) surface cell using He diffraction techniques. Scanning tunneling microscopy (STM) studies have determined that the Au (001) surface reconstructs with a dominant (5x1) periodicity, which can be distorted into much larger cells by rotations and a contraction of roughly 4 % in the reconstructed surface layer⁹. More recently, a (28x5) reconstructed cell was found by Yamazaki et al.¹⁰ for the Au (001) surface using ultra-high vacuum transmission electron microscopy (UHV-TEM). In most of the previous investigations of the reconstructed Au (001) surface, some common elements appear. Firstly, in all but one of the LEED studies above⁶, one dimension of the reconstructed cell was found to be 5 times the bulk F.C.C. spacing, while the other dimension of the cell is always less precisely known. Also in most of the models proposed to explain this reconstruction it is assumed that the reconstructed layer is hexagonal and has a spacing contracted from the bulk F.C.C. (111) spacing¹. It has also been pointed out by several authors^{6,7,9,10,11} that the reconstructed Au (001) surface is not commensurate with the bulk lattice and is found, in most cases, to consist of domains rotated with respect to the bulk

lattice. He diffraction and positive ion channeling spectroscopy (PICS)¹¹ have demonstrated that the reconstructed layer is on the order of a single monolayer in thickness.

It was thought early on that the surface reconstructed due to the segregation of impurities to the surface from the bulk^{1,2}. This prompted subsequent studies of the clean Au (001) surface using Auger electron spectroscopy (AES) to ensure the cleanliness of the surface being examined¹¹. The clean Au (001) surface was found to reconstruct into (5x20) surface domains while the (1x1) surface is found only when contamination is present¹².

Since much of the work to date on the Au (001) surface has been done using standard surface science techniques, relatively little has been said about the effect of bulk properties on surface reconstruction. Earlier work using UHV-TEM by Yamazaki et al.¹⁰ concentrated on thin film islands of Au grown on a Ag islands sitting on a graphite substrate. While the work done by Yamazaki et al.¹⁰ represents one of the first efforts by UHV-TEM to study the Au (001) reconstructed surface, it is limited in several ways. The first limitation is that the vacuum conditions in the microscope are borderline for clean surface studies (Pressure in the microscope is 3×10^{-8} torr). There is a cryoshield around the specimen to slow contamination rates, which is a patch method at best. If there is any heating of the sample to anneal the surface, the cryoshield will quickly become saturated with vacuum contaminants, rendering it an ineffective means of controlling contamination on the specimen. Secondly, there is no method mentioned for cleaning the surface once contaminated other than heating the sample, or the creation of

new surfaces by evaporation. During the heating of the sample, the graphite substrate will most likely be a constant source of carbonaceous contamination. Finally, since the surfaces studied are those of small islands, the strain fields due to substrate interactions call into question whether this sample is truly representative of a Au single crystal surface.

It is the intention of this chapter to present results using UHV-HRTEM on bulk Au (001) single crystal samples, where the surface is found to reconstruct in the presence of a non-trivial concentration of bulk defects. In particular, the differences in previous reports on the detailed structure of this surface are explained as a consequence of different annealing and preparation conditions.

§ 3.3 EXPERIMENTAL

The specific details of the specimen preparation technique used to obtain clean, well ordered, Au (001) surfaces were given in chapter 2. There are however some slight differences between the technique outlined there versus that used here. Two types of samples were examined, a bulk Au (001) oriented single crystal followed by a Au thin film for comparison. Since the bulk single crystal sample was the first single crystal specimen on which we attempted to establish a reconstruction, we wanted to determine the limits of our *in situ* specimen preparation. More specifically, we wanted to see if it was possible to start with a blank specimen that was not electron transparent, thin it to electron transparency and then establish a well ordered Au (001) surface. We have subsequently found that it is better to begin with thinner, electron transparent samples,

rather than try to thin the specimen in the SSC. The reason for trying to do the final thinning in the SSC was that it is cleaner, since it could be done by ion milling in an UHV environment. The problem is however, that the existing Perkin Elmer ion gun has too low an ion current to be an efficient thinning tool. We also did not have the Kimball Physics electron gun mentioned in chapter 2, and were forced to use the optical annealing source to anneal the surface. The optical annealing source is not the best way to anneal surfaces because it heats up not only the specimen but also the surrounding cartridge material, thereby increasing the risk of recontaminating the clean surface.

Bulk Au (001) oriented single crystals were obtained from Atomergic Chemical Company and were spark cut into 3 mm disks. As was described in Chapter 2, these disks were first mechanically polished using standard metallographic techniques, and then dimpled so that the thickness at the dimple was 30 microns. These specimens were then cleaned and placed in the SSC of the microscope, where the crystal was sputtered with 4 keV Xenon ions until transparent to 300 keV electrons. The crystal was then checked for contamination using PEELS and UHV-HREM. Initial examination with linear mode PEELS showed that after the initial ion milling with 4 keV Xenon, a significant amount of Xe had been implanted in the specimen causing line and point defects to appear in the bulk crystal. It should be pointed out that presently we are able to use our PEELS spectrometer not only in linear but in differential mode, thereby substantially increasing our sensitivity to contaminants. The specimen was then annealed until the Xenon was no longer detectable to the PEELS and the bulk defect concentration had been reduced to acceptable levels.

The crystal was then cleaned with 2 keV Xe ions and annealed with the optical annealing source at 340 °C. This process of sputter cleaning with low energy Xe ions and annealing was repeated until a clean, well ordered, (001) reconstructed surface was obtained. Once the reconstruction was established, the surface was re-cleaned and re-annealed for varying times to investigate the effect of annealing on the material. The Au thin film sample required no preparation outside the vacuum and the surface was prepared in the same way as the bulk single crystal sample, except that the Kimball Physics electron gun was used to anneal the surface.

§ 3.4 RESULTS

The results of this experiment will be broken up into a discussion of the basic features of the reconstructed Au (001) surface, followed by an analysis of the domain structure. These two will be tied together in the discussion section, where we show that the large variation in results can be understood within a simple model based upon local variations in the bulk strain fields.

§ 3.4.1 BASIC CRYSTALLOGRAPHY OF THE RECONSTRUCTION

Before describing the various forms of the reconstruction that were observed, it is important to detail the basic elements. Let us first begin by discussing the diffraction pattern shown in figure 3.1 which demonstrates the basic elements of the reconstruction.

The background in all cases is a bulk (001) crystal, which produces a square reciprocal lattice mesh with diffuse structure in the diffraction pattern arising from bulk defects. In

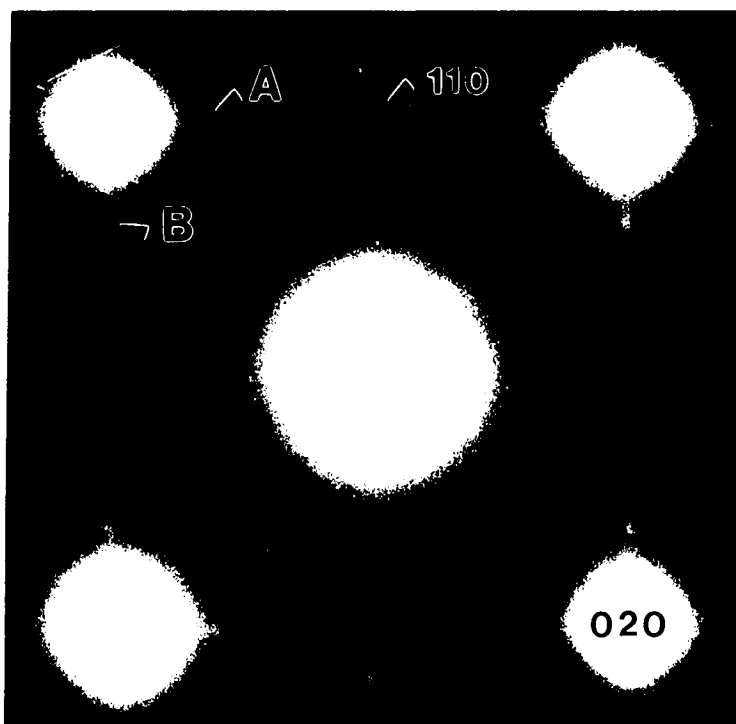


Figure 3.1. An early stage diffraction pattern showing all the general features exhibited by the Au (001) reconstructed surface. A and B demarcate satellite spots from the reconstructed surface, and a surface allowed {110} type spot is also labelled.

addition to the bulk spots, diffraction from the surface mesh (e.g. $\{110\}$ diffraction spots) is also present in the diffraction patterns. It is important to recognize that these spots are due to an incomplete number of (001) layers along the beam direction and as such are both bulk and surface sensitive; a bulk defect can lead to an incomplete number of layers as readily as a surface step, for instance. Analysis of dark field images using bulk $\{200\}$ spots indicates the presence of voids in the material (e.g. Figure 3.5c), and the square nature of the (002) and (022) spots in figure 3.2 imply that the voids are tetrahedrally shaped. To understand this, consider that a tetrahedron in projection is a square and that the shape transform of a square is a star shape, with the points of the star half way along the square sides. If this intensity is smeared by the strain field of the voids, the resulting shape would be a square, diffuse spot which is what is seen in figure 3.2. The sharpness of the bulk forbidden (110) spots depends upon the concentration of voids and, in Figure 3.1 for instance, the bulk forbidden (110) spots are diffuse.

Superimposed on this bulk diffraction is far weaker surface diffraction from what initially appears to be two, but is in reality, four different domains; we will leave for later the exact analysis in terms of the four domains and just deal with two 90 degree rotation domains. Each of these domains corresponds to a hexagonal mesh corresponding to a single (111) monolayer contracted by about 4% with respect to the normal bulk (111) spacing. The contraction can be best seen by noticing that the two additional surface spots between the bulk (200) spots are not collinear, but lie slightly above a line connecting the bulk spots. We should also note that the diffraction pattern is consistent with monolayers; if there were more than one layer of (111) material stacked either as

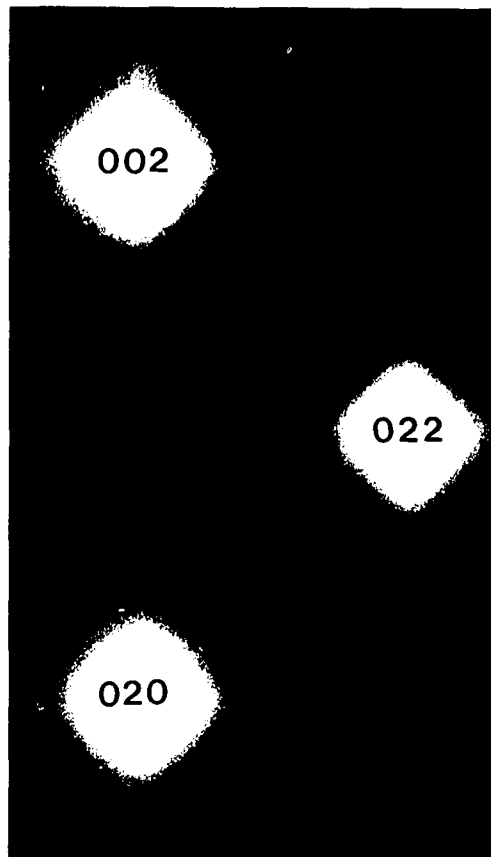


Figure 3.2. Shown are the higher index diffraction spots from the Au (001) reconstructed surface. The square shape of the spots correlates well with the presence of tetrahedrally shaped voids in the bulk crystal, which are remnant from the ion milling stage of surface preparation.

hcp or fcc the surface structure factor would be very different. Furthermore, the intensities of the surface spots are consistent with a single monolayer on the top and bottom surfaces. In addition there are also spots which can be attributed to some combination of double diffraction between the surface and bulk and, in principle, a modulation of the bulk material. The modulation that we are referring to would be the strain field associated with the surface reconstruction. In terms of a coincident site lattice between the bulk and surface, there is a strong coincidence along one bulk $\langle 110 \rangle$ direction of 5 and approximately a 20 coincidence normal to this; we will describe this as a $5 \times n$ structure and later refer to the '5' and 'n' directions for more detailed analysis.

The basic imaging technique that we have used is dark field imaging with an objective aperture around different diffraction spots. The objective aperture used was of a size that did not allow a single spot to be used so that typically, a bulk spot and two or three satellite spots were used in taking the dark field images. The most important dark field images were taken with the bulk $\{002\}$ type spots with the surface satellite spots shown in figure 3.1 included within the aperture. This gave images where the interference between the bulk and surface spots shows the local orientation of the '5' period of the domains, see Figure 3.3b. In other cases, two beam images using the systematic $\{200\}$ spots produces contrast from the 'n' dimension of the reconstructed domains, as will be discussed further below. Also, dark field images of the thin film specimen using the $\{110\}$ type spots showed contrast from both dimensions of the reconstructed unit cell.

Let us now return to the full breakdown of the diffraction pattern into four different domains. Closer analysis of the diffraction pattern indicates that the spots between a pair of bulk (200) spots are split into two, see Figure 3.3a. It is significant to note that the spot along the bulk $\langle 110 \rangle$ direction showed in general a far smaller (if any) splitting. Previous analyses of this surface have reported a rotation of the domains by about 0.5 degrees leading to a breakup into four domains. However, a rotation would lead to equal splitting of all diffraction spots and this is not the case. We can therefore conclude that the breakdown into four domains is due primarily to a shear normal to a bulk $\langle 110 \rangle$ direction, i.e. normal to the '5' direction. The presence of the four domains can be readily seen in {200} dark field images, for instance Figure 3.3b.

To summarize the general features of the reconstruction, there exists a surface hexagonal monolayer, contracted by about 4% relative to a bulk (111) Au layer, which approximately fits on the surface with a $5 \times n$ coincident site lattice.

§ 3.4.2 DOMAIN STRUCTURE

There is a vast amount of fine detail in both the images and diffraction patterns which indicates that the domain structure of the reconstruction is in fact exceedingly complicated. It should be mentioned that in other surfaces which have been looked at by our group, for instance the boron doped Si (111) $\sqrt{3} \times \sqrt{3}$ R30, such detail was missing so this is not an artifact of electron microscopy. The first point to mention is that there is a substantial amount of diffuse scattering along the '5' direction around the surface spots which depends upon the exact annealing treatment of the material. Figure 3.4 shows a

Figure 3.3. (a) An off the zone axis diffraction pattern showing the splitting of surface satellite spots around the $\{200\}$ diffraction spots, where the split spots are indicated with arrows. (b) A dark field image taken with the bulk $\{200\}$ type spot as well as the associated reconstruction satellite spots, which shows the presence of four domains. (c) A blow up of the $\{200\}$ type spot and associated reconstruction satellite spots showing the splitting in the reconstruction spots.

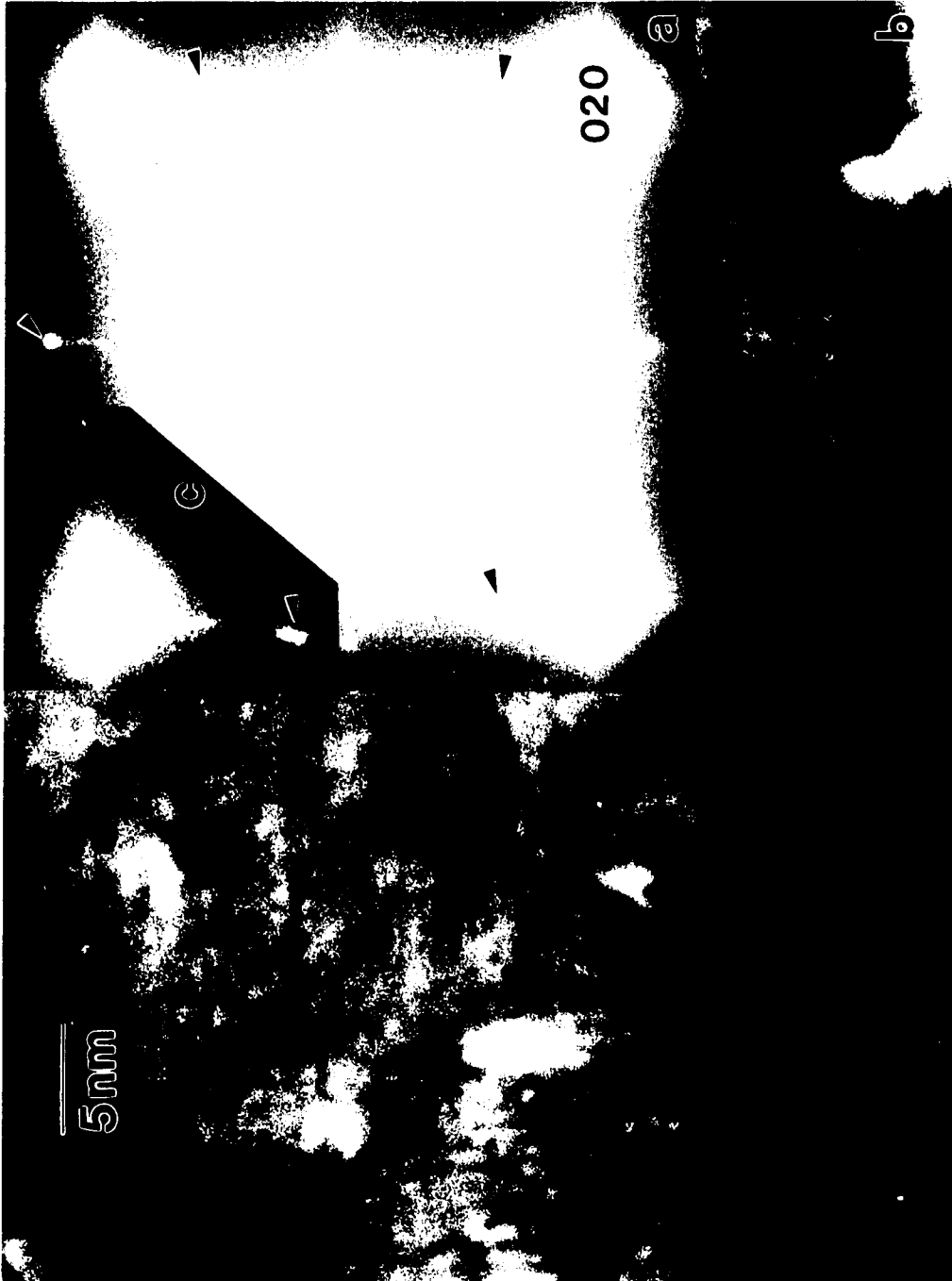
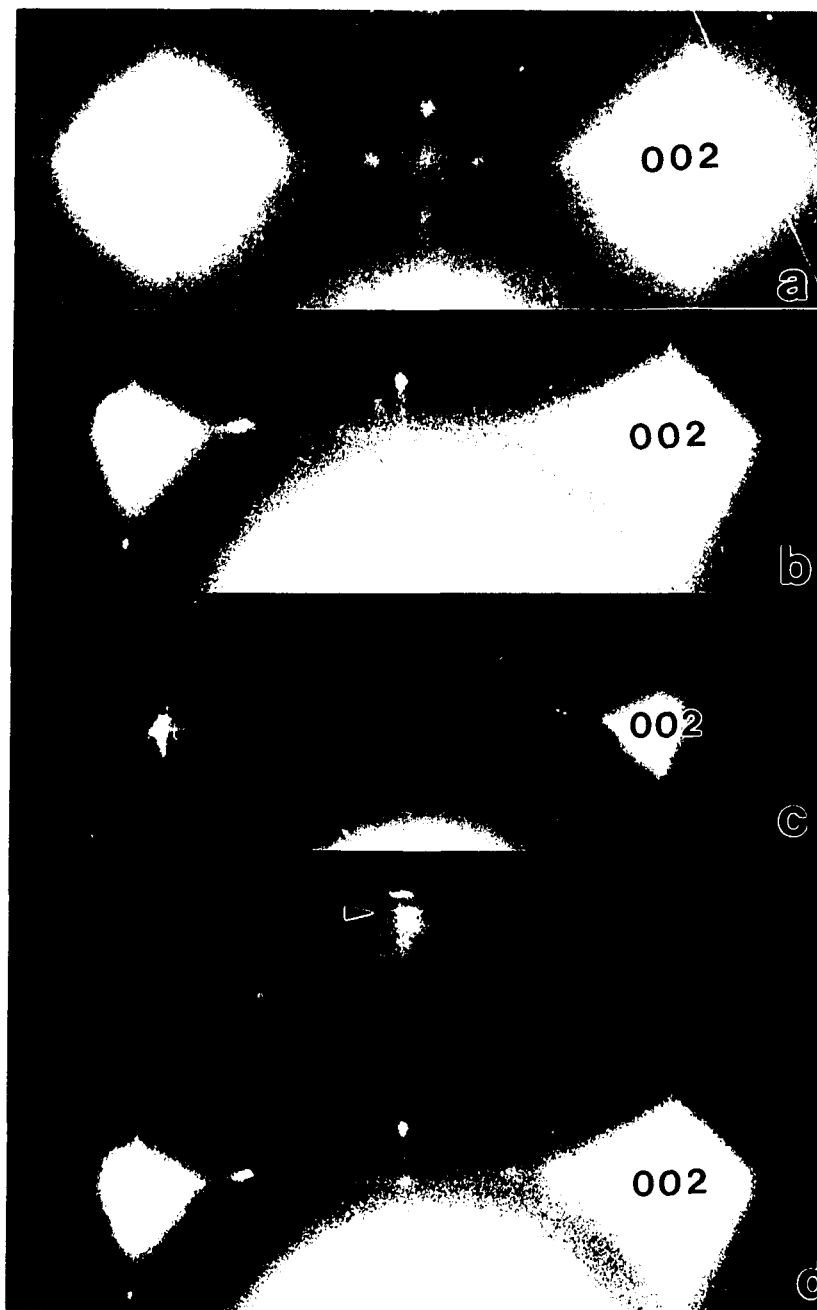


Figure 3.4. Shown here is a montage of diffraction patterns as a function of annealing time. (a) An on the zone axis diffraction pattern showing the $\{200\}$ spots and surface spots for the early stage of the reconstruction. It should be noted that the diffraction pattern is sensitive to the evolution of the reconstruction as is shown by the small difference between the background and surface spot intensities. (b) An off the zone axis diffraction pattern after more annealing. The diffuse intensity between the $\{200\}$ spots is decreased and the intensity of the surface spots is increasing. The satellite spots near the $\{200\}$ bulk spots are beginning to split. (c) An off the zone axis diffraction pattern exhibiting a marked decrease in diffuse scattering near the $\{200\}$ type spots. The surface spots are now clearly split and the intensity of the surface spots is increasing indicating an ordering of the reconstruction. (d) A larger view of the diffraction pattern shown in (b), which shows the splitting of a bulk $\{220\}$ type reflection (arrowed).



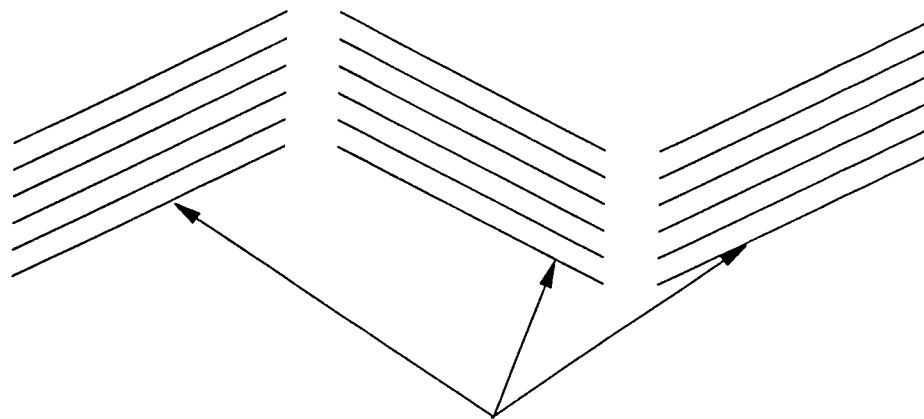
montage of diffraction patterns concentrating on this region as a function of improving annealing of the material. To assist in interpretation of this diffuse scattering, Figure 3.5 shows a comparable montage of $\{200\}$ images. In the earlier micrographs in Figure 3.4 and 5 the domain size along the '5' direction is small but quite large along the 'n' direction. In particular, a common occurrence is an intimate intergrowth of pairs of sheared domains, see Figure 3.5a. This may be just a microdomain structure, or it may in fact be a stable modification of the material by a constant shear wave (see Figure 3.6).

As the annealing of the material improves, the bulk $\{110\}$ spots become sharper, consistent with both the removal of bulk defects and a higher degree of flatness in the surface. There is however, no noticeable difference in the overall film uniformity as the annealing improves, so we are led to believe that the major difference is the reduction in the number of bulk defects and associated strain field. The only change in the surface structure is growth in the size of the reconstructed domains and a reduction in the amount of diffuse scattering, see for instance Figure 3.4c and 3.5c. As the annealing improves the splitting of the spots in each pair of domains becomes more apparent and can be seen more clearly further out in the diffraction pattern, see for instance Figure 3.4d.

In addition to these changes to the domain structure, there are substantial variations in the 'n' coincidence. In the less well annealed samples, this was quite difficult to observe and only with longer annealing did it become more apparent. With the latter samples it was quite clear that the 'n' coincidence was not a fixed number but, in fact, varied from domain to domain and even within domains. For instance, Figure 3.7 shows a region where a number of domains are visible with slightly different orientations,

Figure 3.5. Shown here is a montage of dark field images taken with bulk reflections and the associated surface satellite spots. (a) A $\{200\}$ dark field image showing the intimate intergrowth of pairs of sheared domains. This modulation may be due to a shear wave along the longer dimension of the reconstructed surface cell. (b) A $\{200\}$ dark field image showing clear domain structure as well as the presence of voids which are remnant from the ion milling process. These voids are responsible for the diffuse scattering seen in diffraction patterns like those shown in figure 3.4. (c) A $\{110\}$ dark field image of the Au thin film sample after annealing, which shows several domains of different sizes and shapes.





'5' Fringes of The (5x1) Reconstruction

Figure 3.6. A schematic diagram of a possible shear structure which is seen in figure 3.5a.

and in some cases, small changes in the apparent periodicity at the edge of the domain are evident. It is very dangerous to directly interpret these spacings since local strains can couple into the apparent spacing observed, but they do indicate local variations. We should also note that the domains do not appear to cross the line where a dislocation (arrowed) is passing within the bulk. A clearer demonstration of the local variations is shown in the high resolution images shown in Figure 3.8, where both the '5' and the 'n' dimension can be resolved. Whereas the '5' dimension does not vary, it is clear that the 'n' dimension of the structure is very different.

§ 3.5 DISCUSSION

All the above information appears to be very complicated, but in fact can be understood relatively easily; in the process of analyzing the results from this surface, it becomes apparent why there has been so much discussion in the literature of the fine details of the reconstruction, but agreement about the basic elements. First, it should be stated that the average structure of the reconstruction is a 5x20 cell; this agrees with the previous work and does not appear to change substantially. Our only disagreement is that the material is sheared, not rotated; however, since this conclusion concerning rotation came from small plate like crystallite samples¹⁰, surface effects maybe responsible for the differences seen here.

A significant feature of the reconstruction is that the '5' coincidence is strong and does not appear to substantially change. Looking at the coincidence between the surface and bulk as sketched in Figure 3.9, it is apparent that there are regions of excellent

Figure 3.7. A systematic two beam dark field image taken with the bulk {200} type spot and associated surface satellite spots, showing the existence of several domains. These domains are marked A through E and are oriented along several directions. Closer examination reveals that these domains are clearly confined by the presence of dislocation lines near the surface, which are arrowed.



Figure 3.8. A high resolution image showing both the "5" and "n" dimension of the reconstructed surface. The "5" dimension is seen to be a hard dimension while the "n" dimension is seen to have a wavy character. There is a noticeable switch in orientation of the reconstructed domains marked by a and b, as a function of distance along the peninsula shown in the image.



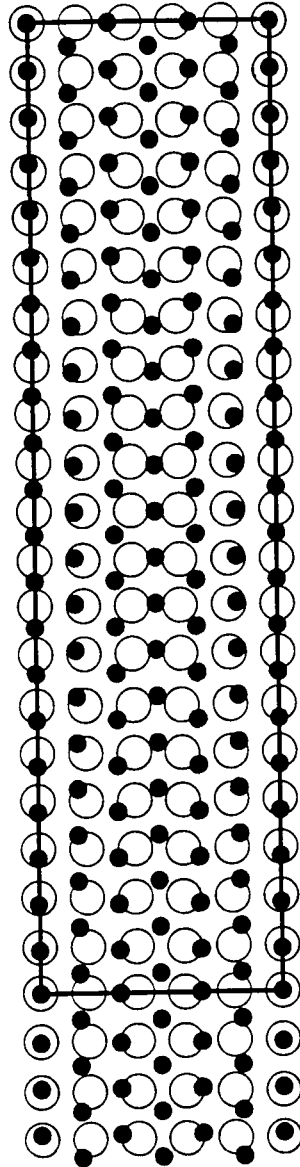


Figure 3.9. A coincidence site lattice construction of the (5x1) reconstructed surface. Coincidence for the "5" dimension is very strong and should tend to lock the surface layer along this dimension. This dimension is then referred to as a hard dimension, while the "1" dimension exhibits no similar locking tendency. It is possible, with the appropriate strain along the bulk $\langle 110 \rangle$ direction, to make the 1 dimension range from 15 to 21.

matching along the '5' direction which will tend to lock the surface layer with respect to the bulk. If the surface is sheared normal to this layer, there will be relatively little change in the total energy. We find it useful to think of the '5' direction as a hard direction, and the 'n' direction as soft.

The variations in the 'n' dimension can be understood as local accommodations to strains. STM⁹ and ion channeling data¹¹ indicate the presence of a substantial buckle along the '5' direction which would lead to a significant bulk strain field. In a large domain the center will approach one value of the 'n' component, but at the edges or when the substrate geometry changes, the strain field will change which explains the local variations shown in Figures 3.7 and 3.8. This is also consistent with the fact that the domains do not appear to cross the strongly strained region near to dislocations.

To summarize the above, the nature of the reconstruction on the Au (001) surface is a hexagonal monolayer which is easily locked in along the '5' direction. The exact nature of the 'n' component depends heavily upon the local geometry and local strain. The data is consistent with a shear of about 1 % along the '5' direction leading to a cell with the following form,

$$\begin{bmatrix} 5 & 0 \\ \delta n & n \end{bmatrix} \quad (3.1)$$

as the 'best' coincident site lattice, where $15 \leq n \leq 21$ and $\delta = 0.01$. We cannot however completely rule out a small rotation in addition to the shear seen above. Variations in the experimental results reported by different groups can be rationalized as variations in the

exact nature of the surface, since they were not able to determine directly the defect structure beneath the surface (e.g. dislocations, point defects).

In summary, clean Au (001) surfaces were prepared under UHV conditions and the surface reconstruction was followed using transmission electron diffraction and conventional TEM imaging methods. The clean surface reconstruction of a Au (001) surface was found to reconstruct into nearly orthogonal ($5 \times n$) domains, where n is between 15 and 21. These domains are sheared by 0.5 degrees along the '5' directions of the reconstruction. There is good evidence that the exact nature of the reconstruction is a function of the local substrate geometry and defect locations.

CHAPTER 4

THE EFFECT OF BULK DEFECTS ON SURFACE RECONSTRUCTIONS

§ 4.1 INTRODUCTION

During the course of our work on the bulk single crystal Au (001) reconstructed surface, it became apparent that bulk defects such as stacking faults and dislocations were interacting with the (5x n) reconstruction in a non-trivial fashion. In many dark field images the reconstruction could be seen to conform to the strain field of bulk defects and in some cases was completely disrupted in areas directly over the defect strain field. It was not until after we were done with the Au (001) single crystal sample and had moved onto a Si (111) surface, that we began to notice this interaction in both the Au (001) (5x n) and Si (111) (7x7) dark field images. We subsequently repeated the Au (001) reconstruction results, but this time with a thin film sample from Argonne National Lab. During this experiment, we were not only looking for the differences in the character of the reconstruction, but specifically for the interaction of the (5x n) reconstruction with bulk defects.

§ 4.2 BACKGROUND

As was mentioned in chapters 1 and 3, surface reconstructions of clean metal surfaces have been studied in the past with a large degree of success using spatially

averaged techniques, such as low energy electron diffraction (LEED), reflective high energy electron diffraction, and He ion scattering. These techniques have been successful in determining the dimensions and symmetry of reconstructed surfaces, but because they are spatially averaged, they do not allow direct observation of reconstructed domain morphology in real space. With the advent of STM (scanning tunneling microscopy), it has been possible to directly image reconstructed domains in real space, but STM has one inherent limitation; it is in many ways too surface sensitive. For instance, one way of describing the Si (111) (7x7) reconstruction is as an hexagonal array of subsurface partial dislocations coupled with atomic rearrangements in the very top layer¹. STM is sensitive to atomic rearrangements, but is unable to determine the nature of the underlying dislocations except in cases where defects occur just below the reconstructed layer. An important issue that has thus far remained unclear is whether subsurface defects might be playing an important role in reconstructed domain structure and in the surface reconstruction process in general. Transmission electron microscopy under ultra-high vacuum conditions affords the possibility of simultaneous observation of both the bulk and surface, thereby enabling the observation of reconstructed domain and bulk defect interactions. As was mentioned in chapter 2, it has not been possible until very recently to combine high quality electron microscopy with standard surface science techniques due to the stringent cleanliness and vacuum requirements of conventional surface science studies. The intention of this chapter is to demonstrate that subsurface dislocations and stacking faults can strongly interact with the reconstructed domains of clean metal surfaces.

Examples are shown from a Au thin film sample which clearly show the interaction of the strain field of subsurface defects with the Au (001) (5x n) reconstruction.

§ 4.3 EXPERIMENTAL

The experimental details of the microscopy and surface preparation have already been explained in chapter 2. The only real difference between the process outlined there and that used in this experiment is that no initial sample preparation was required. Since this sample was a thin film, the only specimen preparation that was necessary was to clean the surface in the SSC and anneal it to obtain the reconstructed surface. Annealing was done using the Kimball Physics electron gun with 3-4 keV electrons and a current of 2-3 mA.

§ 4.4 RESULTS

In the following, we will focus on results demonstrating the interaction of dislocations and stacking faults with the Au (001) (5x n) reconstructed surface. The details of the reconstruction were discussed in chapter 3.

There are several conventional TEM techniques that are available to examine reconstructed surfaces. As was mentioned in chapter 2, weak beam techniques have, in the past, been used in an effort to maximize contrast from surface features. In chapter 3, it was found that conventional plan view bright and dark field images provide more than adequate contrast from reconstructed surfaces. Both on and off the zone configurations can be used to determine the size and morphology of reconstructed

domains. While it is true that conventional plan view bright and dark field imaging provides more than adequate contrast from surface features, one should be cautious in analyzing these images. The reason for this is that scattering from surface features can couple with scattering from bulk defects producing anomalous contrast features; it is therefore imperative that images with more than one diffracting condition be used. For instance, it is possible under certain conditions to see fringes from the reconstructed surface seemingly end at a dislocation line. However, under another diffracting condition the fringes can be seen to pass over the dislocation line unaffected.

The reconstruction of the Au (001) surface forms a variety of domain sizes and morphologies depending upon many factors including the defect state of the bulk crystal. In areas where no noticeable dislocation and stacking fault concentrations exist, large domains of varied shape exist. Figure 4.1 is a dark field image of a Au (001) reconstructed (5x n) surface from a thin film sample taken with the surface allowed {110} diffraction spot and the associated reconstruction spots. The fringes marked with arrows and the letter 'n' are the long dimension of the reconstructed cell, and roughly orthogonal to these are smaller fringes from the '5' dimension. Heavier dark lines marked D indicate domain boundaries. There are also voids remnant from the ion milling process which appear as white spots. This figure is an example of domain morphology which is unaffected by bulk defects.

Figures 4.2a and 4.2b are dark field images taken with the bulk { 220 } type reflections and the associated surface satellite spots. In both images, a dislocation line can be seen to wind through the images in an elbow shape. Closer examination reveals



Figure 4.1. Shown is dark field image taken with the surface allowed (110) reflection and the associated reconstruction spots. Fringes marked by arrows and the letter 'n' correspond to the long dimension of the reconstructed unit cell and roughly orthogonal to these are fine fringes corresponding to the '5' dimension. The larger dark lines marked by 'D' are domain boundaries. This is an example where the reconstructed surface is not affected by subsurface bulk defects.

Moire fringes from the 'n' dimension of the reconstructed unit cell. These fringes can be seen to terminate at the dislocation line in figure 4.2a. Figure 4.2b was taken under a slightly different diffracting condition under which the dislocation line is less visible. The Moire fringes from the 'n' dimension of the reconstructed unit cell however have a larger intensity ratio relative to the bulk crystal and are therefore more visible. It is clear from this micrograph that the reconstruction is disrupted by the dislocation line.

Figures 4.3a and 4.3b are dark field images taken with the surface $\{110\}$ type reflection and the associated surface satellite spots. A stacking fault can be clearly seen in the center of the micrograph and closer examination reveals Moire fringes from the 'n' dimension of the reconstructed unit cell. These fringes are seen to be clearly disrupted by the stacking fault. Figure 4.3b is a dark field image taken from the same area, but under a condition that maximizes the ratio of surface contrast to that of the bulk, thus making the stacking fault less visible. The Moire fringes of the 'n' dimension are more clearly visible and are seen to be disrupted by the stacking fault. Also visible in this micrograph are a finer set of Moire fringes roughly normal to the Moire fringes from the 'n' dimension. These finer fringes are from the '5' dimension of the reconstructed unit cell.

The examples shown clearly indicate interactions between sub-surface defects and the Au (5x1) surface reconstruction. This is not really a very surprising result, but definitely opens up as an issue for discussion, the role of bulk defects in explaining disagreements in results from different surface structure determinations. Dislocations near a free surface interact strongly with their corresponding image dislocations leading to a

Figure 4.2. (a) A dark field image from a (5x n) reconstructed Au (001) single crystal thin film taken with the bulk (220) reflection and the associated reconstruction spots. Central in this micrograph is a dislocation line which is arrowed. Upon closer examination, lighter Moire fringes from the 'n' dimension of the reconstructed unit cell can be seen to approach the dislocation line but not cross it. (b) A dark field image taken under slightly different diffracting conditions which enhance the contrast from the surface relative to the bulk making the Moire fringes from the reconstruction more visible and the dislocation line less visible. Again, the Moire fringes from the 'n' dimension of the reconstructed unit cell can be seen to approach the dislocation line but not cross it.

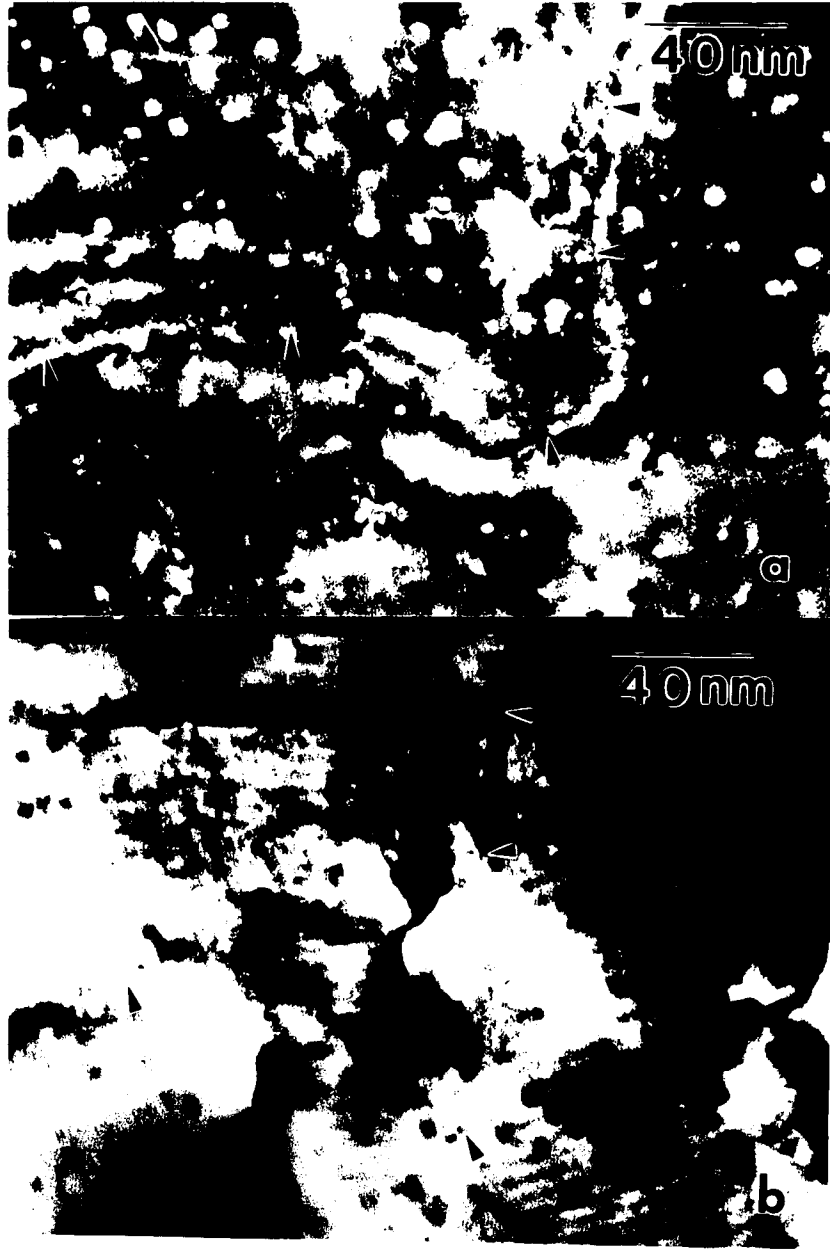
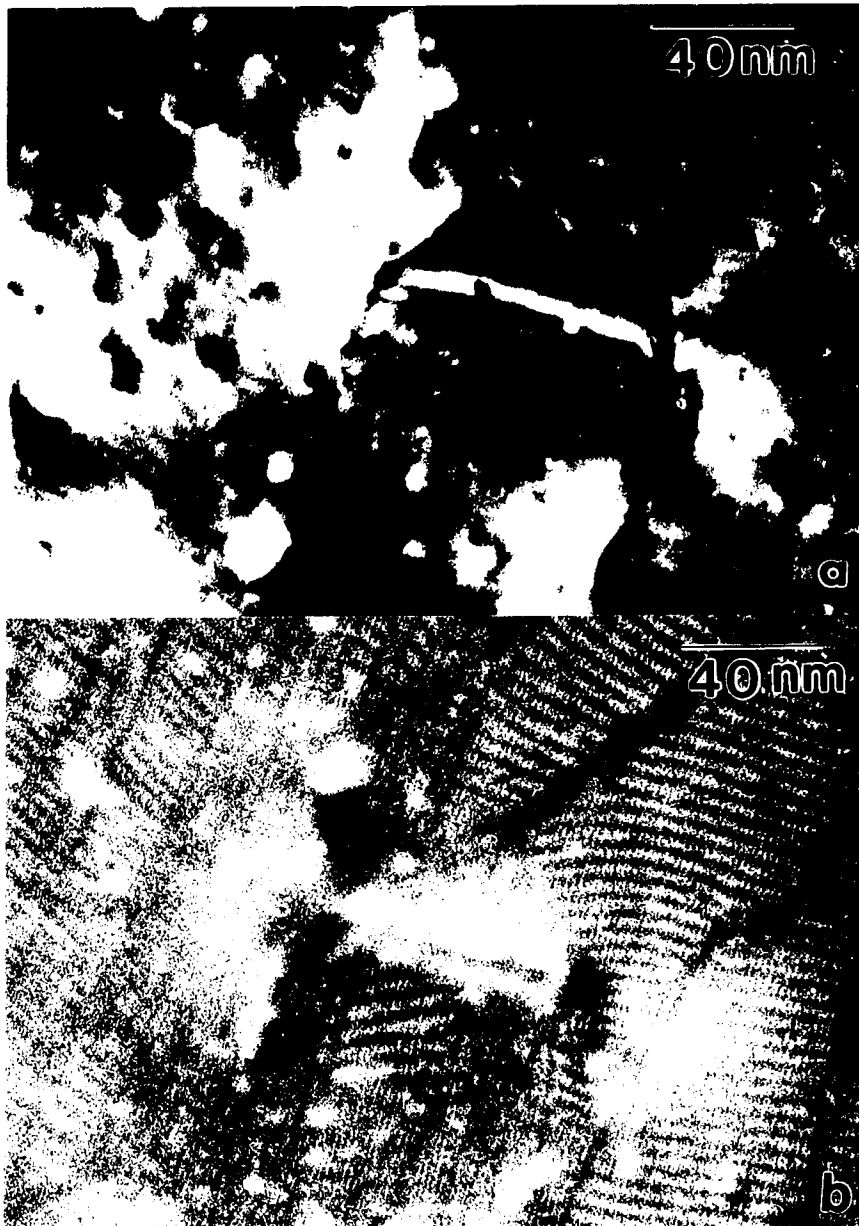


Figure 4.3. (a) A dark field image from a (5x n) reconstructed Au (001) single crystal thin film taken with the bulk forbidden (110) reflection and the associated reconstruction spots. Central in this micrograph is a stacking fault and closer examination reveals Moire fringes from the 'n' dimension of the reconstructed unit cell. These Moire fringes can be seen to terminate at the stacking fault. (b) A dark field image of the same area as 4 (a) but under slightly different diffracting conditions which make the fringes from the reconstruction more visible and contrast from the stacking fault less visible. Moire fringes from the '5' dimension of the reconstructed unit cell can also be seen to run roughly normal to the 'n' dimension Moire fringes. Both sets of fringes are seen to terminate at the stacking fault.



substantial strain field at the surface which can readily interact with the reconstruction. The details of the elasticity necessary to model this case are given in Chapter 6. If we use the analysis described there and apply Hooke's law, the expression for the inplane strain of an edge dislocation, a distance of c below the reconstructed surface is given by the following equation².

$$\epsilon = -\frac{2bc}{\pi} \frac{y^2}{(c^2 + y^2)^2} \quad (4.1)$$

In equation (4.1), b is the Burgers vector, and y is the distance away from the dislocation, along the surface. If the dislocation is a distance of 25 angstroms below the surface the in plane strain exceeds 1 %. If we now consider that the 'n' dimension of the Au (001) (5xn) reconstruction is the commensuration distance between a bulk <220> direction and an equivalent <220> direction of the (111) - like surface monolayer, the strain field of a sub-surface dislocation will alter substantially the energetics of this matching as well as the spacing.

The Au (001) (5xn) reconstruction is not the only reconstruction which has been found to exhibit an interaction with bulk defects. The Si (7x7) surface reconstruction has been observed to interact with {112} type stacking faults³. These stacking faults act to constrain the size of reconstructed domains as well as acting as domain boundaries.

CHAPTER 5

UHV MICROSCOPY OF THE RECONSTRUCTED Ir (001) SURFACE

§ 5.1 INTRODUCTION

The Ir (001) surface represents the first true bench mark for the Hitachi UHV H9000 as a versatile UHV instrument capable of studying contamination sensitive clean surfaces. While it is true that work with Au and Si crystals has become routine for the UHV-H9000, these are very forgiving surfaces. The sticking coefficients of residual vacuum gases such as CO, CO₂ and O₂ are relatively small on the Au (001) surface and Si (111) surface but for Ir, the sticking coefficient for CO is very close to 1 at room temperature. As such, Ir provides an excellent test case for the integrity of the UHV environment in both the surface science chamber (SSC) and microscope.

Ir (001) also provides a convenient test for many of the techniques used in the work on the Au (001) surface. The Ir (5x1) reconstruction is believed to have a much stronger coincidence with the (1x1) surface and can, in a sense, be thought of as locked into the bulk fcc surface. The reconstructed unit cell is considerably smaller than the Au (001) (5xn) structure and has provided an excellent test of the dark field imaging techniques used there. Also, the observation of the reconstruction in the presence of bulk defects will add to the existent knowledge obtained from the Au (001) surface. It should be

expected that since the reconstructed unit cell has a stronger coincidence with the bulk (1x1) surface, the interaction of bulk defects with the reconstruction should be considerably reduced, if at all existent.

§ 5.2 BACKGROUND

The Ir (001) surface has long been known to reconstruct into a (5x1) surface unit cell. The majority of the work done on this surface has been done using low energy electron diffraction (LEED)¹⁻¹¹ and more recently, field ion microscopy (FIM)¹²⁻¹⁴.

In general it has been found that the (001) faces of Au¹⁵, Pt¹⁶ and Ir¹⁻¹⁴ reconstruct in a similar way. In all cases, the reconstructed layer consists of a hexagonal reconstructed layer superimposed on the bulk fcc (100) surface. For Au and Pt, the misfit between the reconstructed layer and the bulk surface is taken up by some combination of a surface layer compression and a shear or rotation of the hexagonal surface mesh. On both the Au and Pt (001) surfaces, this produces rather large reconstructed unit cells with a strong coincidence in one direction and a softer coincidence in the other. The Ir (001) (5x1) reconstruction is an exception in that the reconstructed hexagonal layer seems to have a much stronger coincident relationship with the fcc quadratic surface. It is generally found that the hexagonal overlayer in the (5x1) reconstruction requires no rotation or shear to fit on the (1x1) surface.

The general features of the Ir (001) (5x1) reconstruction are as follows. As was mentioned previously, the reconstruction is made up of a quasihexagonal surface layer superimposed on the bulk fcc quadratic lattice forming a (5x1) coincidence with the bulk surface. The reconstructed layer is referred to as quasihexagonal because it is believed

that the hexagonal angle is not exactly 60° but is slightly less. The (5x1) surface unit cell consists of 6 atoms and is shown in figure 5.1. In order to accommodate the higher density of atoms in the surface unit cell, the quasihexagonal layer is buckled by roughly 0.5 \AA upward¹. The most widely accepted model is referred to as the "two bridge model" and assumes that the registry of the quasihexagonal surface layer is one in which two bridge sites of the bulk fcc surface are occupied by the reconstructed layer. In the two bridge model, the quasihexagonal reconstructed layer is found to have a 5% bond length contraction in order to form the (5x1) coincident cell². While it is true that the "two bridge model" is the most widely agreed upon model of the Ir (001) (5x1) reconstruction, it is by no means certain that it is correct. R factor analyses done by Lang et al². indicate that the two bridge model has the best Zanazzi-Jona (ZJ) R factor fit of 0.2². This ZJ R factor is at the upper limit of what is considered a good fit. ZJ R factors with a value of less than 0.2 are considered "good", while those between 0.2 and 0.35 are considered "fair", and those with a value of 0.5 or greater are considered "bad"⁴.

The (5x1) reconstructed surface is generally considered to be the clean surface structure of the Ir (001) surface. The (1x1) surface is thought to be a metastable state which is far from equilibrium³. It has been suggested that the (1x1) Ir surface is stabilized by the presence of chemisorbed O_2 ³. The (1x1) surface will reconstruct to the (5x1) surface after heating to temperatures higher than 800° K ⁴, which is the most widely published transition temperature. This temperature criterion is, however, deceiving. If one considers the ways in which most investigators obtain the reconstruction, it is clear that no such simple criterion can be determined. In fact, the methods of obtaining the

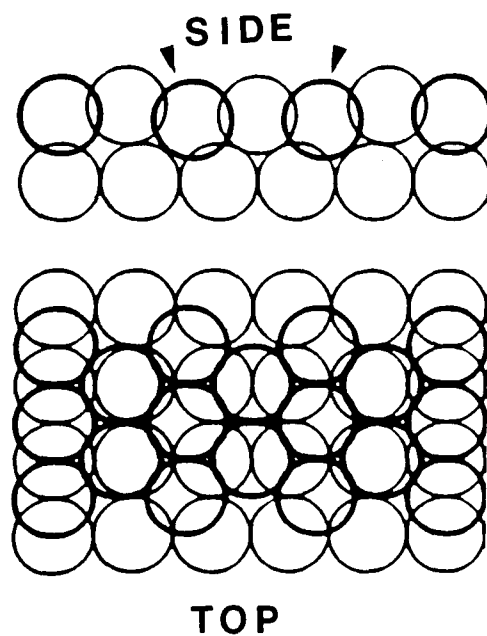


Figure 5.1. A schematic drawing of the Ir (001) (5x1) reconstructed surface showing the two bridge model. The heavy circles arrowed in the side view are the atoms occupying the bridge sites. (Taken from Van Hove et al.⁴)

reconstruction are somewhat varied. For instance, several authors have used a combination of repeated annealing in partial pressures of O_2 at temperatures of approximately 1400 °K to clean the surface, followed by annealing at the same temperature for a few minutes^{5,6}. In some cases, the same O_2 treatments are used followed by ion bombardment and then high temperature annealing^{3,7}. Usually after several cycles of these treatments, the clean surface (5x1) reconstruction is observed. The reason why the high temperature annealing is done in a partial pressure of O_2 is to remove CO that is chemisorbed on the surface by forming CO_2 . Grant⁸ has obtained the (5x1) reconstructed surface by prolonged heating at 1400 ° C, followed by ion bombardment with Ar and finally, annealing at 400 °C . In the case of FIM investigations, the Ir tip is cleaned by a combination of heating or field evaporation¹². In some cases, the tip can be sputter cleaned and then heated¹³⁻¹⁴.

The method of surface preparation used varies from investigation to investigation and more than likely depends upon the individual UHV chamber and the equipment available. The investigators who chose to use the O_2 surface cleaning treatment followed by high temperature annealing are probably concerned with the residual gases of CO, CO_2 and H_2O in vacuum. In the case of the investigation by Grant⁸, the fact that the (5x1) was observed after annealing the (1x1) surface at 400 °C indicates that the transition to the (5x1) is aided by surface disorder caused by ion bombardment. It is perhaps more appropriate to say that the reconstruction of the Ir (001) surface is a function of temperature, vacuum environment, surface disorder and time. In cases where the surface is prepared without ion bombardment, the (1x1) to (5x1) transition will take place at

temperatures above 800 °K. If, however, the surface has been disordered by ion bombardment, the transition temperature can be significantly lowered. It should also be pointed out that Lehwald et al.⁷ have found by a lattice dynamical analysis that there exists a large tensile surface stress for the Ir (001) surface. This tensile stress is suggested to be the driving force for the (1x1) to the (5x1) transition.

The adsorption of CO, CO₂ and O₂ on both the Ir (001) (1x1) and (5x1) surfaces have been widely studied^{1,3,5,8}. Several authors have found that the (5x1) surface can be saturated with both CO and CO₂ without destroying the reconstruction. If however O₂ is allowed to saturate the surface, the (5x1) reconstruction will revert to the (1x1) surface. The adsorption of CO and CO₂ was found by Grant⁸ to produce spots at the {1/2, 1/2} positions with weaker satellite spots at the {0,±1/2} positions. In the case of O₂, if the O₂ saturated (5x1) reconstructed surface is heated, the (5x1) surface is seen to disorder and ultimately form oxygen (2x1)^{1,3,5,8}, (14x2)⁸, (7x2)⁸ and (1x1)⁸ superstructures.

It is the intention of this chapter to present the first UHV-TEM results on a bulk single crystal Ir (001) reconstructed surface. Further results on the interaction of bulk defects with the reconstruction will be presented and contrasted with the case of the Au (001) (5xn) reconstruction.

§ 5.3 EXPERIMENTAL PROCEDURES

The initial sample preparation scheme used outside the SSC was exactly the same as that described in chapter 2. It should be pointed out that mechanical polishing techniques work considerably better on Ir than Au, due to the fact that Ir is much harder

and easier to polish than Au. The real difference came in the surface cleaning. Because the Ir (001) surface has a sticking coefficient near 1 for CO and fairly high for CO₂, it is very difficult to clean. As a result the standard sputter anneal cycle described in chapter 2 was modified slightly. Instead of ion milling and annealing in separate steps, both were done at the same time. The idea was to anneal out bulk crystal damage and clean the surface at the same time. The elevated temperature of the crystal surface coupled with ion bombardment with Xe⁺ ions should keep desorbed gaseous species from readsorbing onto the clean surface. The results of this modification were that the surface could be cleaned more completely and in less time. In most cases, 4.1 keV Xe⁺ ions were used to ion mill the surface and the Kimball Physics electron gun was used to heat the specimen. The specimen temperature was at first monitored by an infrared pyrometer with an emissivity set at 0.19. It was not possible to accurately correct for the difference in emissivity between 0.19 and 0.35 for Ir. The temperature was therefore monitored by comparing the color of the heated sample with the equivalent color of a black body for a given temperature. For higher temperatures, this is not a bad approximation, but it is not accurate in the low temperature regime. The concern was not so much the exact temperature, but that the surface was hot enough to prevent the adsorption of residual vacuum gases and also to be above the (1x1) to (5x1) transition temperature.

The most important stumbling block to obtaining the clean (5x1) surface is undoubtedly the residual gases in the SSC. As was pointed out in chapter 2, it is not the residual gas spectrum at the base pressure that is important, but the partial pressures of hydrocarbons and CO_x vacuum constituents when the ion and electron guns are operating.

During the ion milling or annealing steps of surface preparation, these partial pressures need to be below about 6×10^{-9} torr, otherwise the surface cannot be cleaned properly. It is therefore necessary that the residual gas pressures in the SSC be as low as possible, especially for CO. In an effort to meet this requirement, an O₂ plasma clean was tried to reduce the hydrocarbon background. The plasma clean was successful and reduced the hydrocarbon background in the chamber considerably. In fact, the chamber itself was observed to be visibly cleaner. After subsequent baking of the SSC and outgassing of the proper equipment, the (5x1) reconstruction was obtained. The reconstructed surface could be obtained reproducibly by outgassing the necessary equipment and then doing a combined ion mill and anneal cycle.

§ 5.4 RESULTS

The UHV-TEM results from the Ir (001) surface will be presented in two major sections. In the first section the evolution of the microstructure of the Ir (001) sample up until the time that the reconstruction was found will be presented. In the second section the results from the reconstructed surface will be discussed.

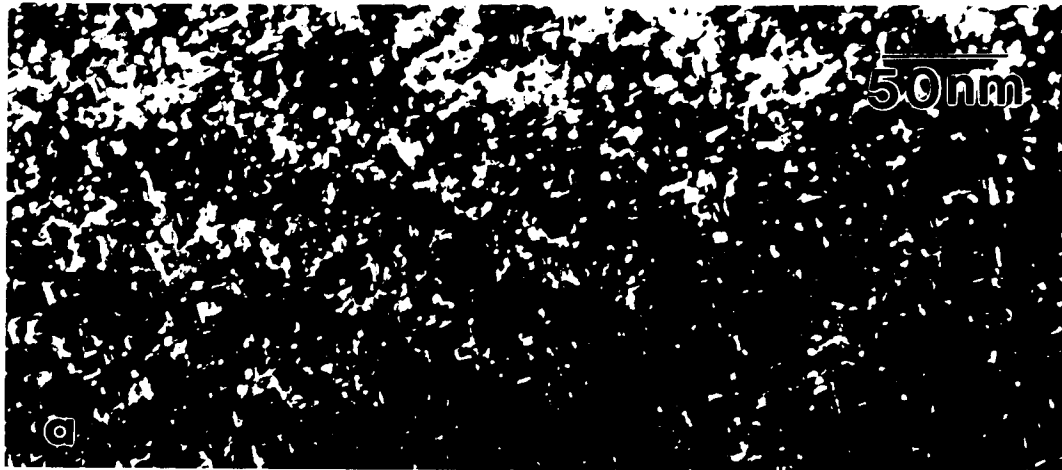
§ 5.4.1 INITIAL MICROSTRUCTURE

After the mechanical polishing and ion milling steps of specimen preparation were completed, the Ir crystal was put into the SSC and the chamber baked. After the bake, the crystal was put into the microscope for initial examination. The initial microstructure was one indicative of a mechanically damaged specimen. Figure 5.2a is a dark field

image taken with the objective aperture around a $\{200\}$ type spot. This image shows a high concentration of defects many of which are probably microtwins and small dislocation loops due to the ion milling preparation outside the microscope. The high concentration of defects is not cause for concern at this stage because these defects can be annealed out. Figure 5.2b is a bright field image taken after a couple of independent ion milling and annealing steps. The image shown in figure 5.2b was taken right after an ion milling step with 3.1 keV Xe⁺ ions but before annealing. There is a clearly visible defect layer near the surface and the bulk crystal can still be seen to have a high defect density. After further annealing, much of the damage remnant from the earlier stages of specimen preparation can be removed. Figure 5.2c is a dark field image taken with a $\{200\}$ type spot which clearly shows an improved defect state of the crystal. The salt and pepper contrast seen in figure 5.2a is gone but there are still some dislocations present. Another feature that appeared soon after the defect density of the crystal was reduced is the small particles that can be seen throughout figure 5.2c. The exact nature of these particles will be discussed later in this chapter.

The annealing properties of Ir are considerably better than that of Au. It was possible in the first few ion mill and anneal cycles to get the crystal to begin to order. The most visible sign of this was the squaring of holes in the crystal. Figure 5.3 is a low magnification bright field image of the edge of the crystal with a squared hole. The edges of the hole are quite sharp and the corners of the square are not rounded but are truncated by a diagonal plane. A small amount of amorphous carbon contamination (arrowed) can be seen on the peninsula jutting up toward the top of the figure.

Figure 5.2. A montage of dark field images as a function of surface processing time. (a) A dark field $\{200\}$ image showing the initial crystal. The defects seen in this image are microtwins and small dislocation loops. (b) A bright field image after further processing steps but before an annealing step. A defect layer at the surface can be seen which is due to ion beam damage. (c) A $\{200\}$ dark field image after further annealing. The defect concentration is reduced but the particles remain.



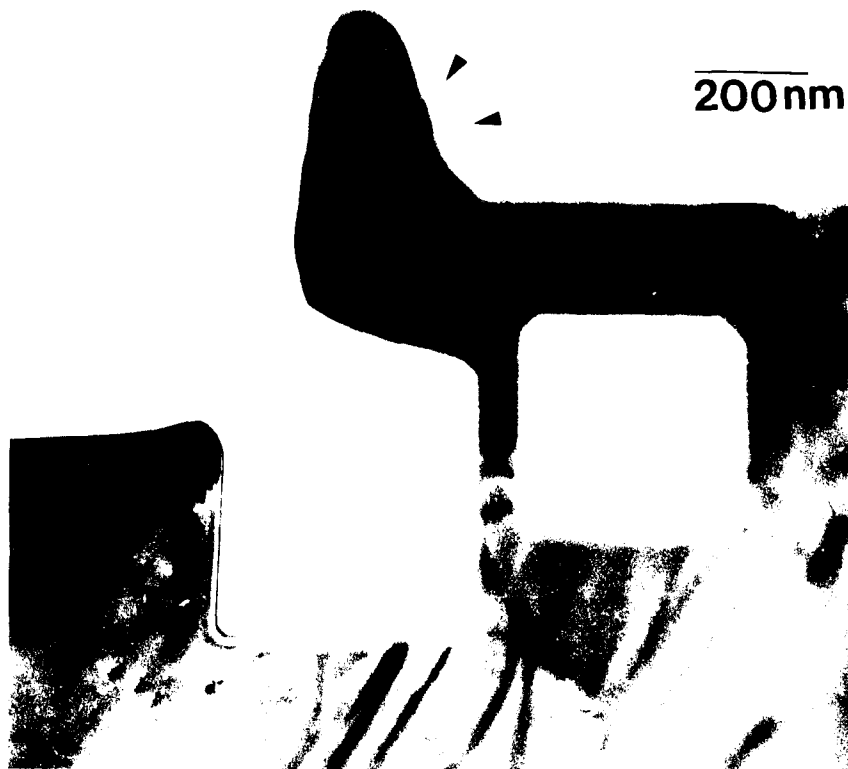


Figure 5.3. Shown is a bright field image showing a square hole that appeared after annealing. Arrowed is carbonaceous contamination that could not be eliminated by sequential ion milling and annealing treatments. Combined treatments of ion milling and annealing were successful in eliminating this type of contamination.

The kind of carbonaceous contamination seen in figure 5.3 was difficult to get rid of by using independent ion milling and annealing steps. It was after several more surface cleaning cycles that a combined ion milling annealing treatment was tried. The combined treatments were remarkably successful at cleaning the surface as well as keeping the defect density of the material to a minimum. The concentration of particles seen in figure 5.2c did not reduce as a function of annealing.

Parallel electron energy loss spectroscopy (PEELS) analysis was done on the specimen to see what, if any contaminants were present in the crystal as well as to try to get an idea of what the small particles in the crystal were. PEELS spectra were taken in differential mode at various points in the surface preparation. The major features in these spectra were from carbonaceous contamination, oxygen, argon and iridium. The edge due to Ar was from ions implanted during the initial thinning of the specimen outside of the SSC. The carbon and oxygen edges could be due to surface contamination or to iridium oxide formation during annealing. With subsequent annealing steps, the edge due to argon was reduced below the limit of detection of the PEELS spectrometer.

§ 5.4.2 APPEARANCE OF STEPS

After several combined ion milling and annealing cycles, where the annealing temperature was above 1000 °C, steps were found on the surface. Images of steps for [001] zone axis are often taken in centered dark field using the bulk forbidden surface allowed, {1x1} type spots. It is instructive to examine how these spots arise. Consider an electron beam illuminating a crystal down the [001] zone axis, viewed down the $\langle 110 \rangle$

direction as shown in figure 5.4. Let the Ewald sphere intersect the (220) diffraction spot. The amplitude in reciprocal space of the {111} type spots is given by a Sinc function, where t is the thickness and s is the excitations error.

$$\phi = \frac{\text{Sin}(\pi ts)}{\pi ts} \exp(\pi its) \quad (5.1)$$

As can be seen in figure 5.4, small changes in the thickness t can cause a finite intensity for the {111} type spots shown. The Sinc function is a rapidly decaying function and would only give rise to two contrast levels for this spot, i.e, either zero intensity or some intensity. When these spots have intensity, they are half way between the transmitted beam and the {220} type spots and are thus called the {1x1} spots.

Figure 5.5 is a dark field image taken with the surface allowed, bulk forbidden {1x1} type spot. In the upper left hand corner of figure 5.5 is a diffraction pattern taken from the same area as the image. The presence of the {1x1} type spots in the diffraction pattern to a first approximation, are due to an incomplete stacking sequence along the $\langle 001 \rangle$ direction of the crystal. Because these spots are due to an incomplete stacking sequence, these spots are both surface and bulk sensitive. The identification of a stepped surface can be determined from the diffraction pattern immediately. If the surface {1x1} type spots are examined, they are seen to be split along the $\langle 220 \rangle$ direction of the bulk lattice but the bulk {200} spots are not split. This splitting in the {1x1} type spots is seen to exist irrespective of crystal tilt indicating that it is not the result of a diffraction

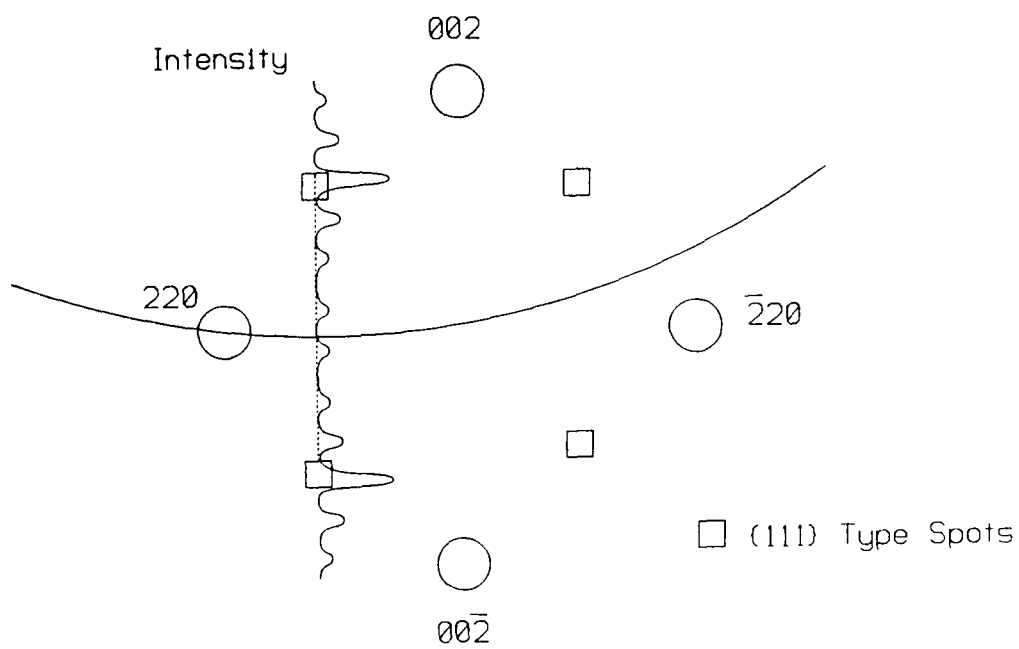


Figure 5.4. A schematic diagram in reciprocal space showing the origin of the $\{1x1\}$ type spots. The electron beam is parallel to the $[001]$ zone axis of the crystal, viewed down a $\langle 110 \rangle$ direction. The intensity distribution of the $\{111\}$ type spots is shown.



Figure 5.5. A dark field image taken with the $\{1 \times 1\}$ spot. Steps can be seen running throughout the image. Closer examination reveals that the step contrast has at least three different levels of grey. Inset in the upper left hand corner is a diffraction pattern of the same area. the $\{1 \times 1\}$ spots are split and diffuse, while the bulk spots are not, which indicates the presence of steps.

effect but is a true property of the crystal. The splitting of the $\{1 \times 1\}$ type spots coupled with the lack of splitting in the bulk diffraction spots indicates the presence of a regular array of steps; if there were a small number of steps, these spots would be streaked and diffuse. These spots are split along the $\langle 220 \rangle$ direction of the bulk crystal, which means that the steps are running in a direction normal to this. If the image is now examined, contours of different contrast levels can be seen running diagonally throughout the image. These contours are contrast from steps and white particles can be seen throughout the image. By closer examination of the dark field image in figure 5.5, at least three contrast levels can be seen ranging from whitish grey to almost black. As was mentioned earlier, if the kinematic analysis of these images given is used there should be only two distinct contrast levels for a $[100]$ zone of an fcc crystal. A complete stacking sequence would give an intensity in the final image of zero. For an incomplete stacking sequence however, the intensity from the $\{1 \times 1\}$ spots would have a non-zero value, hence two contrast levels. It is clear from figure 5.5 that a more complete analysis of this contrast in terms of the dynamical theory of diffraction is necessary in order to completely understand the digital step contrast seen in images like figure 5.5.

§ 5.5 Ir (001) (5x1) RECONSTRUCTION

§ 5.5.1 DIFFRACTION PATTERN ANALYSIS AND PARTICLE IDENTIFICATION

After the oxygen plasma cleaning and the appropriate outgassing of equipment, subsequent surface cleaning cycles produced the (5x1) reconstructed surface. The most convenient method of explaining the reconstruction is to first explain the diffraction pattern from a reconstructed area, and then to evaluate the dark field images of the reconstruction. The diffraction pattern contains all of the information necessary to determine the nature of the reconstruction while the images provide affirmation of the information in the diffraction pattern, as well as the interaction of the reconstruction with the bulk crystal.

The diffraction pattern from the Ir (001) (5x1) reconstructed surface can be interpreted in a straight forward manner. Figure 5.6 is an enlargement of a diffraction pattern showing the reconstruction. There are two types of spots in this pattern, one set of diffuse spots and one set of sharper diffraction spots. Let us begin by first explaining the sharper diffraction spots in this pattern. There are 4 spots around the central spot which are the Ir {200} type spots from diffraction with the beam down the [001] zone. Next, half way between the {200} type spots are spots labelled 'F' which are the surface allowed, bulk forbidden {1x1} type spots. There are now two sets of hexagonal spots that can be seen in the diffraction pattern. In figure 5.6, one set of hexagonal spots is arrowed and the other set is rotated 90 degrees with respect to the first set. The hexagonal spots in the pattern are due to the reconstructed hexagonal surface layer. The

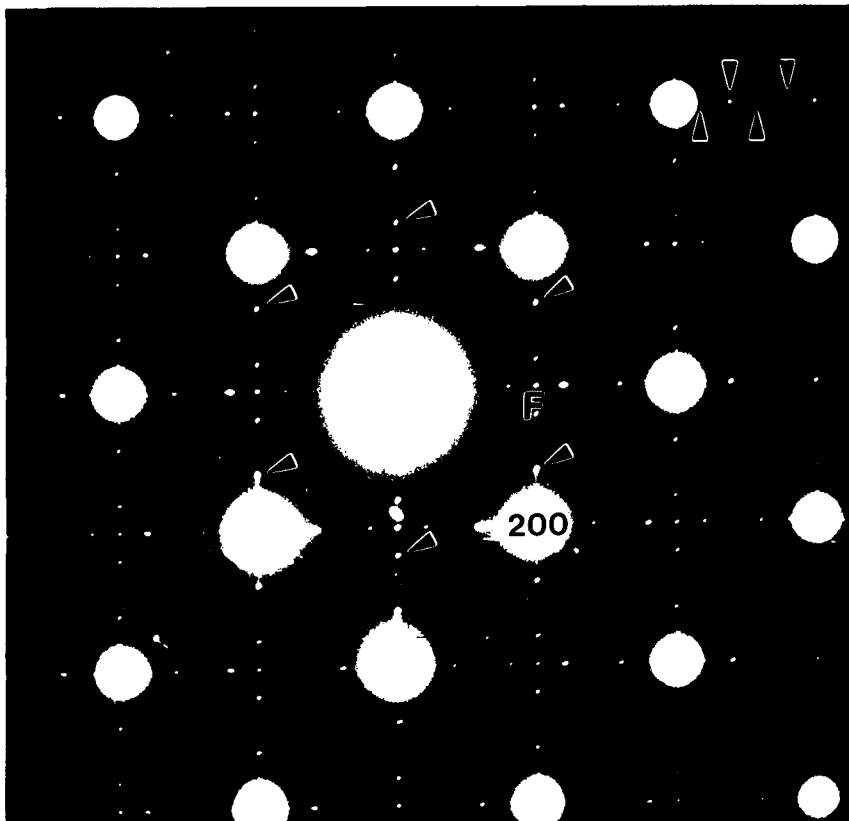


Figure 5.6. A large magnification diffraction pattern of an Ir (001) reconstructed surface. The spot marked "F" is a {1x1} type spot and an Ir {200} type spot is marked for reference. One set of surface hexagonal spots is arrowed and the other set is orthogonal to the arrowed set. In the upper right hand corner, the 1/5th order spots are arrowed and are seen to run between a {1x1} type spot and a {200} type spot.

fact that there are two distinct sets of hexagonal spots indicates the presence of two orthogonal domains. It should be pointed out that the hexagonal reconstructed layer is similar to that of the Au (001) surface because there is a contraction of the hexagonal layer to fit onto the bulk quadratic layer. The hexagonal layer is not really a regular hexagon but has one side, the side collinear with the $\{1 \times 1\}$ spots, contracted by 2 % with respect to the other side. In the Au (001) (5 \times n) reconstruction there was an approximately 4 % contraction of the hexagonal layer which translates into a shift outward of the hexagonal spots from the line connecting the bulk $\{200\}$ type spots. The rest of the sharp spots in this diffraction pattern can be formed by double diffraction between the hexagonal overlayer and the bulk fcc (001) surface. If this diffraction pattern is looked at in terms of the fcc (001) surface alone, the surface unit cell is a primitive square lattice which is formed by the $\{1 \times 1\}$ and $\{200\}$ type spots. If one looks further out in the diffraction pattern between a $\{1 \times 1\}$ spot and a $\{200\}$ spot, one should see 4 spots along the line between them. Arrowed in the upper right hand corner of figure 5.6 is one such line of spots, most of which are due to double diffraction between the hexagonal overlayer and the bulk fcc lattice. These spots are equivalent to the 1/5 order spots seen in LEED patterns from this surface. Each double diffraction spot is separated by a distance of 1/5 the total distance between the bulk forbidden $\{1 \times 1\}$ type spot and the bulk $\{200\}$ type spot.

The interpretation of the diffuse spots in figure 5.6 is not as straight forward as for the reconstruction and bulk spots. There are four main diffuse spots at roughly 2/3 of the distance from the transmitted beam to the $\{200\}$ type spots in figure 5.6. There are also

four more diffuse spots that are seen to be nearly coincident with the hexagonal spot just above the $\{1 \times 1\}$ spots, but these are not as easy to see. These diffuse spots arise by diffraction from the particles that were mentioned in section 5.3. The simplest way to determine this is to consider the shape transform of these particles in the diffraction pattern. Figure 5.7 is a high resolution image where the particles are seen to have a square projected shape. If the diffuse spots in the diffraction pattern are from these particles, the shape transform of the diffraction spot should be star shaped with a maximum intensity at half the square side. These square particles are oriented so that the $\{200\}$ type fringes from the high resolution image are collinear with square diagonal. For most of these cubes, the cube diagonal is 11 to 13 times the $\{200\}$ spacing. The cube edge is therefore, $(11 \text{ to } 13)d_{200} \cos(45)$, and the ratio of the size of the diffuse spot in reciprocal space to that of the (200) spacing should therefore be $1/((11 \text{ to } 13) \cos 45)$. A quick measurement from the diffraction pattern in figure 5.6 will show that this is indeed the case.

The shape of the diffuse spots in figure 5.6 are however not star shaped but are oblong. This is most likely due to the strain associated with the misfit between the particle lattice and the Ir matrix. The Moire fringes seen within the particles themselves are due to interference between the $\{200\}$ Ir spots and the diffuse spot which would give the Moire fringe a spacing of 3 times the (200) spacing. This is indeed the case in figure 5.6. The identification of what is inside these particles is a little more difficult. PEELS spectra did not reveal any conclusive evidence to determine composition of these particles. Two possible candidates are IrO_2 or Ir_2P . IrO_2 is a rutile structure with $a=4.47$

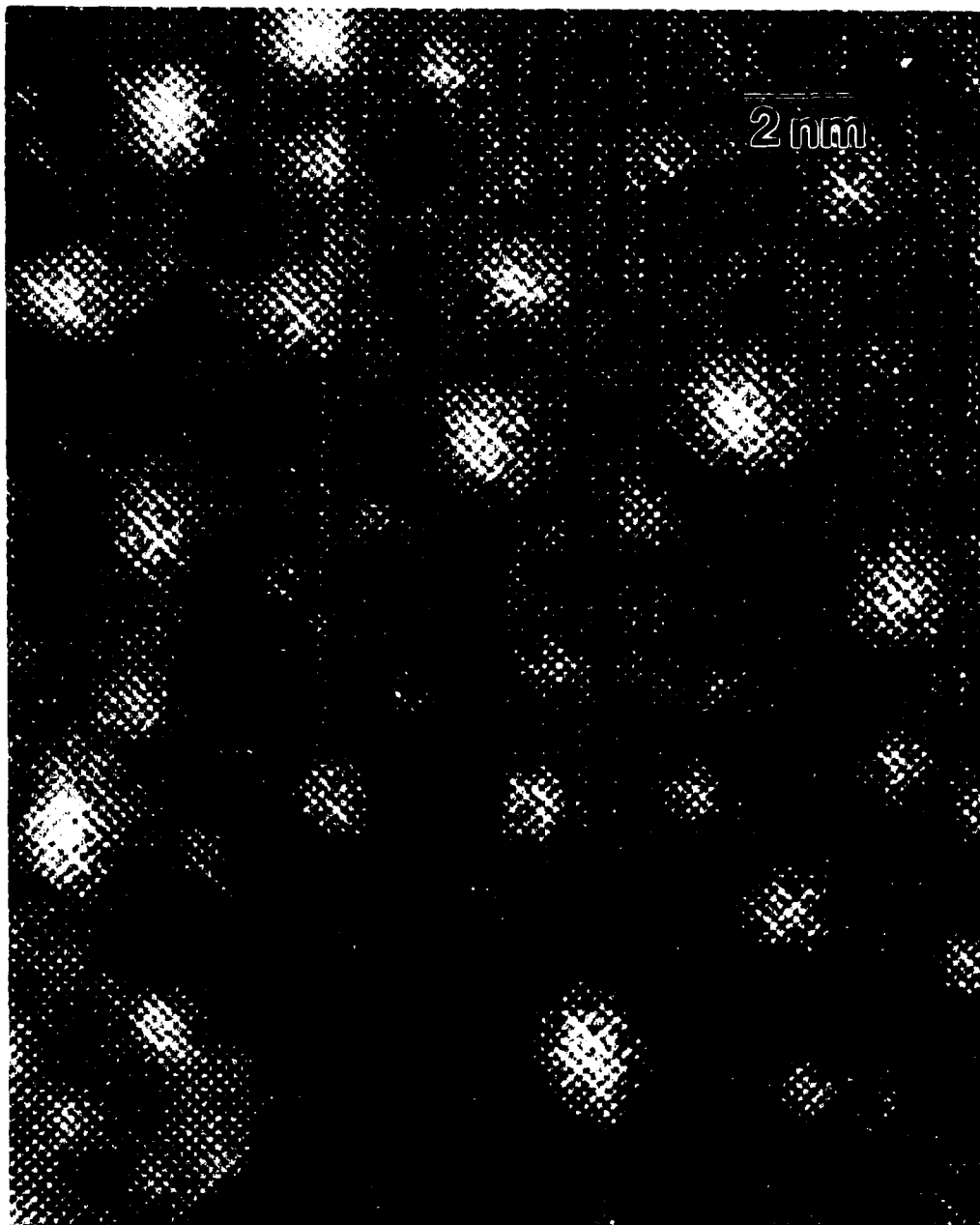


Figure 5.7. A high resolution image of IrO₂ particles. The particles have a square projection and the Ir (200) fringes are parallel to the diagonal of the square particles. There are roughly 10 to 14 (200) planes per box diagonal.

$\pm 0.02 \text{ \AA}$ and $c = 3.14 \pm 0.02 \text{ \AA}$ ¹⁷. Ir₂P is cubic with a lattice parameter $a = 5.46 \text{ \AA}$ ¹⁸. As was mentioned in the background, oxygen is known to diffuse in to Ir readily from the surface⁷. This diffusion would be appreciably enhanced by the elevated annealing temperatures used to coerce the reconstruction. If the particles were IrO₂, they would have to be oriented with the *c* axis of the unit cell parallel to the beam direction. The indexing of this case would be similar to indexing an [001] oriented bcc crystal. The diffuse spots inside the Ir {200} spots could then be indexed as {110} type spots and those at (1, 6/5) would be the {200} type spots. The ratio between the *d* spacing of the {200} spots, to that of the {110} type spots should be 1.414 or the square root of 2. The actual ratio is approximately 1.32, which corresponds to about a 6 % error over what the value should be. A good portion of this error is due to the difficulty in obtaining accurate distances between the diffuse spots. Measuring the *d* spacing of the {110} type spots from figure 5.7, the d_{110} spacing of the particles is 3.0 \AA . The d_{110} spacing for IrO₂ should be 3.2 \AA , which represents a 6 percent error. Some of this is due to the inability to accurately measure the diffuse spots as well as the probability of strain distortions to fit the rutile oxide into the Ir matrix. For supporting evidence, one could count the number of particles in dark field images taken with the {200} type spot that exhibit the Moire fringes versus the total number of particles. Because one is counting in a dark field image, there are three possible orientations of the particles. One is with the *c* axis parallel to the beam and the other two are with the *c* axis normal to the beam. The case where the *c* axis is normal to the beam produces Moire fringes between the IrO₂ {110} type spot and the Ir { 200 } spots. When the *c* axis is perpendicular to the beam there

are two distinct orientations, one with the IrO_2 $\{001\}$ spot in the aperture and one with the $\{110\}$ spot in the beam. The zone axis of the particle in this case would be the $[011]$ axis parallel to the beam. In this case $2/3$ of the particles seen in the dark field image should show Moire fringes. Out of 154 particles counted, 98 were found to have the fringes, which is roughly 64 % of the particles. This is a pretty good fit considering the low number of particles counted. It should however be kept in mind that not all particles could be counted in the dark field prints. The reason for this is that some of the particles were over exposed or under exposed. As such, the statistical evidence presented is convincing, but more work needs to be done to conclusively identify the composition of these particles.

The possibility of Ir_2P cannot be ruled out apriori, but there is a problem with this assumption. Examination of figure 5.7 shows that not all the particles exhibit Moire fringes. If the particles were Ir_2P which is a cubic structure, the Moire fringes would appear in all particles. The fact that they don't implies the structure is not cubic and not all the particles are oriented with the c axis along the beam direction.

§ 5.5.2 IMAGES OF THE RECONSTRUCTED Ir (001) (5X1) RECONSTRUCTION

The primary imaging technique used to image the reconstructed surface was centered dark field imaging with an objective aperture that allowed the information $\{200\}$ spot and the satellite reconstruction spots but not the (1×1) spots. Figure 5.8 is a dark field image taken with the bulk $\{200\}$ and associated satellite spots from the reconstruction. The dark Moire fringes running from top to bottom in figure 5.8 are

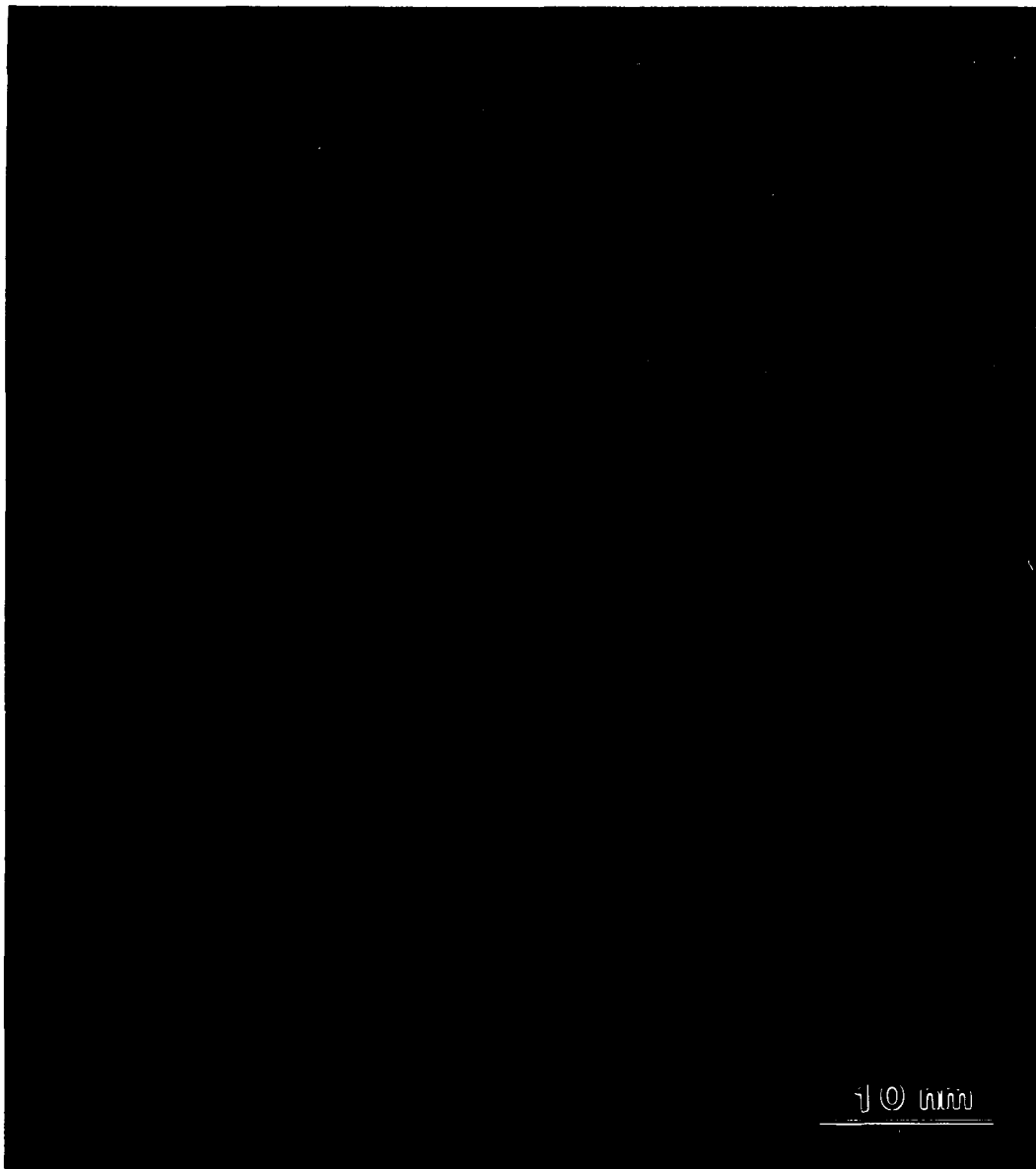


Figure 5.8. A dark field image taken with the $\{200\}$ bulk spot and associated reconstruction spots. The objective aperture used was large enough to let several reconstruction spots contribute to the image, but not the $\{1\times 1\}$ spot. Running top to bottom are Moire fringes from the '5' dimension of the $\{5\times 1\}$ reconstructed surface. Roughly normal to these fringes are another set of Moire fringes which are from the '1' dimension.

Moire fringes from the interference between the surface hexagonal or the $2/5$ reconstruction spot and the $\{200\}$ spot. As such, the spacing of this Moire fringe should be $5 d_{111} / 2$ or 6.8 \AA . These fringes are indeed 6.8 \AA and closer examination of figure 5.8 reveals that there are some smaller Moire fringes roughly normal to these fringes. These fringes are from the '1' dimension of the reconstructed unit cell. The black and white squares that are seen throughout this image are the particles described in the last section. It is clear from figure 5.8 that this reconstruction is more strongly coincident with the bulk surface than for the Au (001) $(5 \times n)$ reconstruction. The fringes from the Ir (001) surface do not wind and bend along the surface. This reconstruction occurs in very straight bands and terminates abruptly. Furthermore, the (5×1) reconstruction is not affected by the presence of the particles and does not bend around them. In some areas the reconstruction can be found in single unit cell wide configurations and in others covers rather large areas.

During this particular experiment, we looked explicitly for the interaction of bulk defects with the (5×1) reconstruction. Figure 5.9a is a dark field image taken with the bulk $\{200\}$ spot and the associated reconstruction spot near a dislocation. The Moire fringes from the '5' dimension of the reconstruction can be seen running in bands from left to right and top to bottom. There is a dislocation central in this image and the bands of reconstruction can be seen to run past the dislocation without being affected in the slightest by the strain field of the dislocation. Figure 5.9b is a similar dark field image of the reconstruction near a profile edge of the sample. The Moire fringes from the '5' dimension of the reconstruction can be seen to run in straight bands as before and are also

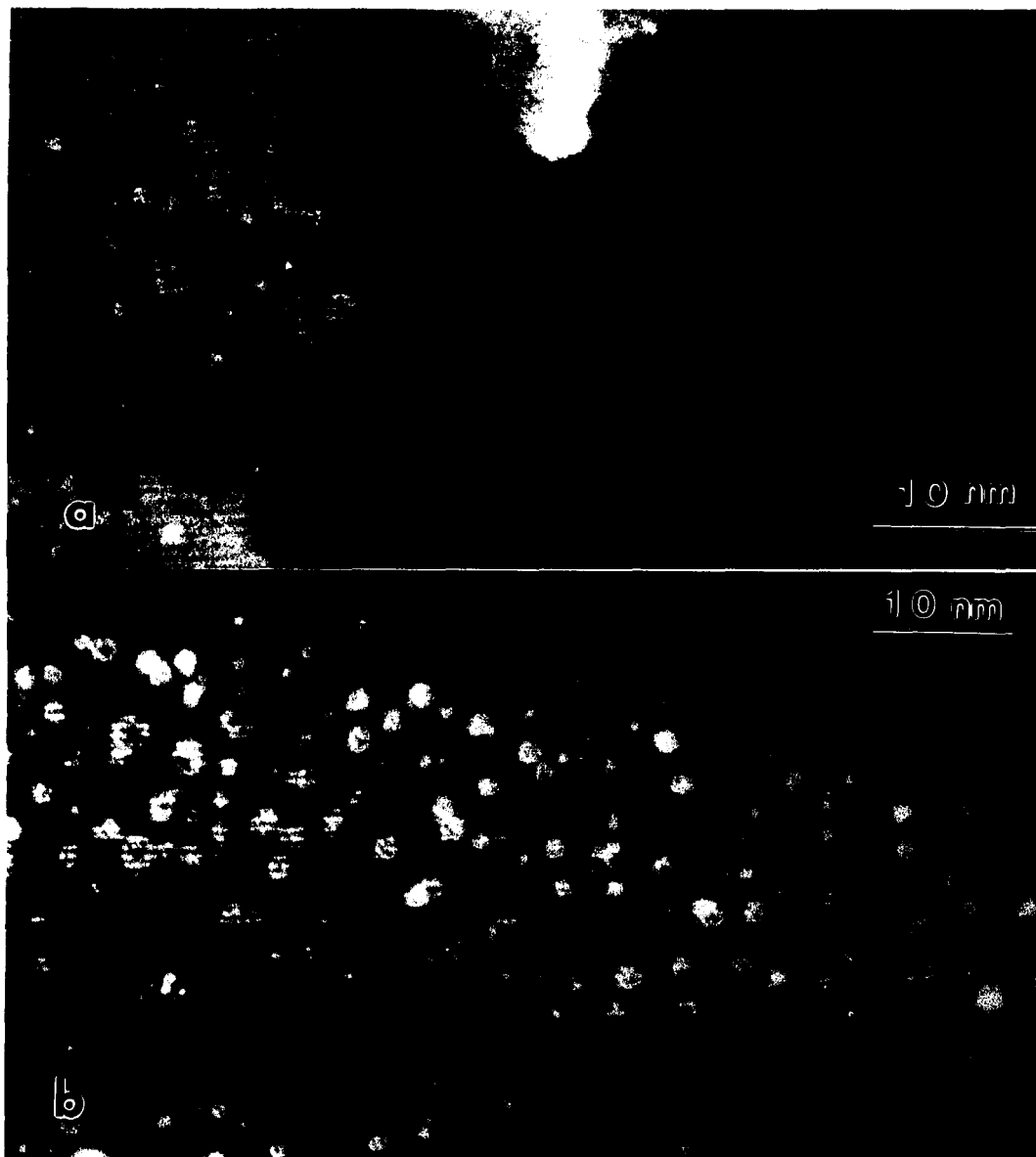


Figure 5.9. (a) A dark field image taken with the bulk $\{200\}$ and associated surface reconstruction spots in the objective aperture. Two domains from the reconstructed surface can be seen to run, unaffected by a dislocation in the center of the image. (b) A similar dark field image showing the surface reconstruction near a profile surface. The Moire fringes from the reconstruction are not bent due to the presence of the profile surface. The reconstruction is seen to step down abruptly to accommodate the curvature of the surface.

not affected by the presence of the curved profile surface. The reconstruction seems to step down to accommodate the curve in the surface, but there is no bending of the Moire fringes per se with the surface. Other dark field images were taken of similar areas of the reconstructed surface in the presence of bulk defects but in no case could the reconstruction be seen to bend around the defect.

§ 5.6 DISCUSSION OF Ir (001) (5X1) RECONSTRUCTION

The reconstruction of the Ir (001) surface has some similarities with the reconstructed Au (001) surface, but also possesses some stark differences. The similarities between the two surfaces are that both surfaces reconstruct by way of a hexagonal overlayer superimposed on the bulk fcc (001) surface. In the case of the Au (001) surface, a 4 % contraction of the reconstructed overlayer is seen and in the case of the Ir (5x1) reconstructed surface, there is a 2 % contraction of the hexagonal layer. No evidence for the tension field suggested by Lehwald⁷ is seen in the (5x1) reconstructed overlayer.

The Ir reconstruction occurs in bands and was seen to cover large areas as well as to occur in single unit cell bands. These bands seem to be locked in to the surface in straight rows and terminate in integral numbers of bands. The Au (001) reconstruction began in patches and covered larger areas of the surface with increasing surface treatments. The Au (001) (5xn) reconstruction was found to be very sensitive to the presence of bulk defects, such as dislocations and stacking faults near the surface. It was shown in chapter 4 that the presence of stacking faults in particular caused the

reconstruction to bend around the defect and in some cases caused complete termination of the reconstruction. No such interaction was found in the case of the Ir (5x1) reconstruction both in the presence of a dislocation and the IrO₂ particles. In a sense, this is proof positive that the interaction of defects with the Au (5xn) reconstruction was in fact a true interaction rather than a diffraction effect.

Another interesting aspect of this reconstructed surface is the decrease in concentration of surface steps with the advent of the reconstruction. Examination of diffraction patterns like that in figure 5.6 and others show no evidence for the existence of the arrays of steps seen before the reconstruction. This phenomena has been seen in LEED, but was attributed to the possibility of the step terraces being larger than the coherence length of the LEED beam. UHV-TEM does not suffer from this problem, but there was still no evidence for the large step concentration seen before the reconstruction.

From the images presented in the last section, it is not possible to determine the registry of the reconstructed overlayer with the bulk surface. It may however be possible to compare good quality high resolution images of the reconstructed surface with simulated images to determine the registry of the reconstructed overlayer with the bulk (001) surface. It should however be pointed out that high resolution images are difficult to take in UHV. The reason for this is that there is no amorphous contamination around to correct astigmatism and beam tilt in the usual way.

Finally, a word should be said about the surface step analysis done in section 5.3. The presence of digital step contrast with four distinct contrast levels is an area for future study. The traditional explanations for the visibility of surface steps due to Cherns cannot

explain this type of contrast variation. A more comprehensive dynamical diffraction study must be undertaken before any definitive conclusions can be drawn about the number of contrast levels possible for a given step configuration.

To summarize, the Ir (001) surface was found to reconstruct into two hexagonal orthogonal domains with a (5x1) coincidence with the bulk fcc (001) surface. There is a 2 % contraction of the hexagonal overlayer in one direction similar to what was seen in the case of the Au (001) surface. The reconstruction occurs in bands and is not affected by the presence of bulk defects or profile surfaces. The registry of the hexagonal overlayer cannot be determined from the dark field images presented here, but might be determined by HREM images and simulations. At present, such an analysis is under way but will take some time yet to complete.

CHAPTER 6

EDGE DISLOCATIONS NEAR A FREE SURFACE

§ 6.1 INTRODUCTION

The dislocation analysis described in the following chapter was begun with some very specific goals in mind. We wanted to obtain a closed form, two dimensional, linear elasticity solution for the problem of a single edge dislocation and an array of edge dislocations near the free surface of an elastic medium. At the time, we wanted to explore the ways in which the visibly high energy configurations of the surface reconstructions on the Au (001) surface and the Au (111) surface might be accommodated. More specifically, we wanted to see if it was possible to construct the surface reconstruction as an array of dislocations beneath the reconstructed surface. The results of such an analysis might help explain the observation of strong coincidence in the '5' direction of the Au (001) (5x n) reconstruction. It may also lead to an explanation of why the intensity of surface sensitive dark field images is higher than what might be expected. If the reconstruction was in fact accommodated by a subsurface array of edge dislocations, the contrast from the surface could consequently be enhanced by strain contrast from the presence of the array of dislocations. This might be especially true of reconstructed surfaces where a uniaxial contraction is part of the reconstruction process.

§ 6.2 BACKGROUND

The defect properties of misfitting overlayers have been widely examined both theoretically and experimentally for applications in epitaxial growth. Frank and Van der Merwe¹⁻² first considered the case of a misfitting overlayer in the limit where the misfit between the overlayer and substrate was taken up by a one dimensional array of edge dislocations. This solution was determined by finite difference methods and was therefore truncated at first or second order to ensure that the solution would be tractable. Since then, several authors have made varying degrees of improvements on this model by extending to the case of an overlayer of arbitrary thickness³, as well as to the case where the misfit between the over layer and substrate is taken up by two dimensional arrays of dislocations⁴. The Frank-Van der Merwe dislocation model for accommodating misfit between crystals was then extended to the case of crystal boundaries, where the difference between the two crystals is taken up by arrays of dislocations for a straight misfitting boundary, a twist boundary and finally a symmetric tilt boundary⁵⁻⁶. The solutions in this case were refined elasticity solutions based on the finite difference analysis, where a generalized Airy stress function is used. More recently, computer simulations of similar types of boundaries have been carried out based on the analyses of Frank and Van der Merwe⁷⁻⁸.

All of the above analyses have been carried out for the case of a misfitting overlayer of one material on another substrate material with varying degrees of substrate interaction. The case that this chapter will explore is the case where there is an area of misfit between two areas of a single crystal where the misfit between the two areas is

taken up by an array of equally spaced edge dislocations. This formulation has direct applications to the case of a reconstructed surface, where the misfit between the reconstruction and bulk terminated surface is taken up by an array of edge dislocations. More generally, this problem is one of examining the elastic properties of an array of edge dislocations near a free surface in an elastic half space. The approach will be to start with a single dislocation near a free surface and then by superposition construct the solutions for an array of evenly spaced edge dislocations. The two dimensional elasticity solutions for a single dislocation with burgers vector parallel to a free surface was first investigated by Head⁹, as the limiting case of an edge dislocation near a bimetallic interface. The displacements and stresses were computed using traditional potential theory. Since then several authors have investigated the behavior of dislocations in thin plates and strips near a free surface using both two and three dimensional elasticity analyses¹⁰⁻¹³. Dundurs and Mura¹⁴ have solved the more general problem of an edge dislocation near a circular inclusion. In the limit of large inclusion radius and zero shear modulus, the Airy stress function from this case can be used to find the solution of an edge dislocation near a free surface. In the present chapter, we will make use of the existing solutions of Dundurs and Mura¹⁴ and Dundurs and Sendeckyj¹⁵, to find the pertinent stress fields for the edge dislocation near a free surface. This solution is preferable to that of Head because the Airy stress function exists and does not have to be recomputed for this special case. The solution of Dundurs and Sendeckyj¹⁵ is also sufficiently general so as to make adaptation to the specific case of the array of edge dislocations near a free surface more amenable.

§ 6.3 PARTICULAR SOLUTION FOR A SINGLE EDGE DISLOCATION NEAR A FREE SURFACE

The intent of this section is to produce a two dimensional linear elasticity analysis of the case for a single edge dislocation near the free surface of an infinitely extended elastic half plane. The approach that will be used is to extract the Airy stress function for this particular case from existing general solutions rather than solving the field equation for this particular case. The appropriate stress and strain field can then be determined by the usual differentiation of the Airy stress function, and the energy of either the single dislocation or array of edge dislocations can then be determined by calculating the work required to introduce an extra half plane or planes into the material¹⁴. It should be pointed out that the stress field and energy for the single edge dislocation near a free surface have been given by Dundurs and Mura¹⁴. The analysis for the single edge dislocation is repeated here to obtain the stress field required to extend these solutions to the case of an infinite array of evenly spaced edge dislocations.

Begin by considering the case of a single edge dislocation near a bimetallic interface shown in figure 6.1. The Airy stress function was determined for this case by Dundurs and Sendekyj¹⁵. The elastic constants defined by Dundurs and Sendekyj¹⁵ will be carried through in this analysis for the sake of consistency. The bimetallic interface consists of two infinitely extended half planes, region 1 and region 2, joined together along a common plane. The dislocation is a distance of c below the interface in region 1 and its corresponding image is a distance of c above the interface in region 2. The two half planes are characterized by their individual shear moduli G_i , $i=1,2$, and Poisson's

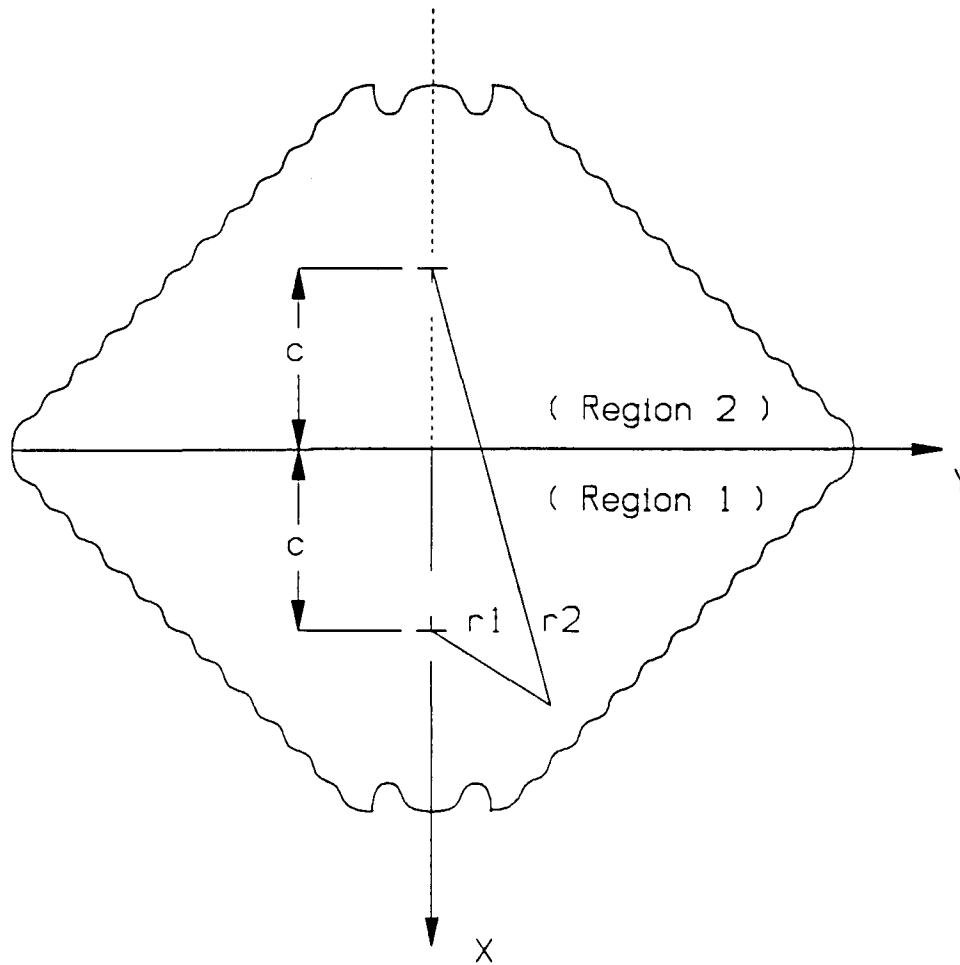


Figure 6.1. The problem description for a dislocation located a distance of c below a bimetallic interface. The image dislocation is located at c above the interface.

ratio ν_i , $i=1,2$. The following reduced constants are defined to make the representation of the Airy stress functions manageable:

$$\Gamma = \frac{G_2}{G_1} \quad (1)$$

$$\kappa_i = \begin{cases} 3 - 4\nu_i & \text{For Plane Strain} \\ \frac{3 - \nu_i}{1 + \nu_i} & \text{For Plane Stress} \end{cases} \quad (2)$$

$$A = \frac{1 - \Gamma}{1 + \Gamma \kappa_1} \quad (3)$$

$$B = \frac{\kappa_2 - \Gamma \kappa_1}{\kappa_2 + \Gamma} \quad (4)$$

$$\begin{aligned} r_1 &= \sqrt{(x - c)^2 + y^2} \\ r_2 &= \sqrt{(x + c)^2 + y^2} \end{aligned} \quad (5)$$

The Airy stress function χ for this particular case consists of two parts, one for each elastic half plane.

$$\chi_1 = \frac{Gb}{\pi(\kappa+1)} \left\{ 2r_1 \log r_1 \cos \theta_1 - (B+A)r_2 \log r_2 \cos \theta_2 \right. \\ \left. + (B-A)r_2 \theta_2 \sin \theta_2 + 2Ac \left(2 \log r_2 - \cos \theta_2 + \frac{2c \cos \theta_2}{r_2} \right) \right\} \quad (7)$$

$$\chi_2 = \frac{Gb}{\pi(\kappa+1)} \left\{ (2-A-B)r_1 \log r_1 \cos \theta_1 - (B-A)(r_1 \theta_1 \sin \theta_1 + 2c \log r_1) \right\} \quad (8)$$

To obtain the Airy stress function for the case of a single edge dislocation near the free surface of an elastic half plane, we take the limit as G_2 approaches zero¹⁶, then χ_2 is zero and we obtain a the following Airy stress function :

$$\chi_1 = \frac{Gb}{\pi(\kappa+1)} \left\{ 2r_1 \log r_1 \cos \theta_1 - 2r_2 \log r_2 \cos \theta_2 \right. \\ \left. + 2c \left(2 \log r_2 - \cos \theta_2 + \frac{2c \cos \theta_2}{r_2} \right) \right\} \quad (9)$$

We now have the case shown in figure 6.2, that is a single edge dislocation situated at a distance of c below the free surface of an elastic half space. The image field of the dislocation remains and the radii r_1 and r_2 , are the same as they were for the case of the bimetallic interface. As was mentioned earlier, we can calculate the stress field components, σ_{xx} , σ_{yy} and σ_{xy} directly by differentiating χ in the following way :

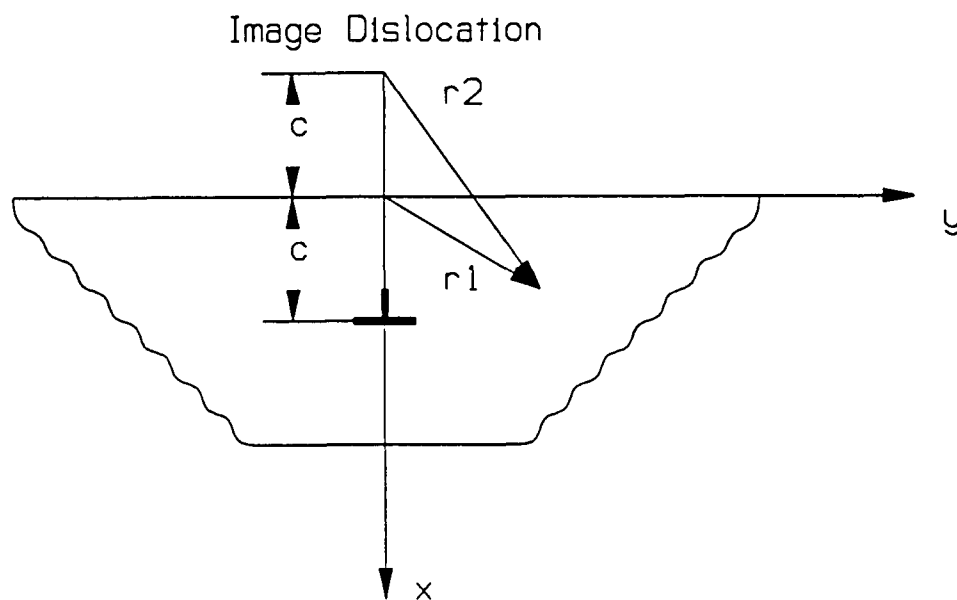


Figure 6.2. The case of a single edge dislocation near a free surface, which is a limiting case of the solution for an edge dislocation near a bimetallic interface, when the shear modulus of region 2 is set equal to zero.

$$\sigma_{xx} = \frac{\partial^2 \chi}{\partial y^2} \quad (10)$$

$$\sigma_{xy} = -\frac{\partial^2 \chi}{\partial x \partial y} \quad (11)$$

$$\sigma_{yy} = \frac{\partial^2 \chi}{\partial x^2} \quad (12)$$

As a check of the validity of the Airy stress function we obtained we can check the traction conditions. The stresses obtained by differentiation of χ must satisfy the traction conditions, which require that at the free surface ($x = 0$), σ_{xx} and σ_{xy} must be equal to zero, which can easily be verified in this case.

The pertinent stress component for our purposes is σ_{yy} , which has the following form after differentiation of χ ,

$$\sigma_{yy} = \frac{2Gb}{\pi(\kappa+1)} \left\{ \frac{3(x-c)}{r_1^2} - \frac{2(x-c)^3}{r_1^4} - \frac{(3x+5c)}{r_2^2} + \frac{2(x+c)^3}{r_2^4} \right. \\ \left. + \frac{16c(x+c)^2}{r_2^4} - \frac{12c^2(x+c)}{r_2^4} + \frac{16c^2(x+c)^3}{r_2^6} - \frac{16c(x+c)^4}{r_2^6} \right\} \quad (13)$$

It is instructive to examine the behavior of σ_{yy} at the free surface, since here it has a simple form and is most interesting in the context of surface science. At the surface or more specifically, at $x=0$, σ_{yy} has the following form¹⁶.

$$\sigma_{yy} = -\frac{16Gbc}{\pi(\kappa+1)} \frac{y^2}{(c^2 + y^2)^2} \quad (14)$$

If we now examine this function to find the value of y for which σ_{yy} is a maximum, we find by simple calculus it is for $y = \pm c$ and has a value shown below¹⁶.

$$\sigma_{yy}|_{y=\pm c} = \frac{-4Gb}{\pi(\kappa+1)c} \quad (15)$$

Plotted in figure 6.3 is σ_{yy} versus distance along the surface y , for a dislocation a distance of c below the free surface. It is clear from the plot of σ_{yy} that it is a smoothly varying function of y and does indeed have a maximum at $y = \pm c$; although, at first glance, this may seem counterintuitive. One might expect that the maximum value of σ_{yy} might exist at y equal to 0 or some multiple of the burgers vector away from $y = 0$. This is more than likely due to the image effects imposed by the presence of the free surface.

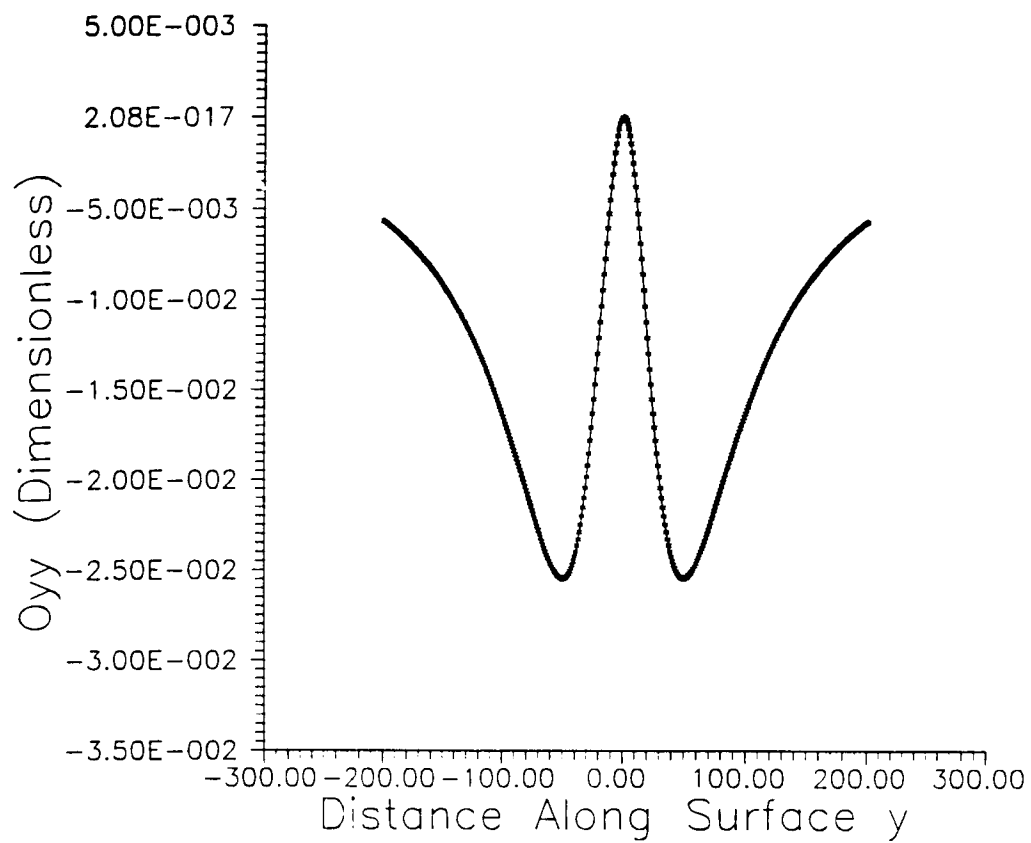


Figure 6.3. A plot of σ_{yy} at the free surface ($x=0$), as a function of distance along the free surface, y .

§ 6.4 ENERGY OF THE SINGLE DISLOCATION NEAR A FREE SURFACE

There are several different ways to calculate the energy of dislocations ranging in difficulty from the tractable to the absurd. The easiest way to calculate the elastic potential energy of a single dislocation is to calculate the work required to cut the original material, insert an extra half plane of material and close up the gap. This process is illustrated in figure 6.4. In the case of an edge dislocation with burgers vector parallel to the free surface, the only component of the stress distribution that yields a net contribution to the elastic potential energy is σ_{yy} . For an edge dislocation of constant burgers vector b , the elastic potential energy has a very simple form shown in equation (17). This energy is really just b times σ_{yy} integrated over the face of the cut made to insert the extra half plane into the material¹⁴.

$$E_p = \frac{b}{2} \int_{c+r_0}^0 \sigma_{yy}|_{y=0} dx \quad (16)$$

The result of this integration can be written as the sum of 2 terms as is shown in the following equation.

$$E_p = \frac{Gb^2}{\pi(\kappa+1)} \left\{ \frac{1}{2} \ln \left[\frac{(2c+r_0)^2}{r_0^2} \right] - \frac{2c(c+r_0)}{(2c+r_0)^2} \right\} \quad (17)$$

The terms in E_p , can be broken down into individual components which can further be analyzed. The first term is a logarithmic term which is the standard energy term for

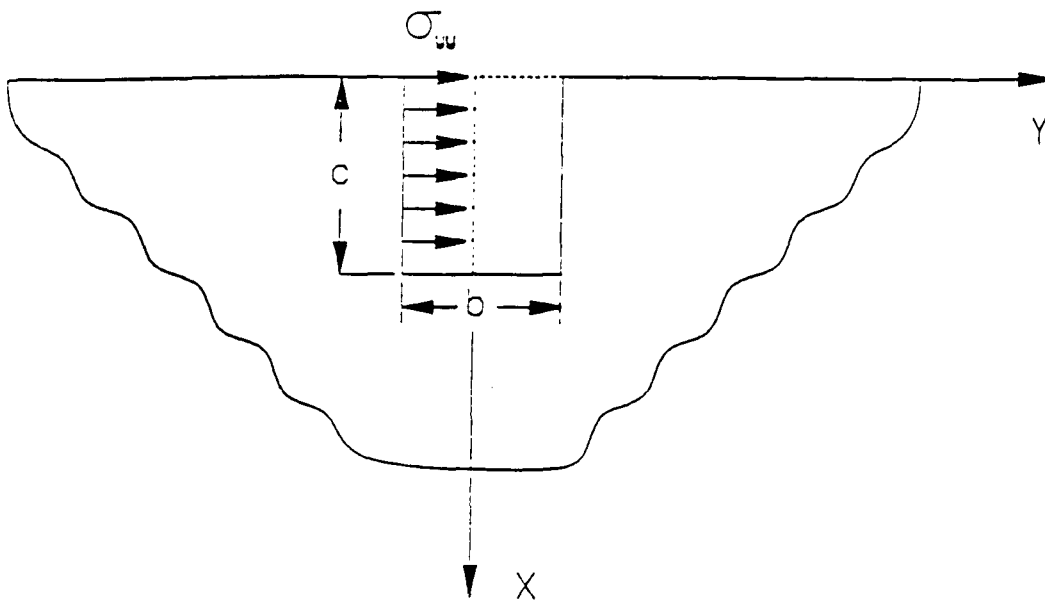


Figure 6.4. A schematic diagram of how to calculate the elastic potential energy, E_p , for an edge dislocation near a free surface.

an edge dislocation and suffers from the same problem that bulk dislocation energies suffer; i.e., the term increases without bound as a function of crystal size. The second term has a constant limit and is associated with the image dislocation. This energy is plotted as a function of c in figure 6.5. The dominant term in this function is the logarithmic term and as a result, the energy has the approximate shape of a logarithmic function.

The single dislocation energy is what was expected¹⁴, but there is more predictive information that can be gleaned from this function. Let us now explore the case where a single dislocation already exists in the material, and a new dislocation is introduced a distance of d along the surface away from the first dislocation. The energetics of this case can be written immediately from E_p by writing the sum of the original E_p , and then E_p evaluated at $y=y+d$, and in terms of a new depth variable c_1 . This new function will be called E_{pintro} , and if we plot E_{pintro} versus c_1 we obtain the curve shown in figure 6.6. From figure 6.6, it is clear that there is no new energetically favorable positions due to the presence of the other dislocation. In fact, E_{pintro} has the same functional shape as the energy of a single dislocation, shifted upward by an amount equal to the energy of a single dislocation situated at a distance of c below the surface.

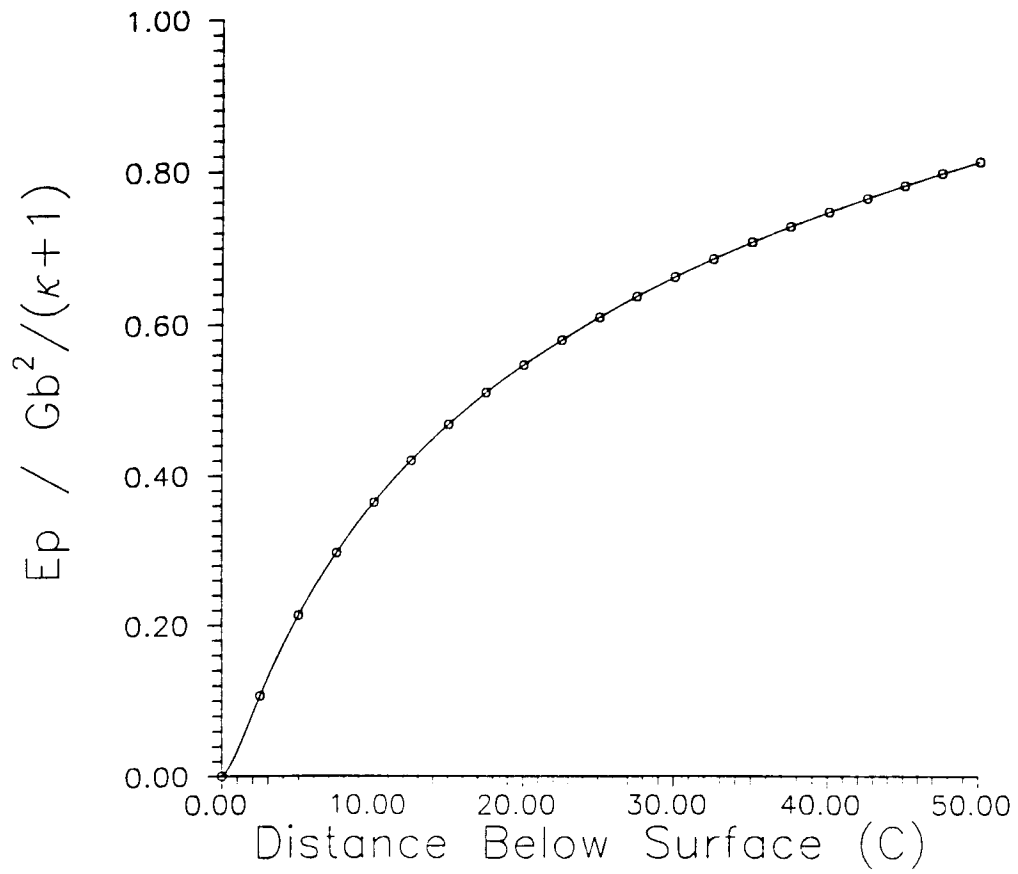


Figure 6.5. The elastic potential energy E_p , for an edge dislocation a distance of c below the free surface of an elastic half-plane, plotted as a function of c .

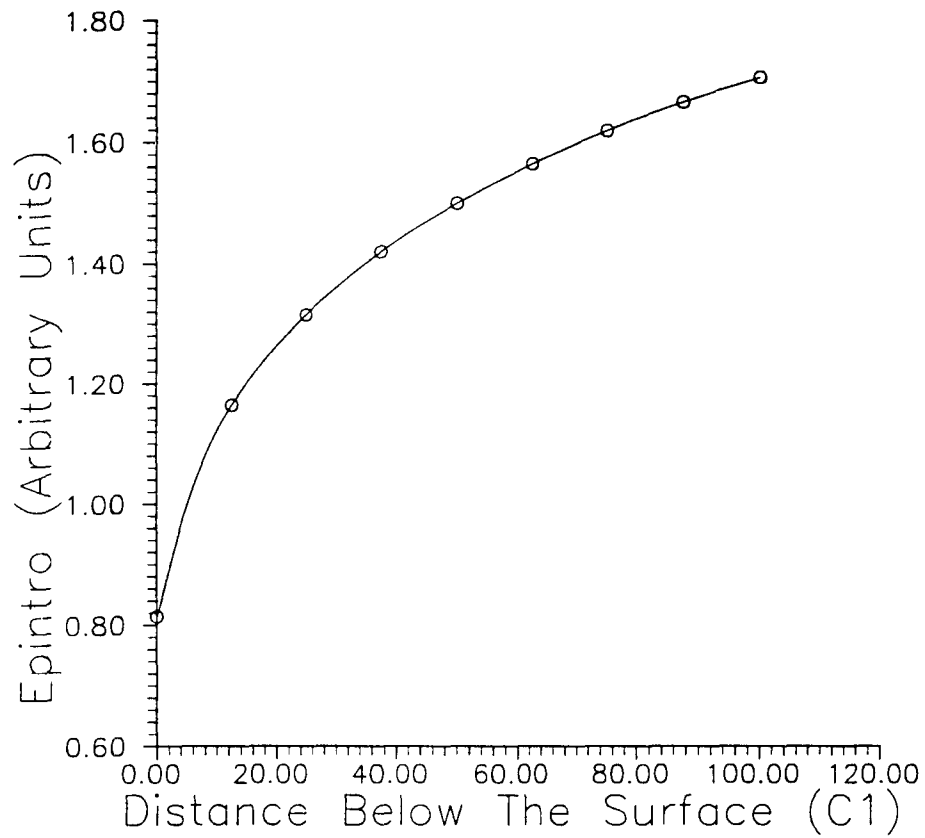


Figure 6.6. A plot of the energy of introducing a new edge dislocation E_{pintro} , into a material which already has a single dislocation situated at c .

§ 6.5 STRESS DISTRIBUTION OF AN ARRAY OF EDGE DISLOCATIONS

In order to calculate the elastic potential energy of an array of evenly spaced dislocations, we need to construct the appropriate stress field σ_{yy_array} . By the use of the superposition principle, we can construct σ_{yy_array} for the array by superimposing the stress distribution of single dislocations at integral values of the dislocation spacing d , which can be written in the following way.

$$\sigma_{yy_array} = \frac{2Gb}{\pi(\kappa+1)} \sum_{n=-\infty}^{\infty} \left\{ \begin{aligned} & \frac{3(x-c)}{(x-c)^2 + (y-nd)^2} - \frac{2(x-c)^3}{((x-c)^2 + (y-nd)^2)^2} \\ & - \frac{(3x+5c)}{(x+c)^2 + (y-nd)^2} + \frac{2(x+c)^3}{((x+c)^2 + (y-nd)^2)^2} + \frac{16c(x+c)^2}{((x+c)^2 + (y-nd)^2)^2} \\ & - \frac{12c^2(x+c)}{((x+c)^2 + (y-nd)^2)^2} + \frac{16c^2(x+c)^3}{((x+c)^2 + (y-nd)^2)^3} - \frac{16c(x+c)^4}{((x+c)^2 + (y-nd)^2)^3} \end{aligned} \right\} \quad (18)$$

The next step in the analysis is to find a closed form expression for the summation formula for σ_{yy_array} given in equation (18). In general, we seek a method of finding a closed form expression for infinite sums of real valued functions, where the function depends on the index of summation i . A somewhat contrived but nevertheless useful way of doing this has been suggested by Morse and Feschbach¹⁷. The principle behind this summation scheme is to replace the index variable i with a complex variable z , then find a function ϕ , with simple poles at integral values of z . As long as $f(z)$ has no essential singularities we can then proceed to form the following composite function. We want to find a function ϕ which has simple poles at $z=0, \pm 1, \pm 2, \dots, \pm\infty$, is bounded

at ∞ , and has a residue of 1. One such function is $\cot(\pi z)$ for positive $f(z)$ and for $f(i)$ alternating in sign, $\operatorname{csch}(\pi z)$ has simple poles at $z=0, \pm 1, \pm 2, \dots, \infty$, is bounded at ∞ , and has residue $(-1)^z$. A composite function is then constructed which is the product of $\pi\phi$ with the real valued function $f(i)$, for which a sum is required. If we replace the index variable i with a complex variable z , we can then consider the contour integral of the composite function for successive contours in the complex plane. Shown in figure 6.7 is a series of contours that might be used as well as the poles of the function $f(i)$. If we consider the first contour C_0 , we have the following result for the contour integral around C_0 .

$$\oint_{C_0} \pi \cot(\pi z) f(z) dz = f(0) + \sum \operatorname{Res}(\pi \cot(\pi z) f(z)) \Big|_{z = \text{poles of } f(z)} \quad (19)$$

$$\oint_{C_0} \pi \cot(\pi z) f(z) dz = f(0)$$

From figure 6.7 we see that there are no poles of $f(z)$ inside contour C_0 , so the sum of the residues of $f(z)$ is zero, and we have $f(0)$ or f evaluated at the pole of ϕ as the result of the integral by the Cauchy integral formula. If we now evaluate the contour integral about successively larger contours C_j we generate the following result for the C_∞ contour.

$$\oint_{C_\infty} \pi \cot(\pi z) f(z) dz = f(0) + f(-1) + f(1) + \dots + f(\pm\infty) + \sum \operatorname{Res}(\pi \cot(\pi z) f(z)) \Big|_{\text{Poles of } f(z)} \quad (20)$$

Now if the following limit condition holds on the function $zf(z)$ at ∞ , then the contour integral around the contour at infinity is zero. That is,

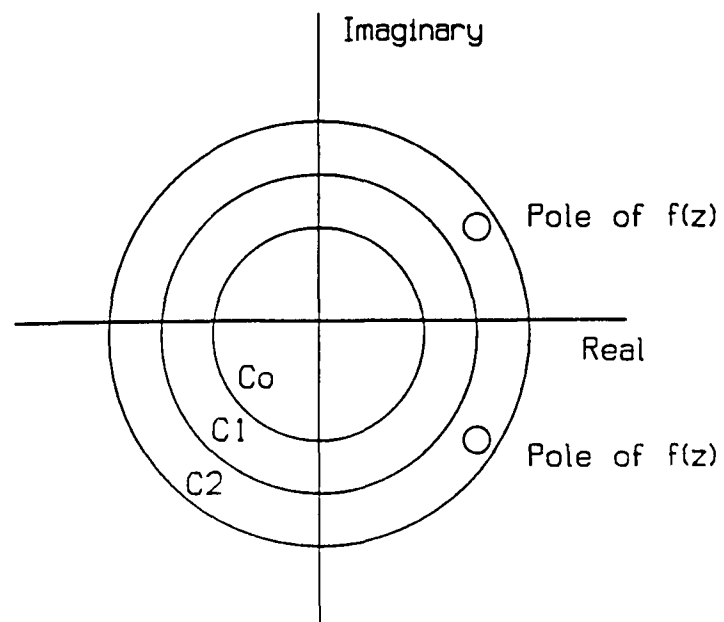


Figure 6.7. A series of contours to illustrate the summation scheme used to determine the functional form of σ_{yy} for an array of edge dislocations.

$$\text{if } \lim_{|z| \rightarrow \infty} |zf(z)| \rightarrow 0 \text{ then,} \quad (21)$$

$$\oint_{C_{\infty}} \pi \cot(\pi z) f(z) dz = 0$$

We then have the following summation formula for $f(i)$ in terms of the residues of the composite function $\phi f(z)$,

$$\sum_{-\infty}^{\infty} f(i) = -\sum \text{Res}(\pi \cot(\pi z) f(z)) \Big|_{\text{poles of } f(z)} \quad (22)$$

If we now break up the sum in equation (18) for σ_{yy_array} into eight individual sums, we need only evaluate them for the lowest power of r_i^{-n} using (22). To simplify things, divide through by d to leave the index variable by itself for each sum. We can then define three parameters, α , β and γ ; here $\alpha=y/d$, $\beta=(x-c)/d$ and $\gamma=(x+c)/d$. In the following, β is used for the $1/r_1$ terms and γ is used for the $1/r_2$. We can then write the lowest power of $1/r$ in equation (18), i.e., $1/r_1^2$ in the following way.

$$\sum_{-\infty}^{\infty} \frac{3(x-c)}{(x-c)^2 + (y-nd)^2} = \frac{3\beta}{d} \sum_{n=-\infty}^{\infty} \frac{1}{\beta^2 + (\alpha-n)^2} \quad (23)$$

By applying equation (22) we obtain a closed form expression of the sum shown in equation (24).

$$\frac{3\beta}{d} \sum_{n=-\infty}^{\infty} \frac{1}{\beta^2 + (\alpha-n)^2} = \frac{\text{Sinh}(2\pi\beta)}{\text{Cosh}(2\pi\beta) - \text{Cos}(2\pi\alpha)} \quad (24)$$

The summation formulas for the higher powers of r_i^{-n} can then be obtained by differentiating the summation result for the lowest power of r_i^{-2} with respect to the parameters β or γ . The net result of applying equation (22) to the lowest power of $1/r$ in (18), and then differentiating to get the rest of the sums produces the following function for σ_{yy_array} .

$$\sigma_{yy_array} = \frac{4Gb}{d(\kappa+1)} \left\{ S_1(\beta, \alpha) + \pi\beta S_3(\beta, \alpha) - S_1(\gamma, \alpha) \right. \\ \left. - \pi \left(\gamma + \frac{2c}{d} \right) S_3(\gamma, \alpha) + \left(\gamma - \frac{c}{d} \right) \frac{4\pi^2 c}{d} S_1(\gamma, \alpha) (S_2(\gamma, \alpha) + 2S_3(\gamma, \alpha)) \right\} \quad (25)$$

The S_i have the following definitions :

$$S_1(\gamma, \alpha) = \frac{\text{Sinh}(2\pi\gamma)}{\text{Cosh}(2\pi\gamma) - \text{Cos}(2\pi\alpha)} \quad (26)$$

$$S_2(\gamma, \alpha) = \frac{\text{Cos}(2\pi\alpha)}{\text{Cosh}(2\pi\gamma) - \text{Cos}(2\pi\alpha)} \quad (27)$$

$$S_3(\gamma, \alpha) = \frac{1 - \text{Cosh}(2\pi\gamma)\text{Cos}(2\pi\alpha)}{(\text{Cosh}(2\pi\gamma) - \text{Cos}(2\pi\alpha))^2} \quad (28)$$

In the functions S_i , β is used if the term arises from a sum in powers of $1/r_1$, and γ is used if the term arises from a sum in powers of $1/r_2$.

There are some checks that should be performed in order to explore the validity of this functional representation for the σ_{yy_array} . The first of these is to plot σ_{yy_array} and σ_{yy} for the single dislocation at the free surface, versus distance along the surface in the limit as d approaches infinity. In this limit, σ_{yy_array} should be the same as the σ_{yy} for the single dislocation. Figure 6.8 is a plot of this case and as can be seen from the figure, the two functions do in fact match each other in this limit. In figure 6.8, d was taken as 1.0×10^8 Å. Another test is to plot σ_{yy_array} at the free surface versus distance along the surface as a function of d , the spacing of dislocations in the array. For decreasing d , the overall magnitude of the stress distribution increases while the variation with y is diminished. For large d , the overall stress field should be smaller, but the variation should be larger. This is indeed the case for the function in equation (25) as can be seen in figure 6.9.

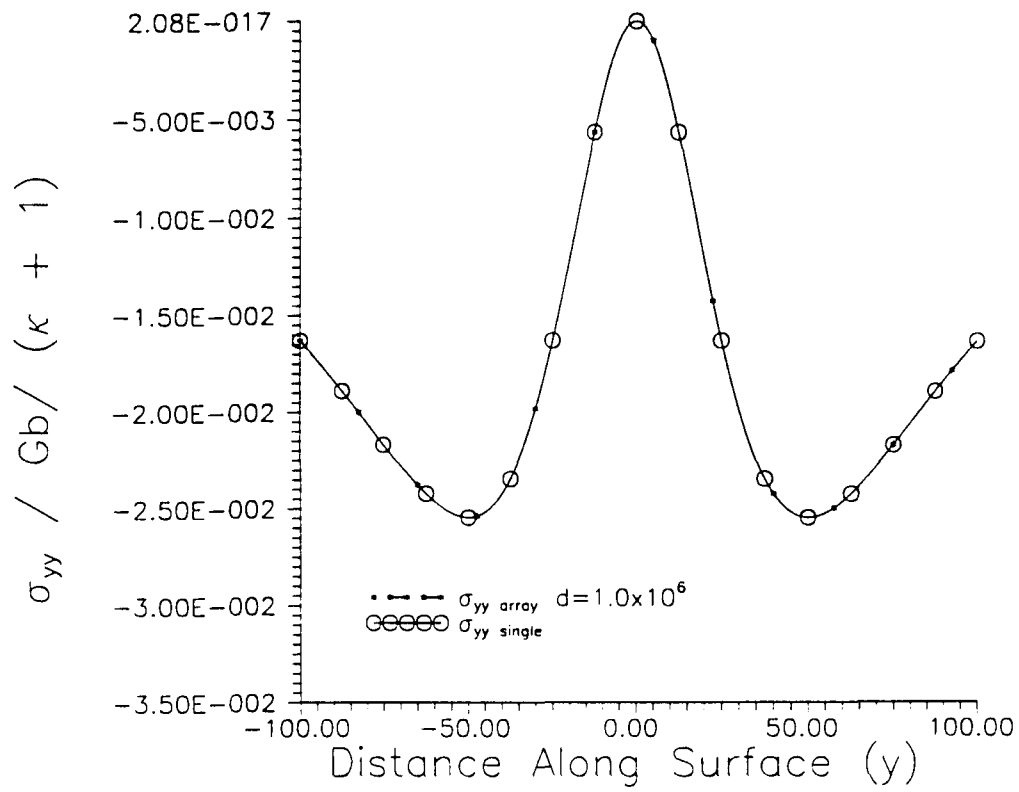


Figure 6.8. A plot of the convergence of σ_{yy_array} and σ_{yy} in the limit of large dislocation spacing d , as a function of distance along the free surface y .

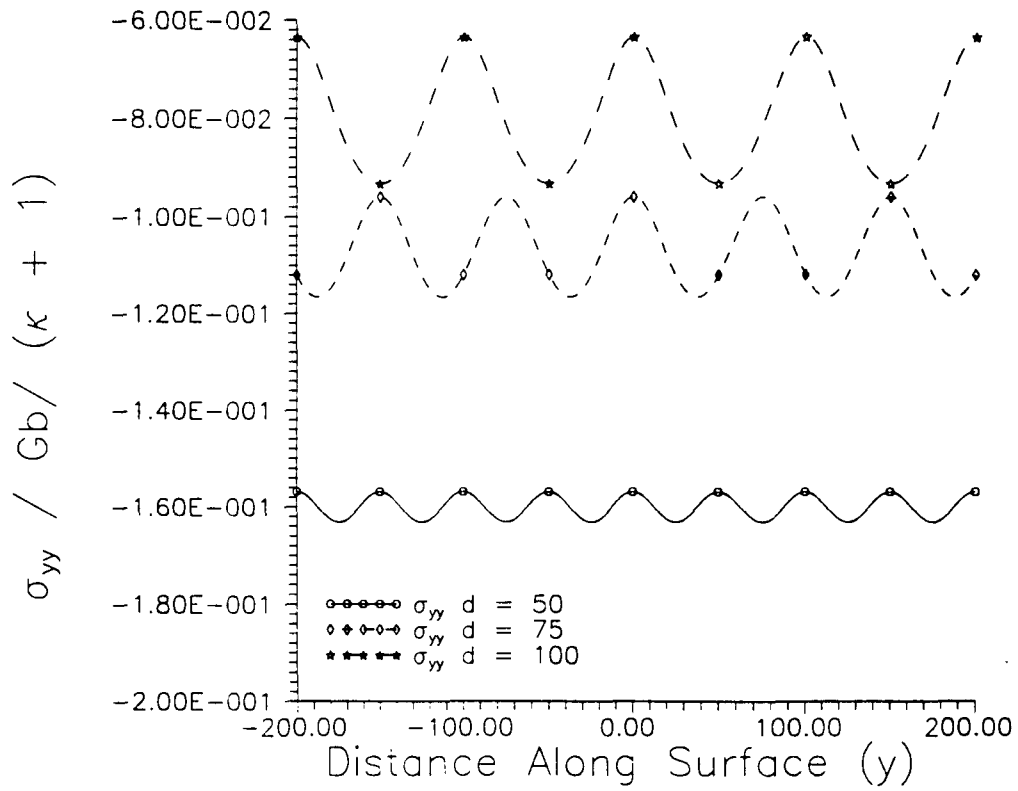


Figure 6.9. A plot of the dependence of σ_{yy_array} , as a function of dislocation spacing d , versus distance along the free surface y .

§ 6.6 THE ENERGY OF AN ARRAY OF EDGE DISLOCATIONS NEAR THE FREE SURFACE OF AN ELASTIC HALF-PLANE

The calculation of the elastic potential energy of the array of edge dislocations proceeds in the same manner as that for the single edge dislocation. The only difference being, that the work is calculated using σ_{yy_array} instead of σ_{yy} . The limits of integration are the same and the energy was found by breaking up the energy integral and integrating each term separately, and then recombining at the end to produce an indefinite integral form. The limits were then evaluated using the total indefinite integral and thus the elastic potential energy of the array. The value of the indefinite integral at $x=0$ or the upper limit is zero; thus the elastic potential energy of the array of edge dislocations is the indefinite integral evaluated at the lower limit, $x=c+r_o$, where η has the following definition.

$$\eta = \frac{2c + r_o}{d} \quad (29)$$

$$E_{p_array} = \frac{Gb^2}{\kappa+1} \left\{ \frac{1}{2\pi} \ln \left[\frac{\text{Cosh}(2\pi\eta) - 1}{\text{Cosh}(2\pi\frac{r_o}{d}) - 1} \right] + \eta \frac{\text{Sinh}(2\pi\eta)}{\text{Cosh}(2\pi\eta) - 1} - \frac{r_o}{d} \frac{\text{Sinh}(2\pi\frac{r_o}{d})}{\text{Cosh}(2\pi\frac{r_o}{d}) - 1} - \frac{4\pi c}{d^2} \frac{(c+r_o)}{\text{Cosh}(2\pi\eta) - 1} \right\} \quad (30)$$

The energy for the array has a relatively simple form consisting of four terms. The first term is a logarithmic term which depends on the distance below the surface.

The second term is the product of a linear term in η and a hyperbolic quotient. For small values of η , the hyperbolic term dominates while in the limit of large η , the hyperbolic term approaches one, and the linear portion is the dominant term. The third term is a constant and is a function of the strength of the core energies of the dislocations in the array. The strength of the core energy is reflected through the term r_0 , which is a distance around the core where the properties of the material cannot be considered elastic. This is usually taken as roughly 2-5 times the burgers vector b . The fourth and final term is a term due to the image dislocations and drops off to zero very quickly as a function of c .

The behavior of this function should be checked to make sure that no mistakes have been made in integration. The first thing to check is the behavior of the array energy in the limit of large d . If the function is indeed correct, $E_{p \text{ array}}$ should approach that of the single dislocation in the limit of large d . Figure 6.10 is a plot of E_p and $E_{p \text{ array}}$ in the limit of large d , where d is taken to be 1.0×10^8 units, and the energy of the array does in fact coincide with that of the single dislocation in the limit of large d . It is clear that in this limit, we have in fact found a suitable closed form expression for the energy of an array of edge dislocations in an infinitely extended elastic half space.

Let us now examine the behavior of $E_{p \text{ array}}$ as d is allowed to approach more finite values. Figure 6.11 is a plot of $E_{p \text{ array}}$ versus c , as a function of d . For relatively large values of d ($d=1000$), $E_{p \text{ array}}$ has the familiar logarithmic shape of a dislocation energy and can be seen to approach the single dislocation energy. When d becomes relatively small ($d=50$), this function becomes more and more linear and increases sharply. In this case,

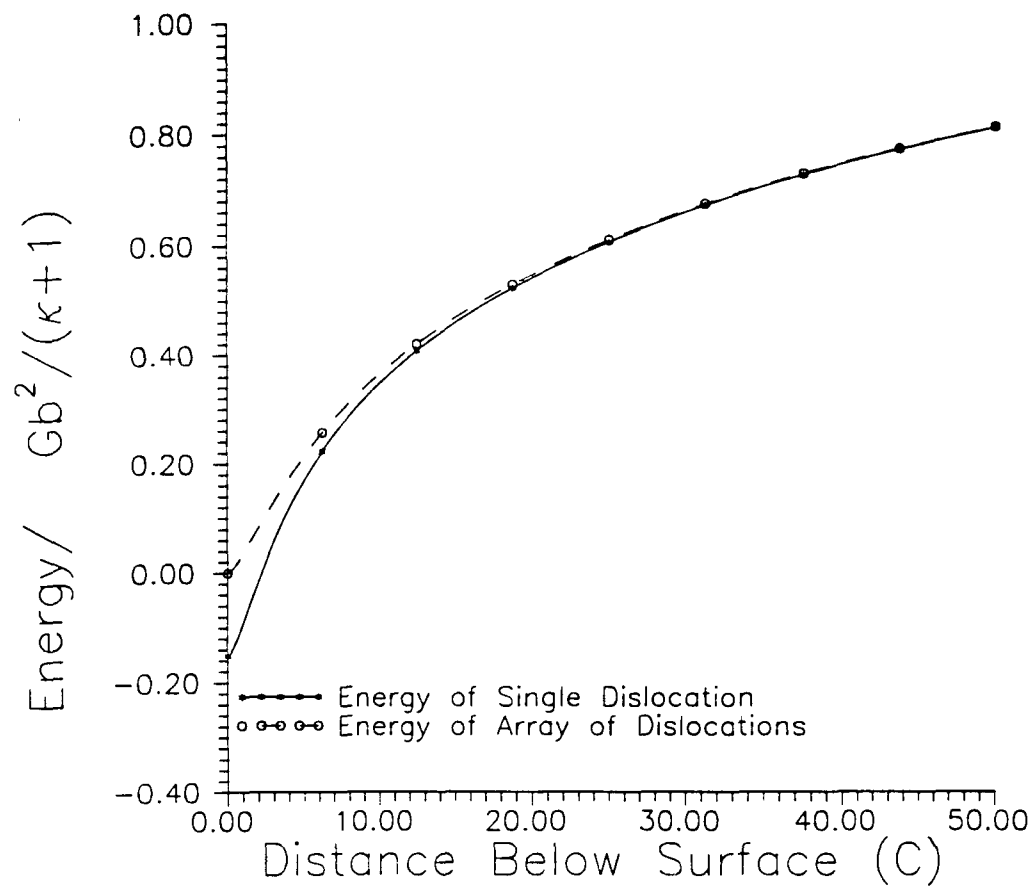


Figure 6.10. A plot of E_p and $E_{p \text{ array}}$ in the limit of large d . As should be expected, the two functions are the same in this limit.

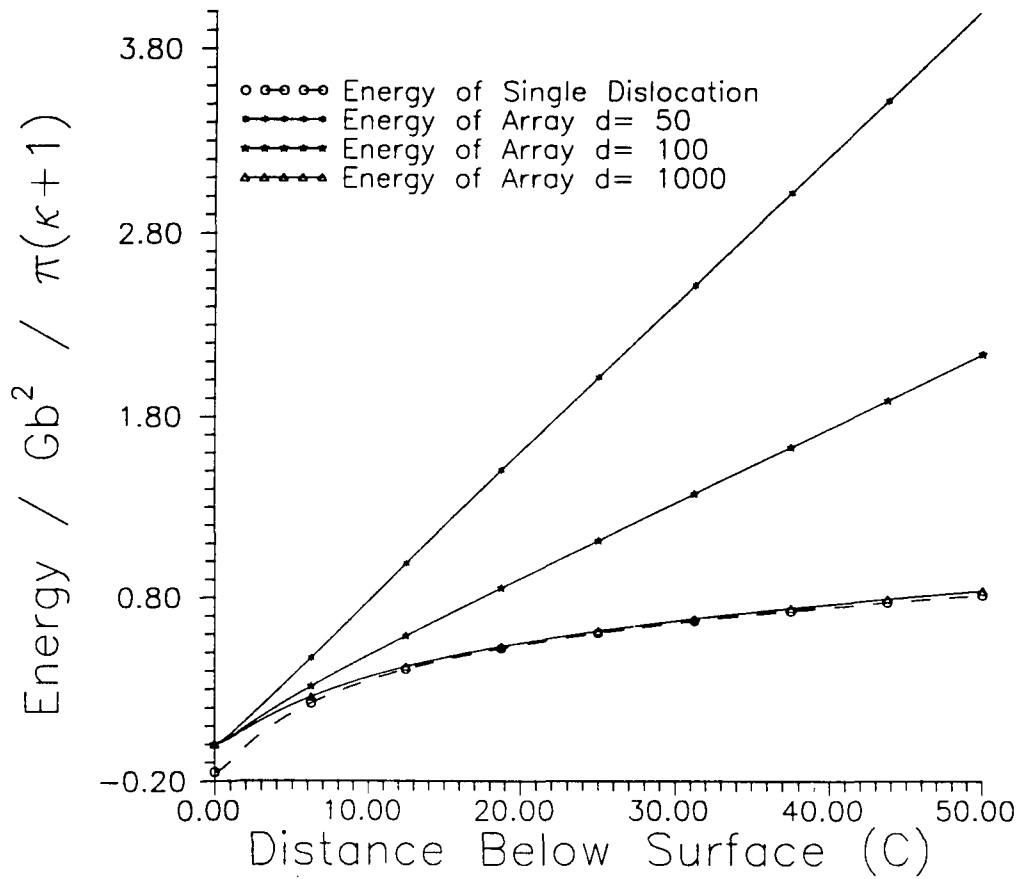


Figure 6.11. A plot of $E_{p \text{ array}}$ versus c for various values of d . For large d , $E_{p \text{ array}}$ has the typical logarithmic shape while for more finite values of d becomes linear.

the second term in equation (30) is the dominant term. It is clear from figure 6.11 that there are no interesting extremum conditions for the array of dislocations, except the trivial position at the surface itself i.e., at $c=0$. In the case of the dislocation near a bimetallic interface there are certain combinations of the elastic constants G_i and ν_i , where the dislocation can find a metastable equilibrium at some distance from the interface. It is however, not possible in this case to find an equilibrium value of c for a given dislocation spacing d .

Another interesting limit that can be explored is the limit of $E_{p \text{ array}}$ as c tends to infinity. In this limit we should expect to obtain two terms, the first term should be linear in c and equal to the strain energy for a slab of thickness c in a uniform compression film where the stress is b/d . The next term should be the energy per unit length per dislocation in a grain boundary composed of an array of dislocations. Also, the image terms should tend to zero rather quickly as a function of c . $E_{p \text{ array}}$ in the limit of large c is given in the following equation.

$$E_{p \text{ array}} = \frac{Gb^2}{\kappa+1} \left\{ \frac{4c}{d} - \frac{r_o}{d} \frac{\text{Sinh}(2\pi \frac{r_o}{d})}{\text{Cosh}(2\pi \frac{r_o}{d}) - 1} - \frac{1}{2} \ln \left[\text{Cosh}(2\pi \frac{r_o}{d}) - 1 \right] \right\} \quad (31)$$

The strain energy of a slab under a uniform compression of b/d , per unit length is given by the following equation.

$$E_s = \frac{G}{1-\nu} \frac{b^2}{d} c \quad (32)$$

If we express κ in the first term of equation (31) in terms of Poisson's ratio, we see that we obtain the result given in equation (32). The last two terms in $E_{p \text{ array}}$ are then the grain boundary energy terms for a grain boundary with this orientation. The grain boundary energies for tilt and twist boundaries can be calculated in the same way by simply adjusting the Airy stress function for differences in the burgers vector.

§ 6.7 ACTIVATION ENERGY FOR THE INTRODUCTION OF AN EDGE DISLOCATION NEAR A FREE SURFACE

It is now possible to evaluate the energetics for the case of an overlayer on a bulk crystal surface, where there is a misfit between the bulk crystal and the overlayer, which is taken up by the introduction of edge dislocations. This might be the case for a the growth of metal films on clean preexisting crystal surfaces, to make a bicrystal, or in the case of a reconstructed surface, where the reconstruction consists of a misfitting overlayer. If we assume that in the limiting case of a critical thickness, the misfit between the overlayer and the bulk surface might be taken up by edge dislocations a depth of c below the reconstructed surface; it is then possible to determine the activation energy for the introduction of edge dislocations to accommodate the misfit between the overlayer and the bulk surface. This can be accomplished by comparing the energy of an edge dislocation as a function of distance c below the free surface, versus the work released

by the uniform straining of the overlayer of thickness c . The maximum difference between these two energies for a given misfit, can be defined as the activation energy barrier for the introduction of the dislocation into this material system for a given misfit. The work released W_{rel} , is the work done against the misfit strain in maintaining the undislocated material which can be defined in the following way.

$$W_{rel} = b \int_c^0 \sigma_{yy} dx \quad (33)$$

$$\sigma_{yy} = \delta [2G + \lambda(1 - \nu)]$$

In equation (33) λ is Lamé's constant, ν is Poisson's ratio and δ is the misfit between the bulk surface and the epitaxial overlayer. If we now take the maximum difference between equations (30) and (33) in the limit of large d , we can produce a curve of activation energies versus misfit δ . Figure 6.12 is a plot of the activation energy for the introduction of an edge dislocation versus misfit δ for Au considering a $1/2$ [110] type burgers vector. It is an exponential type of decay versus misfit and reaches a value above $\delta > 1\%$ where there is no activation energy for the introduction of an edge dislocation.

It is also possible to compute a critical thickness for the introduction of an edge dislocation into the elastic $1/2$ - space versus misfit for the same Au system. The critical thickness can be defined as the value of c where the difference between the dislocation energy and the work released is equal to zero. Figure 6.13 is a typical plot of critical thickness versus misfit δ which shows a relatively sharp decay with misfit.

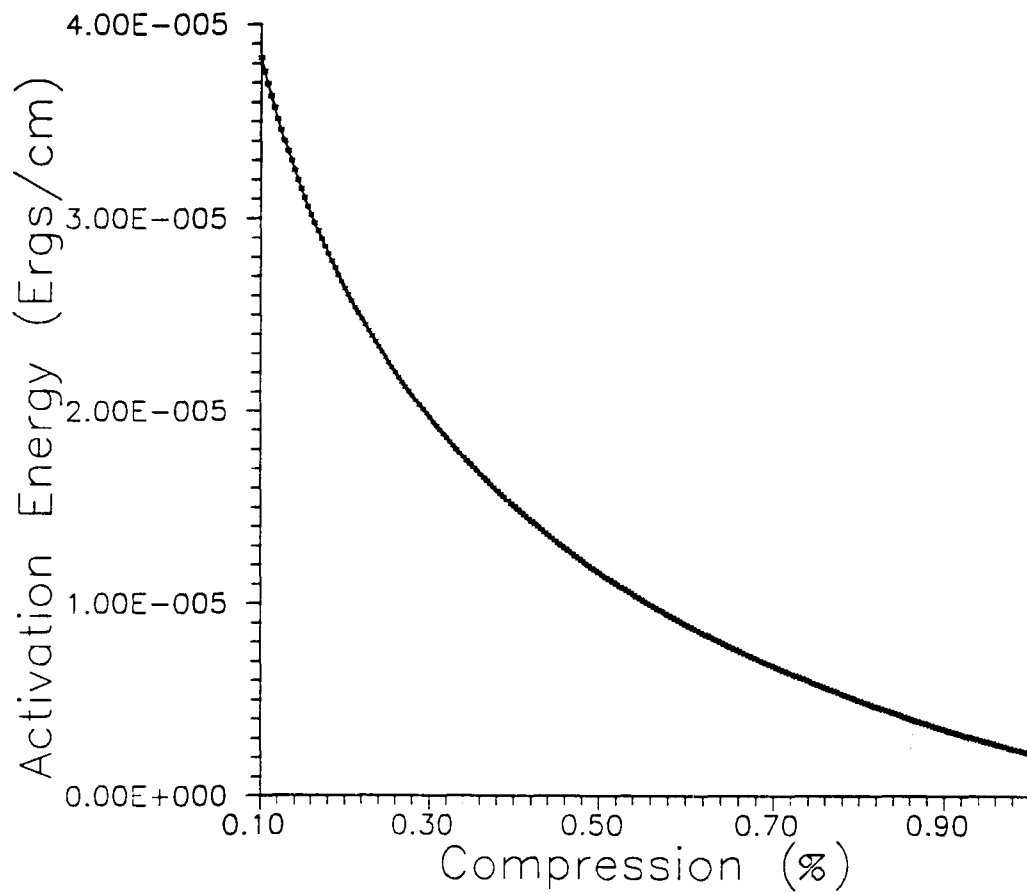


Figure 6.12. A plot of the activation energy of a misfitting overlayer versus misfit δ .

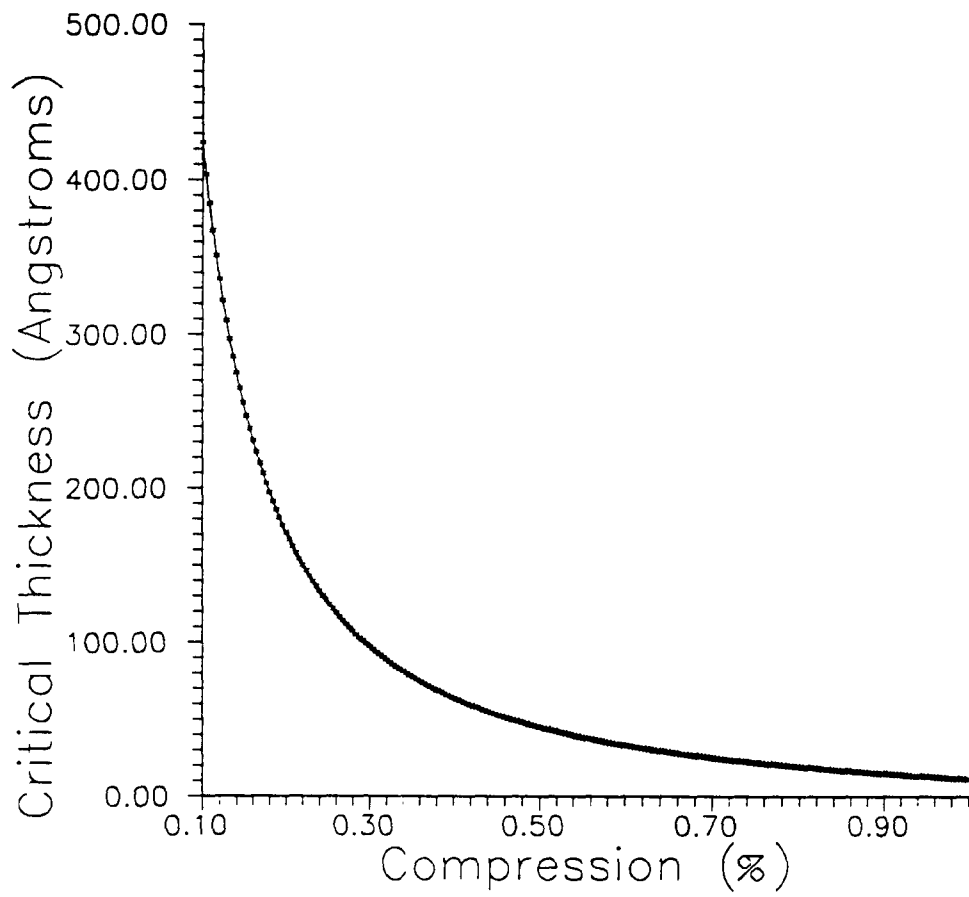


Figure 6.13. A plot of the critical thickness for the introduction of an edge dislocation to accommodate a misfitting overlayer, as a function of misfit.

§ 6.8 DISCUSSION

In this chapter closed form expressions for the stress distributions and energies of single and an array of single dislocations in an infinitely extended half space were obtained. As was pointed out earlier, the analysis for the single edge dislocation has been done before by Dundurs and Mura¹⁴. The important result here is the extension of those solutions to the case of the infinite array of evenly spaced dislocations. Also, the energy of the single edge dislocation was used to construct the activation energy for the introduction of a single dislocation into the half space, as a function of strain, as well as to calculate the corresponding critical thickness. There is no equilibrium distance for the array of edge dislocations from the free surface as might be expected. An interesting result of this analysis is the ability to extract the grain boundary energy terms from $E_{p \text{ array}}$, which can be done for several different simple grain boundaries by adjusting the Airy stress function for the proper orientation of the burgers vector.

CHAPTER 7

SUMMARY AND SUGGESTIONS FOR FUTURE RESEARCH

§ 7.1 GENERAL REMARKS

The results of this work have important implications for both TEM and surface science. The importance of this work for TEM is that it establishes UHV-TEM as a technique capable of truly studying surfaces. In the past, the poor vacuum in most microscopes was a limiting factor in the effectiveness of TEM in sorting out surface phenomena. A good example of this can be seen in the work on radiation damage of surfaces in our group. Buckett¹ has found that the carbonaceous contamination in a typical HREM vacuum can alter the damage mechanism for nickel oxide surfaces. Under conventional microscope vacuum conditions, carbonaceous contamination is seen to react with the surface, damaging it. This of course was not found to occur in UHV and could be reproduced by dosing the surface with varying amounts of CO. These environmental restrictions were overcome to a large extent by my predecessors. The true advance seen realized in this work was the implementation of surface science studies using UHV-TEM. The work of my predecessors did not really use the UHV-H9000 as a surface science tool, but as an environmental cell. In the past, most TEM investigations of surfaces were limited to surfaces that could be cleaned by heating or were inherently insensitive to

contaminants in the microscope vacuum. This was one of the key limitations that had to be overcome before UHV-TEM could be considered a true surface science tool. What was necessary was to be able to produce bulk single crystal samples similar to those used in LEED studies, that were also transparent to 300 keV electrons. Once that was accomplished, a general method for preparing clean surfaces needed to be developed. In chapter 2, a two part process that consists of mechanical polishing and ion beam thinning outside the vacuum, followed by classical surface science sputter anneal cycles once in the surface science chamber, was outlined in detail. It should be pointed out that this process can be used for not only metal specimens but also semiconductor and oxide surfaces with slight modification. The only modification necessary for oxides is to anneal the surfaces under partial pressures of oxygen in order to maintain stoichiometry. The specimen preparation process outlined in Chapter 2 was implemented in subsequent chapters for Au and Ir single crystal surfaces and has been used by others in our group to study semiconductor surfaces.

Before going any further, our ability to detect contaminants on surfaces should be discussed. In the UHV-H9000, we generally use PEELS to check the cleanliness of the bulk and surface of the specimen. In most cases, we are interested in hydrocarbon, CO, and CO₂ contamination of our surface. The carbon based contaminants arise from vacuum impurities such as backstreamed pump oils and also exist on the sample surface when it is introduced into the vacuum from air. Krivanek and Kundmann² have determined that the minimum detectable mass fraction (MMF), using PEELS for to detect Mn in gahnite to be about 0.03% for 5 nA of beam current using differential spectra. If

we do a quick calculation, a monolayer of C on 200 Å of Ir would have a mass fraction of approximately 0.06% which would be detectable under these conditions. The ionization cross section for C is arguably higher than that for Mn which augments the sensitivity of PEELS to surface contaminants. It is therefore safe to say that under the right beam conditions and collection times, we can achieve monolayer sensitivity for C in differential mode, which is adequate to determine whether we have a clean surface or not. We cannot however distinguish between amorphous C, CO and CO₂ adsorbed on the surface with PEELS alone.

The results of this work have important ramifications for the imaging of surfaces using TEM. As was pointed out in Chapter 2, it is not necessary to resort to weak beam imaging techniques in order to obtain surface sensitivity. Dark field images both on and off the zone axis provide sufficient contrast and intensity levels from surface features. It is clear from the dark field images shown in Chapters 3-5, that not only are the intensities of surface features adequate, but also, that it is possible to take relatively high resolution dark field images with reasonable exposure times. The intensity of surface reflections in transmission electron diffraction patterns is high enough to be observed in diffraction patterns with no special processing. When surface imaging is coupled with diffraction patterns, UHV-TEM offers distinct advantages over existing surface science techniques because both real and reciprocal space information can easily be gathered. Also, techniques such as LEED and RHEED can only provide averaged information from the surface and as such provide little or no local surface information. Imaging in UHV-TEM using dark field or high resolution imaging techniques provide not only local

information but also large scale morphological information from the surface. As was seen in the dark field images of the reconstructed Au thin film sample, the relationship of domains on the reconstructed surface is readily seen. In the case of the Ir (001) surface, the presence of small terrace width steps was also easily seen in dark field images using the $\{1 \times 1\}$ reflections to form a dark field image. To see small terrace width, irregularly arranged steps in LEED is not an easy task because it involves the interpretation of diffuse intensity in a highly dynamical diffraction pattern.

Perhaps the most important implication of this work was demonstrated by the interaction of bulk defects with the reconstructed $(5 \times n)$ surface. The existence of this interaction implies that the surface can no longer be considered as a separate entity for analysis; the surface and bulk crystal have to be considered as part of a single materials system, where effects from both have to be considered. UHV-TEM makes an important contribution to surface science by providing a more complete picture of the bulk and surface of a given materials system than techniques previously used such as LEED, RHEED, STM and glancing angle X-ray. While it is true that STM can provide real space information from reconstructed surfaces, it has inherent limitations for surface structure determinations. The reason for this is that it is difficult to obtain information about the relationship of the surface layer being viewed to the layers below. This makes atom position determinations for reconstructed surfaces nearly impossible using STM. Also, STM cannot provide substantive information about the relationship between bulk defects in the crystal and the surface.

In general, the results of this work firmly establish UHV-TEM as a viable technique for studying surface phenomena. The results obtained on the reconstructions of noble metal surfaces in Chapters 3-5 are significant but are not completely new. Other surface sensitive techniques have been used successfully to obtain information on reconstructed surfaces. The important result is that through the study of these reconstructed surfaces, UHV-TEM has been established as a viable technique for obtaining both local and large scale information from surfaces. If one experiment can be treated as proof positive of this fact, it would be the observation of the Ir (001) (5x1) reconstruction. This surface is one of the most difficult to clean and reconstruct by virtue of the fact that it has a sticking coefficient at room temperature for CO and CO₂ of nearly 1. If the Ir surface can be cleaned and observed to reconstruct, then clearly most surfaces can be examined using the UHV-H9000. It was also found that surfaces can no longer be treated as entities unto themselves, but must be considered as part of a materials system which consists of both the bulk and surface of the crystal.

§ 7.2 COMPARISON OF AU AND IR SURFACES

It is difficult to generalize the results from surface reconstruction studies of the (001) surfaces of noble metals. The differences in findings between the Au and Ir (001) surfaces illustrate this quite convincingly. About the only generalization that can be made about these metal surfaces, is that the (001) surface reconstructions of Au, Pt and Ir consist of hexagonal overlayers superimposed on the bulk terminated (1x1) surface mesh. The surface unit cells of each surface possess different dimensions ranging from (5x1) for

Ir and (5x20) for Pt, to (5xn) for Au, where n is between 15 and 21. One specific danger of generalization that can be gleaned from our results on the Ir and Au surfaces is the attempt to quantify the surface reconstruction process in terms of the thermodynamic state variables of temperature and pressure. It is clear from even a cursory examination of the existing literature on both the Au and Ir surfaces, that there is no set transition temperature for reconstruction. This is particularly true of the Ir (5x1) reconstruction. The often cited transition temperature of 800 °K is certainly a misleading quantity. In the background of Chapter 5 it was pointed out that Grant found the surface to reconstruct by heating to only 400 °K. A more correct assessment is that the transition between the (1x1) and reconstructed surfaces is a function of temperature, pressure and more importantly, the defect state of the crystal. The defect state of the crystal is largely a function of how the specimens were prepared.

The Au surface was found to reconstruct with a hard, unvarying '5' dimension, while the n dimension is softer and more variable. The Au surface was found to be more susceptible to the influence of strain fields from subsurface bulk defects. The Ir (5x1) reconstruction was not found to vary in dimension like the Au. The Ir (5x1) occurs in straight bands which are unaffected by the presence of subsurface dislocations and IrO₂ precipitates. This can qualitatively be explained by the fact that Ir has one of the highest surface energies of any metal (roughly 2x that of Au) and would therefore be less susceptible to any interaction with the strain fields of subsurface bulk defects. An interesting offshoot of this observation is that the bending of Moire fringes for the Au (5xn) reconstruction near bulk defects is a real phenomena and not just a diffraction

effect. It is not necessary to take multiple images of defects and the reconstruction to draw conclusions about such interactions.

Interactions of defects with reconstructed surfaces is one aspect of surface reconstruction that should be considered by all investigators. One effect that is specific to TEM is the interaction between the two surfaces of thin TEM foils. In the limit of thin foils, it is possible that the two surfaces can influence each other through image forces. If the thickness of the crystal is less than the effective image force distance, the surfaces can affect each other. It would then be possible in this case for reconstruction on one surface to interact with reconstruction on the other. Defects in the crystal between the surfaces will also have a similar effect. For the crystals used in the Au and Ir runs this is not an issue, but this effect should never the less be kept in mind when interpreting the results of UHV-TEM experiments from thin foils.

§ 7.3 DISLOCATION ANALYSIS

At first glance, the dislocation analysis presented in Chapter 6 may seem unconnected with the experimental results presented in Chapters 3 5. Originally, the intent of this dislocation analysis was to explore the possibility that the misfit between the reconstructed hexagonal layer on the Au (001) surface and the bulk terminated (1x1) surface might be taken up by arrays of straight edge dislocations. We wanted to see if this was an energetically feasible. In particular, was it possible that a metastable position below the surface might be found which would correspond to the coincidence period of the reconstruction? The analysis of the dislocation energetics for both the single and

array of edge dislocations shows that no such metastable state exists as a function of distance below the surface. Also, we didn't find evidence for an array of dislocations with a spacing equal to the coincidence length of the reconstruction. It is however possible that the image of a dislocation near the surface would have different contrast than a bulk dislocation due to the image effects unique to dislocations near surfaces. The examination of activation energy and critical thickness imply that for misfits of greater than 1 %, the introduction of edge dislocations into the misfitting system will be spontaneous. For reconstructed surfaces like Au, there should be some dislocations near the surface to accommodate the roughly 4% compression of the reconstructed overlayer. The predictions of this model merit further investigation experimentally but are not out of line with what is seen for the Au and Ir (001) surfaces.

§ 7.4 SUGGESTIONS FOR FUTURE RESEARCH

Future work based on the results presented in chapters 2 through 5 can be broken down into two categories. The first is the refinement of existing data and the second is the extension of this work to other surfaces. As was mentioned at the end of chapter 5, the geometry of the reconstructed overlayer of the Ir (001) (5x1) reconstruction had been determined but that atom positions of the reconstructed layer relative to the bulk have not yet been determined. Work is underway to do just this by using high resolution TEM images of the reconstruction in conjunction with multislice simulations. Dr. Peirong Xu has measured the intensities of several of the reconstructed (5x1) surface spots directly using the Gatan PEELS spectrometer. With these data, a Patterson function might be

constructed which would also allow the determination of the atom positions for the reconstructed surface directly.

The Au (001) reconstructed surface described in chapter 3 could also be revisited. This work was our first on a Au (001) single crystal surface. It would be interesting to have a look at the intensities of the reconstruction spots in the diffraction pattern with the idea in mind of determining the atom positions, similar to what is underway with the Ir (001) (5x1) diffraction intensities.

Another facet of this work that would be interesting to pursue is the analysis of the images showing digital step contrast in chapter 5. The image of steps shown in chapter 5 is one of the simpler images we obtained. More complex images have been obtained and it is not clear how to interpret the range of contrast levels. Furthermore, recent dark field images taken with the {1x1} show contrast variations from both the reconstructed surface and steps.

Lastly, there are many surfaces that can be studied using the methods described in chapters 2 through 5. One surface that would be interesting to have a look at is the Au (111) surface. This surface is known to have large surface stress components that are known to affect the reconstruction. The reconstruction of this surface has been reported to reconstruct into a large surface unit cell whose dimensions have not been conclusively determined.

Another interesting surface to study is the Ge (111) surface, since the reconstruction on this surface is sensitive to the defect state of the bulk crystal. The

$c(2 \times 8)$ surface is the most widely reported surface but there have been (7×7) and smaller unit cells reported in crystals with high defect concentrations. This would provide an excellent opportunity to study the interaction of bulk defects with the reconstructed surface.

REFERENCES

CHAPTER 1

1. R.E. Schier and H.F. Farnsworth, "Structure And Adsorption Characteristics of Clean Surfaces of Germanium and Silicon", Journal of Chemical Physics, 30 (1959): 917.
2. P. Mark, J.D. Levine and S.H. McFarlane, "Atomic Structure of The Si (111) 7x7 Surface" Physical Review Letters, 38 (1977): 1408.
3. M.A. Van Hove, W.H. Weinberg and C.M. Chan, Low Energy Electron Diffraction, Experiment, Theory and Surface Structure, (New York: Springer-Verlag, 1986) 146.
4. A. Zangwill, Physics At Surfaces, (New York: Cambridge University Press, 1988) 41.
5. S. Brennan, "Two Dimensional X-Ray Scattering", Surface Science 152/153 (1985): 1.
6. J.M. Cowley, "Electron Microscopy of Surface Structures", Progress In Surface Science, 2 (1986): 209.
7. W. Telieps, M. Mundschau and E. Bauer, "Surface Domain Structure of Reconstructed Au {100} Observed By Dark Field Low Energy Microscopy", Surface Science 225 (1990): 87.
8. G. Binnig and H. Rohrer, "Scanning Tunneling Microscopy", IBM Journal of Research and Development 30 (1986): 355.
9. G. Binnig, H. Rohrer, C. Gerber and E. Stoll, "Real Space Observation of The Reconstruction Of Au (100)", Surface Science, 144 (1984): 321.
10. J.E. Bonevich and L.D. Marks, "Ultrahigh Vacuum Electron Microscopy of Crystalline Surfaces", in: Microscopy: The Key Research Tool, (Woodshole: The Electron Microscopy Society of America, 1992) 22 95-102.
11. L.D. Marks, R. Ai, J.E. Bonevich, M.I. Buckett, D. Dunn, J.P. Zhang, M. Jacoby and P. Stair, "UHV Microscopy of Surfaces", Ultramicroscopy 27 (1991): 90.
12. K. Takayanagi, K. Yagi, K. Kobayashi, and G. Honjo, "Techniques For Routine UHV In Situ Electron Microscopy of Growth Processes of Epitaxial Thin Films", Journal of Physics E 11 (1978) 441.

13. K.Yagi, "In Situ UHV Electron Microscopy of Surfaces", in: Crystals, Growth, Properties and Applications, (Berlin: Springer-Verlag, 1982)
14. E. Morita, K. Takayanagi, K. Kobayashi, K. Yagi and G. Honjo, "An Ion-Sputtering Gun To Clean Crystals In-Situ In An Ultrahigh Vacuum Electron Microscope", Japanese Journal of Applied Physics 19 (1980): 1891.
15. K. Mori, K. Kobayashi, K. Takayanagi, K. Yagi and G. Honjo, "Electron Beam Evaporator For In Situ Deposition Studies of Refractory Metal Thin Films", Japanese Journal of Applied Physics, 19 (1980): 183.
16. M.L. McDonald and J.M. Gibson, "An Ultrahigh Vacuum and Ultrahigh Resolution Electron Microscope", in: Proceedings of The 42 nd Annual Meeting of The Electron Microscope Society of America, ed. G.W. Bailey (San Francisco: San Francisco Press, 1984) 436.
17. K. Heinemann and H. Poppa, "An UHV Multipurpose Specimen Chamber With Sample Introduction System For In-Situ Transmission Electron Microscopy", Journal of Vacuum Science and Technology, A4 (1986): 127.
18. Y. Kondo, K. Ohi, Y. Ishibashi, H. Hirano, H. Kobayashi, Y. Hirada, K. Takayanagi and K. Yagi, "Development of An Ultrahigh Vacuum Transmission Electron Microscope", Journal of Electron Microscopy 36 (1987) 337.
19. D.J. Smith, J.J. Podbrodsky, P.R. Swan and J.S. Jones, "Initial Experiences With a 300 kV HREM Converted For UHV Operation" , in: Materials Research Society Meeting Symposium Proceedings, 139 (1989) 282.
20. J.J. Metois, S. Nitsche and J.C. Heyraud, "An Ultra-High-Vacuum Transmission And Scanning Electron Microscope For Crystal Growth Experiments", Ultramicroscopy 27 (1989): 349.
21. Y. Kondo, K. Yagi, K. Kobayashi, H. Kobayashi, U. Yanaka, K. Kise and T. Ohkawa, "Design Features of An Ultrahigh Vacuum Electron Microscope", Ultramicroscopy 35 (1991) 111.
22. Y. Kondo, K. Yagi, K. Kobayashi, H. Kobayashi, U. Yanaka, K. Kise and T. Ohkawa, "Design Features of An Ultrahigh Vacuum Electron Microscope For REM and PEEM Studies of Surfaces", Ultramicroscopy 36 (1991) 142.

23. K. Takayanagi, Y. Tanishiro, K. Yagi, K. Kobayashi and G. Honjo, "UHV-TEM Study of Au (111): Metastable $p \times p$ And Stable $p \times 1$ Surface Structure", Surface Science, 205 (1988) 637-657.
24. G. Nihoul, K. Abdelmoula and J.J. Metois, "High Resolution Images of A Reconstructed Surface Structure on (111) Gold Platelets: Interpretation And Comparison With Theoretical Models", Ultramicroscopy, 12 (1984) 353-360.
25. K. Yamazaki, K. Takayanagi, Y. Tanishiro, and K.Yagi, "TEM Study of The Reconstructed Au (001) Surface", Surface Science 199 (1988) 595-608.
26. K. Yagi, K. Takayanagi, K. Kobayashi, N. Osakabe, Y. Tanishiro and G. Honjo, "Surface Study By An UHV Electron Microscopy", Surface Science 86 (1979) 174-181.
27. J.M. Gibson, M.L. McDonald and F.C. Unterwald, "Direct Imaging of a Novel Silicon Surface Reconstruction", Physical Review Letters 55 (1985): 1765.
28. R.J. Wilson and P.M. Petroff, "Cryopump and Sample Holder For Clean Reconstructed Surface Observations In A Transmission Electron Microscope", Review of Scientific Instruments 54 (1983): 1534.
29. P.M. Petroff and R.J. Wilson, " Surface Dislocation Process For Surface Reconstruction and Its Application to the Silicon (111) (7x7) Reconstructions", Physical Review Letters 51 (1983): 199.
30. K. Takayangi, T. Tanishiro, S. Takahashi and M. Takahashi, "Structure Analysis of Si (111) 7x7 Reconstructed Surface By Transmission Electron Diffraction", Surface Science 164 (1985) 367-392.

CHAPTER 2

1. Y. Tanishiro, H. Kanamori, K. Takayanagi, K. Yagi and G. Honjo, " UHV Transmission Electron Microscopy On The Reconstructed Surface of (111) Gold", Surface Science, 111 (1981): 395.
2. K. Yamazaki, K. Takayanagi, Y. Tanishiro and K. Yagi," Transmission Electron Microscope Study of The Reconstructed Au (001) Surface", Surface Science, 199 (1988): 595.
3. John Edward Bonevich, "Atomic Structure And Sintering Behavior of Ultrafine Ceramic Particles" (Ph.D. diss., Northwestern University, 1991), 59-72.

4. Mary Irene Buckett, "Electron Radiation Damage In Transition Metal Oxides" (Ph.D. diss., Northwestern University, 1991), 108-109.
5. J.W. Edington Practical Electron Microscopy In Materials Science, Vol. 5, (Eindhoven: Philips, 1974), 62.
6. Timothy Scottron Savage, "UHV-TEM Studies of Silicon (111) Single Crystals After Thermal And Laser Treatments" (Masters Thesis, Northwestern University, 1991), 21-27.
7. R. Ai, D.N. Dunn, T.S. Savage, J.P. Zhang and L.D. Marks, " In Situ TEM Sample Preparation For Surface-Sensitive Plane View Imaging," in Proceedings of The 49th Annual Meeting of The Electron Microscopy Society of America, ed G.W. Bailey, (San Francisco: San Francisco Press, Inc., 1991) 642.
8. R. Ai, T.S. Savage, P. Xu, J.P. Zhang and L.D. Marks, "Microstructure of Si (111) On On Ion Sputtering And Electron Annealing" , in Vol 236: Photons and Low Energy Particles in Surface Processing, (Pittsburgh: Materials Research Society, 1991) 259.
9. D. Cherns, "Direct Resolution Of Surface Atomic Steps By Transmission Electron Microscopy", Philosophical Magazine 14 (1974): 549.
10. K. Kambe and G. Lehmpfuhl, "Weak-Beam Technique For Electron Microscopic Observation of Atomic Steps on Thin Single-Crystal Surfaces", Optik 42 (1975) 187.
11. S. Iijima, "Observation of Single and Clusters of Atoms in Bright Field Electron Microscopy", Optik 48 (1977): 193.
12. J.P.F. Levitt and A. Howie, "The Imaging of Surface Step Structures By Dark Field Electron Microscopy", Journal of Microscopy 116 (1979): 89.
13. S. Iijima, "Observation of Atomic Steps of (111) Surface of a Silicon Crystal Using Bright Field Electron Microscopy", Ultramicroscopy 6 (1981): 41.
14. J.C. Heyraud and J.J. Metois. "Anomalous $1/3$ 422 Diffraction Spots From {111} Flat Gold Crystallites: (111) Surface Reconstruction And Moire Fringes Between The Surface And The Bulk", Surface Science 100 (1980): 519.
15. G. Lehmpfuhl and K. Takayanagi, "Electron Microscopic Contrast of Atomic Steps on FCC Metal Crystal Surfaces", Ultramicroscopy 6 (1981): 195.

16. K. Yagi, K. Takayanagi and G. Honjo, "In-Situ UHV Electron Microscopy of Surfaces", in: Crystals, Growth, Properties and Applications 7, (Berlin: Springer-Verlag, 1982): 48.
17. K. Takayanagi, "High Resolution Surface Study By In-Situ UHV Transmission Electron Microscopy", Ultramicroscopy 8 (1982): 145.
18. K. Takayanagi and K. Yagi, "Monatom-High Level Electron Microscopy", Transactions of The Japan Institute of Metals 24 (1983): 337.
19. J.M. Gibson, "Transmission Electron Microscopy And Diffraction From Semiconductor Interfaces And Surfaces", in: Surface And Interface Characterization By Electron Optical Methods, ed. A. Howie and U. Valdre (New York: Plenum Publishing Co., 1988) 55.
20. N. Ikarashi, K. Kobayashi, H. Koike, H. Hasegawa and K. Yagi, "Profile and Plan-View Imaging of Reconstructed Surface Structures of Gold" Ultramicroscopy 26 (1988): 195.
21. Y. Nakai, "Phase Information In Transmission Electron Diffraction By Solid Surfaces", Surface Science 202 (1988): 99.
22. K. Takayanagi, "Surface Structure Analysis by Transmission Electron Diffraction: Effects of The Phases of Structure Factors", Acta Crystallographica A46 (1990): 83.
23. L.D. Marks, T.S. Savage, J.P. Zhang and R. Ai, "Validity of The Kinematical Approximation in Transmission Electron Diffraction For Surfaces, Revisited", Ultramicroscopy 38 (1991): 343.
24. J.M. Gibson and M.Y. Lanzerotti, "Silicon Oxidation Studies By In-Situ TEM", Ultramicroscopy 31 (1989) 29.
25. L.M. Peng and M.J. Whelan, "On The Uncoupling of Surface Superlattice Reflections in TED Analysis of Reconstructed Surfaces", Acta Crystallographica A47 (1991) 107.

CHAPTER 3

1. D.G. Fedak and N.A. Gjostein, "A Low Energy Electron Diffraction Study of The (100), (110) and (111) Surfaces of Gold" Acta Metallurgica 15 (1967): 827.
2. D.G. Fedak and N.A. Gjostein, "Structure And Stability of The (100) Surface of Gold", Physical Review Letters 16 (1966): 171.
3. D.G. Fedak, N.A. Gjostein, " On The Anomalous Surface Structures of Gold", Surface Science 8 (1967): 77.
4. P.N.J. Dennis, P.J. Dobson, "Investigation On The {100} Gold Surface", Surface Science 33 (1972): 187 .
5. G.E. Rhead,"On The Anomalous Surface Structures of Gold and Platinum", Journal of Physics : F 3 (1973): L53.
6. M.A. Van Hove, R.J. Koestner,P.C. Stair, J.P. Biberian, L.L. Kesmodel, I. Bartos, G.A. Somorjai, "The Surface Reconstructions of The (100) Crystal Faces of Iridium, Platinum and Gold", Surface Science 103 (1981): 189.
7. F. Gronlund, P.E. Hojlund Nielsen, "The 5x20 Surface Structure of Gold", Journal of Applied Physics 43 (1972): 391.
8. K.H. Reider, T. Engel, R.H. Swendsen, "Helium Diffraction Study of The Reconstructed Au (100) Surface", Surface Science 127 (1983) 223.
9. G.K. Binnig and H. Rohrer, "Real Space Observation of The Reconstruction of Au (001)",Surface Science 144 (1984): 321.
10. K. Yamazaki, K. Takayanagi, Y. Tanishiro and K. Yagi, "Transmission Electron Microscopy Study of The Reconstructed Au (001) Surface", Surface Science 199 (1988): 595 .
11. D.M. Zehner, B.R. Appelton, "Characterization of Reordered (001) Au Surfaces By Positive-Ion-Channeling Spectroscopy, LEED and AES", Journal of Vacuum Science Technology, 12 (1975): 454.

CHAPTER 4

1. P.M. Petroff and R.J. Wilson, "Surface Dislocation Process for Surface Reconstruction and Its Application To The Silicon (111) (7x7) Reconstructions", *Phys. Rev. Let.* **51**, 199 (1983).
2. J. Dundurs, Private Communication.
3. T.S. Savage, R. Ai, and L.D. Marks Private Communication.

CHAPTER 5

1. G. Kisters, J.G. Chen, S. Lehwald and H. Ibach, "Adsorption of CO on The Unreconstructed and Reconstructed Ir (001) Surface", *Surface Science* **245** (1991): 65.
2. E. Lang, K. Muller and K. Heinz, "Intensity Analysis of The (1x5) Reconstruction of Ir (100)", *Surface Science* **127** (1983): 347.
3. K. Heinz, G. Schmidt, L. Hammer and K. Muller, "Dynamics of The Reconstruction Process Ir (100) 1x1 -> 5x1", *Physical Review B* **32** (1985): 6214.
4. M. A. Van Hove, W. H. Weinberg and C. M. Chan, Low Energy Electron Diffraction, Experiment, Theory and Surface Structure Determination, (New York: Springer Verlag 1986)
5. T. N. Rhodin and G. Broden, "Preparation and Chemisorptive Properties of The Clean Normal and Reconstructed Surfaces of Ir (100) - Role of Multiplets", *Surface Science* **60** (1976): 466.
6. N. T. Barrett, C. Guillot, B. Vilette, G. Treglia and B. Legrand, "Investigation of The Core Level Shift between Surface and Subsurface Atoms of the Iridium (100)(1x1) and (100)(5x1) Surfaces", *Surface Science* **251/252** (1991): 717.
7. S. Lehwald, J. G. Chen, G. Kisters, E. Preuss and H. Ibach, "Surface-Phonon Dispersion Investigation of The (1x1)->(5x1) Reconstruction of the Ir (100) Surface", *Physical Review B* **43** (1991): 3920.
8. J. T. Grant, "A LEED Study of The Ir (100) Surface", *Surface Science*, **18** (1969): 228.

9. K. Heinz, H. Hertrich, L. Hammer and K. Muller, "Low Temperature ordering of Potassium on Ir (100) 1x1 and Ir (100) 5x1", Surface Science, 152/153 (1985): 303.
10. N. Bickel and K. Heinz, "Quasidynamical LEED Structure Determination of The Ir (100) 1x5 Surface Reconstruction", Surface Science, 163 (1985): 435.
11. M. A. Van Hove, R. J. Koestner, P. C. Stair, J. P. Biberian, L. L. Kesmodel, I. Bartos and G. A. Somorjai, "The Surface Reconstructions of The (100) Crystal Faces of Iridium, Platinum, and Gold", Surface Science, 103 (1981): 218.
12. Q. J. Gao and T. T. Tsong, "Direct Observation of Atomic Steps and Atomic Structures in The Reconstruction of Pt and Ir Surfaces", Journal of Vacuum Science and Technology A5, 4 (1987): 761.
13. J. Witt and K. Muller, "Evidence for The Ir (100) Surface Reconstruction by Field Ion Microscopy", Physical Review Letters, 57 (1986): 1153.
14. K. Muller, J. Witt and O. Schutz, "Iridium Surface Reconstruction: A Field Ion Microscopy Study", Journal of Vacuum Science and Technology A5, 4 (1987): 757.
15. D. N. Dunn, J. P. Zhang and L. D. Marks, "UHV Microscopy of The Reconstructed Au (001) Surface", Surface Science, 260 (1990): 220.
16. A. R. Sandy, S. G. J. Mochrie, D. M. Zehner, G. Grubel, K. G. Huang and D. Gibbs, "Reconstruction of the Pt (111) Surface", Physical Review Letters, 68 (1992): 2192.
17. H. M. Ondik and G. M. Wolten, Crystal Data, Determinative Tables Volume II: Inorganic Compounds, (Nation Bureau of Standards and Joint Committee on Powder Diffraction Standards, 1973): T-45.
18. H. M. Ondik and G. M. Wolten, Crystal Data, Determinative Tables Volume II: Inorganic Compounds, (Nation Bureau of Standards and Joint Committee on Powder Diffraction Standards, 1973): C-115.

CHAPTER 6

1. F.C. Frank and J.H. Van der Merwe, " One Dimensional Dislocations I. Static Theory", Proceedings of The Royal Society, A198 (1949): 205.
2. F.C. Frank and J.H. Van der Merwe, " One Dimensional Dislocations III. Influence of The Second Harmonic Term In The Potential Representation on, The Properties of The Model", Proceedings of The Royal Society, A198 (1949): 205.
3. W.A. Jesser and D. Kuhlmann-Wilsdorf, "On The Theory of Interfacial Energy And Elastic Strains of Epitaxial Overgrowths In Parallel Alignment On Single Crystals", Phys. Stat. Sol. 19 (1967): 95.
4. J.H. Van der Merwe, "Equilibrium Structure of a Thin Epitaxial Film", Journal of Applied Physics, 41 (1970): 4725.
5. J.H. Van der Merwe, "Crystal Interfaces Part I: Semi-Infinite Crystals", Journal of Applied Physics, 34 (1963): 117.
6. J.H. Van der Merwe, "Crystal Interfaces Part II: Finite Overgrowths", Journal of Applied Physics, 34 (1963): 123.
7. J.A. Synmann and J.H. Van der Merwe, "Computed Epitaxial Monolayer Structures: I. One-Dimensional Model: Comparison of Computed And Analytical Results", Surface Science 42 (1974): 190.
8. J.A. Synmann and Synmann, " Computed Epitaxial Monolayer Structures: I. Two-Dimensional Model: Zero Average Strain Monolayer Structures In The Case of Hexagonal Interfacial Symmetry", Surface Science 105 (1981): 357.
9. A.K. Head, "Edge Dislocations In Inhomogeneous Media", Proceedings of The Royal Society, 66B (1953): 793.
10. E. Yoffe, "A Dislocation At A Free Surface", Philosophical Magazine 6 (1961): 1147.
11. J. Lothe, V.L. Indenbom and V.A. Chamrov, "Elastic Field And Self Force of Dislocations Emerging At The Free Surfaces of Anisotropic Halfspaces", Phys. Stat. Sol. 111 (1982): 671.
12. F.R.N. Nabarro and E.J. Kostlan, "The Stress Field of A Dislocation Lying In A Plate", Journal of Applied Physics, 49 (1978): 5445.

13. William C. Moss and William G. Hoover, "Edge Dislocation Displacements In An Elastic Strip", 49 (1978): 5449.
14. J. Dundurs and T. Mura, "Edge Dislocation Near A Circular Inclusion", Journal of Mechanics and Physics of Solids, 12 (1964): 177.
15. J. Dundurs and G.P. Sendeckyj, "Behavior of An Edge Dislocation Near A Bimetallic Interface", Journal of Applied Physics 36 (1965): 3353.
16. J. Dundurs, Private Communication.
17. P. Morse and H. Feshbach, Methods of Theoretical Physics, (New York: McGraw Hill Co., 1953) 413.

CHAPTER 7

1. Mary Irene Buckett, "Electron Radiation Damage In Transition Metal Oxides" (Ph.D. diss., Northwestern University, 1991), 108-109.
2. O.L. Krivanek and M.K. Kundmann, "Improved Detection Limits With Parallel Detection EELS", , in: Proceedings of The 49 nd Annual Meeting of The Electron Microscope Society of America, ed. G.W. Bailey (San Francisco: San Francisco Press, 1984) 724-725.

